OUKA
The University of Osaka
Institutional Knowledge Archive

| | |
|---|---|
| Title | Solidification Cracking Prevention by Thermal Strain Control |
| Author(s) | 李, 齋炯 |
| Citation | 大阪大学, 2021, 博士論文 |
| Version Type | VoR |
| URL | https://doi.org/10.18910/82229 |
| rights | |
| Note | |

*The University of Osaka Institutional Knowledge Archive : OUKA*

https://ir.library.osaka-u.ac.jp/

The University of Osaka

Doctoral Dissertation

# Solidification Cracking Prevention by Thermal Strain Control

Jae-Hyeong Lee

December 2020

Division of Materials and Manufacturing Science

Graduate School of Engineering,

Osaka University

# Contents


**1. Introduction** 1

1.1 Purpose and flow chart of study 1

**2. Background of study** 4

2.1 Application and characteristic of stainless steel 4

2.2 Solidification-phase relationship in the Fe-Cr-Ni system 5

2.3 Solidification mode of stainless steel welds 6

2.4 Solidification cracking occurrence in stainless steel 7

2.4.1 Solidification cracking occurrence and propagation 7

2.4.2 Effect of solidification mode on solidification cracking 8

2.4.3 Effect of impurity and alloy elements on solidification cracking 9

2.5 Limits of metallurgical prevention method for solidification cracking 10

2.6 Thermomechanical reason for solidification cracking 11

2.7 Evaluation of solidification cracking susceptibility in austenitic stainless steel 13

2.7.1 The Transverse Varestraint test 13

2.7.2 In-situ observation method in U-type hot cracking test 15

2.7.3 Difference between Transverse Varestraint test and U-type hot cracking test 16

**3. Proposal and establishment of solidification cracking prediction method** 18

3.1 Introduction 18

3.2 Materials and experimental procedures 18

3.2.1 Material 18

3.2.2 U-type hot cracking test 19

3.2.3 Solidification cracking observation 20

3.3 Solidification cracking in U-type hot cracking test 20

3.4 Basic concept of solidification cracking prediction model 22

3.5 Thermal strain calculation using finite element method 22

3.5.1 Finite element model 22

3.5.2 Comparison of temperature properties and thermal strain between experiment and simulation 23

3.6 Critical strain measurement by in-situ observation technique 25

3.7 Theoretical approach to solidification cracking susceptibility of GTAW 26

3.7.1 Calculation of solidification initiation temperature 27

3.7.2 Calculation of solidification completion temperature 30
3.8 Evaluation of solidification cracking susceptibility in GTAW 31
3.9 Prediction results of solidification cracking 32
3.10 Proposal of thermal strain control for solidification cracking prevention 33
3.11 Summary 34

**4. Effects of laser in-situ post heating on solidification cracking behavior** 35
4.1 Introduction 35
4.2 Materials and experimental procedures 35
4.2.1 Material 35
4.2.2 U-type hot cracking test with in-situ laser post heating 36
4.2.3 Solidification cracking observation 37
4.3 Solidification cracking according to laser beam condition 37
4.4 Thermal strain calculation using finite element method 41
4.4.1 Finite element model 41
4.4.2 Comparison of weld bead shape and temperature history between experiment and simulation 41
4.5 Critical strain measurement in laser in-situ post heating 42
4.6 Theoretical approach to solidification cracking susceptibility in GTAW-laser welding 44
4.7 Evaluation of solidification cracking susceptibility in GTAW-laser welding 46
4.8 Influence of laser in-situ post heating on solidification cracking behavior 47
4.8.1 Effect of laser power on solidification cracking behavior 47
4.8.2 Effect of heat source distance on solidification cracking behavior 48
4.8.3 Effect of laser beam size on solidification cracking behavior 49
4.9 Controlling of thermal strain behavior in laser in-situ post heating 50
4.9.1 Controlled by laser power 51
4.9.2 Controlled by heat source distance 53
4.9.3 Controlled by laser beam size 55
4.10 Summary 58

**5. Prevention of solidification cracking by temperature history control via cooling process** 59
5.1 Introduction 59
5.2 Materials and experimental procedures 59
5.2.1 Material 59

5.2.2 U-type hot cracking test with water-cooled GTAW 59
5.2.3 Solidification cracking observation 61
5.3 Solidification cracking suppression via water-cooled GTAW 61
5.4 Thermal strain calculation using finite element method 61
5.4.1 Finite element model 61
5.4.2 Comparison of weld bead shape and temperature history between experiment and simulation 62
5.5 Theoretical approach to solidification cracking susceptibility 63
5.6 Evaluation of solidification cracking susceptibility in coolant-cooled GTAW 64
5.7 Influence of cooling process on solidification cracking behavior 66
5.8 Governing factors and controlling of thermal strain behavior in coolant-cooled GTAW 67
5.8.1 Temperature distribution 67
5.8.2 Controlled by cooling process 68
5.9 Summary 70

**6. Effect of temperature distribution of HAZ on solidification cracking** 72
6.1 Introduction 72
6.2 Materials and experimental procedures 72
6.2.1 Material 72
6.2.2 U-type hot cracking test according to welding speed change 72
6.2.3 Solidification cracking observation 73
6.3 Solidification cracking behavior according to welding speed 73
6.4 Thermal strain calculation using finite element method 75
6.4.1 Finite element model 75
6.4.2 Comparison of weld bead shape and temperature history between experiment and simulation 75
6.5 Theoretical approach to solidification cracking susceptibility 76
6.6 Evaluation of solidification cracking susceptibility 77
6.7 Influence of welding speed on solidification cracking behavior 78
6.8 Changing mechanism of thermal strain behavior according to welding speed 79
6.8.1 Effect of welding speed on temperature distribution of weld bead 79
6.8.2 Thermal strain behavior controlled by thermal expansion of heat-affected zone 82
6.9 Summary 84

**7. Prevention of solidification cracking by thermal expansion control via parallel laser heating** 86

7.1 Introduction 86

7.2 Materials and experimental procedures 86

7.2.1 Material 86

7.2.2 U-type hot cracking test with multi-beam welding 86

7.2.3 Solidification cracking observation 88

7.3 Solidification cracking behavior according to multi-beam welding 88

7.4 Thermal strain calculation using finite element method 90

7.4.1 Finite element model 90

7.4.2 Comparison of weld bead shape and temperature history between experiment and simulation 90

7.5 Theoretical approach to solidification cracking susceptibility 92

7.6 Evaluation of solidification cracking susceptibility in multi-beam welding 93

7.7 Influence of multi-beam welding on solidification cracking behavior 95

7.8 Controlling of thermal strain behavior in multi-beam welding 97

7.8.1 Controlled by overlapped heat sources in multi-beam welding 97

7.8.2 Controlled by non-overlapped heat sources in multi-beam welding 100

7.9 Optimization of multi-beam welding condition for solidification cracking prevention 103

7.10 Summary 104

**8. Conclusion** 106

**Acknowledgment** 110

**References** 111

**Paper and presentation** 119

# Chapter 1 Introduction

## 1.1 Purpose and flow chart of study

Austenitic stainless steels with high hot cracking susceptibility have a problem of solidification cracking during welding. The defect of the weld is a problem related to safety, therefore, various metallurgical prevention methods have been proposed, but has limited success. In this study, thermo-mechanical prevention methods have been studied without side effects. From a thermo-mechanical point of view, solidification cracking is represented by intersection of a hot ductility curve and thermal strain. In this study, we introduced several welding processes that suppress solidification cracking by controlling the thermal strain.

Fig. 1.1 shows the flow chart of the welding process design method to prevent solidification temperature cracking. Chapter 1 is introduction and Chapter 2 is background of this study.

In Chapter 3 solidification cracking prediction model is designed to quantitatively indicate the occurrence of solidification cracking. This model is represented by the hot ductility curve and thermal strain according to each welding condition. The hot ductility curve was obtained based on a combination of the solidification initiation and completion temperatures, in addition to the critical strain. The solidification initiation/completion temperatures were calculated using a metallurgical analysis model and critical strain was measured by in-situ observation method. The thermal strain according to the weld bead location was calculated using the finite element method. This model predicts occurrence and length of the solidification cracking. Therefore, quantitative evaluation of solidification cracking has become possible.

The effect of cooling rate on thermal strain behavior was investigated in Chapter 4 and 5.

In Chapter 4, the effect of cooling rate on solidification cracking behavior was investigated using the solidification cracking prediction model. The cooling rate of weld pool was controlled by laser in-situ post heating. The solidification cracking was vulnerable due to the temperature distribution increased by laser in-situ post heating. The solidification cracking susceptibility according to each welding condition was evaluated. And the effect of temperature distribution due to cooling rate on the thermal strain was investigated using the finite element method.

In Chapter 5, the water-cooling process was applied to prevent solidification cracking based on the understanding of the relationship between the amount of heat input and thermal strain. The experiment confirmed solidification cracking suppression. The hot ductility curve did not significantly change. However, the thermal strain behavior was decreased in water-cooled GTAW. In addition, the solidification cracking behavior according to water-cooling process on the weld bead was analyzed through the finite element method.

The effect of thermal expansion of HAZ on thermal strain behavior was investigated in Chapter 6 and 7.

In Chapter 6, the water-cooling process was applied to prevent solidification cracking, but the welding process became complicated. Therefore, the optimum welding process was investigated to suppress solidification cracking with a simple process. The behavior of cracking according to welding speed was compared. In addition, the effect of welding speed on hot ductility curve and thermal strain behavior was compared. The solidification cracking was suppressed by stress relief

due to thermal expansion of heat-affected zone. The specific principle of the effect of welding speed on solidification cracking behavior was investigated using the finite element method.

In Chapter 7, multi-beam laser welding process was employed by applying the principle of stress relief by thermal expansion to suppress solidification cracking. The laser beam was irradiated to the base material to suppress the solidification cracking due to the increase of expansion of the heat-affected zone. The effect of expansion change of the laser beam irradiated area on the behavior of thermal strain was analyzed using the finite element method.

Finally, Chapter 8 is the summarized conclusions of this study.

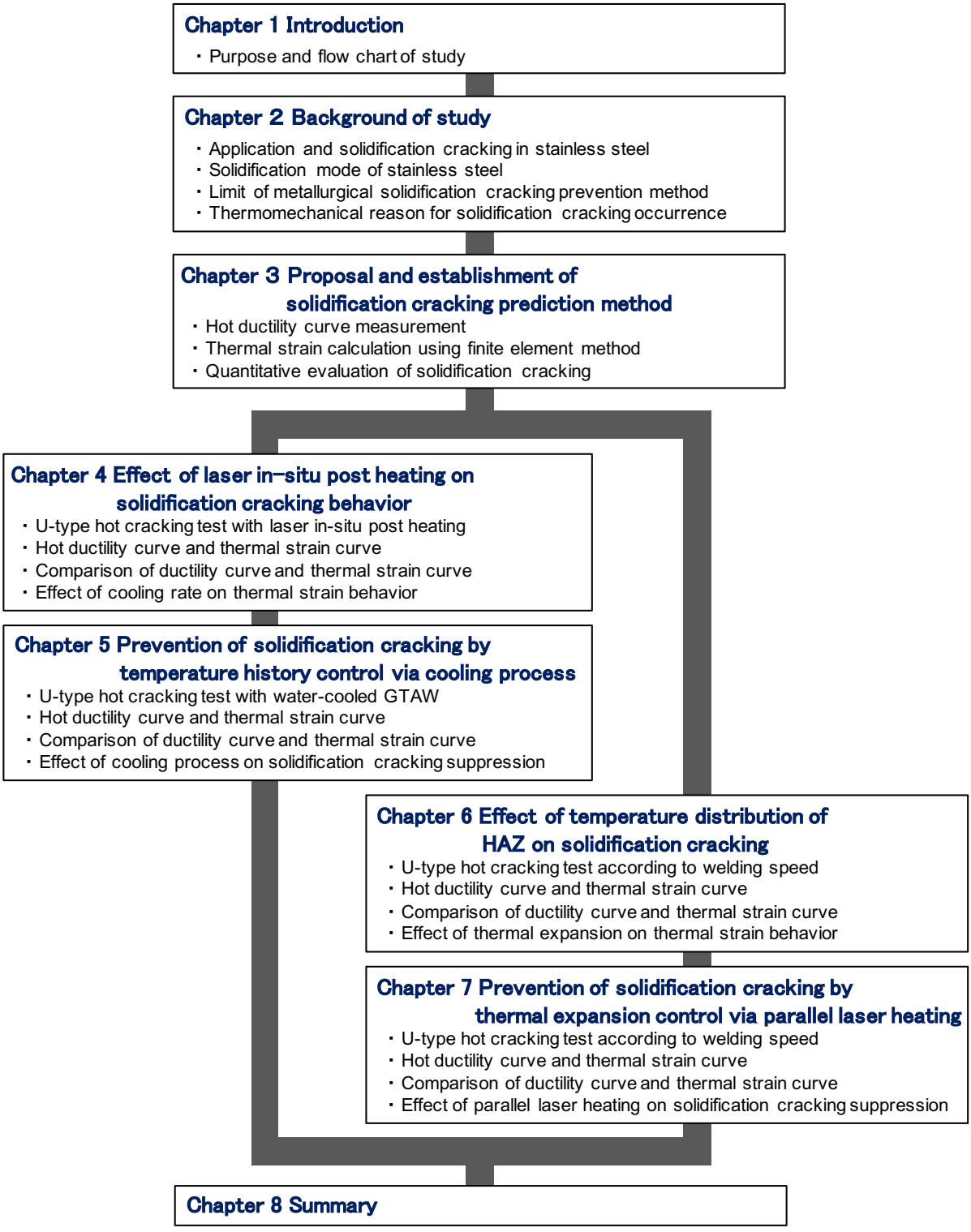



Fig. 1.1 Flow chart of study.

# Chapter 2 Backgrounds of study

## 2.1 Application and characteristic of stainless steel

Stainless steel has been used with phenomenal success in various industries for over 70 years. More applications are being discovered with every passing year as its advantages become more widely identified. From low-end applications, like cooking utensils and furniture, to very sophisticated ones, such as space vehicles and energy industry, the use of stainless steels is indispensable [1-8]. In fact, the omnipresence of stainless steels in our daily life makes it impossible to enumerate their applications.

The word 'steel' means that iron constitutes the bulk of the material, while the use of the adjective 'stainless' implies absence of staining, rusting or corroding in environments where 'normal' steels are susceptible. The term stainless steel is used to describe a family of about 200 alloys of steel with remarkable heat and corrosion resistance properties. Its distinguishing characteristic is the high amount of chromium. A stainless steel contains a minimum of 10.5 mass% chromium that improves its corrosion resistance and strength. The chromium in the alloy creates a passive layer on oxidation when exposed to air (Fig. 2.1). This layer acts as a shield against further corrosion essentially making the alloy rustproof. This mechanism allows for retaining a spotless appearance for long periods under normal working conditions. The carbon percentage can range from 0.03 mass% to 1.2 mass%.

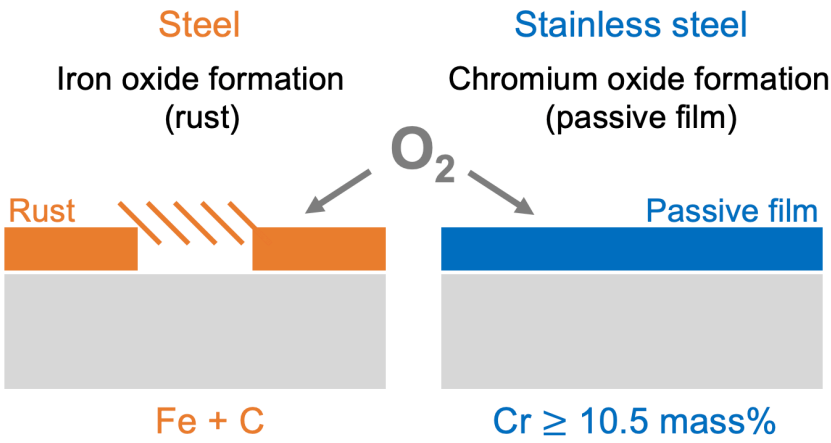
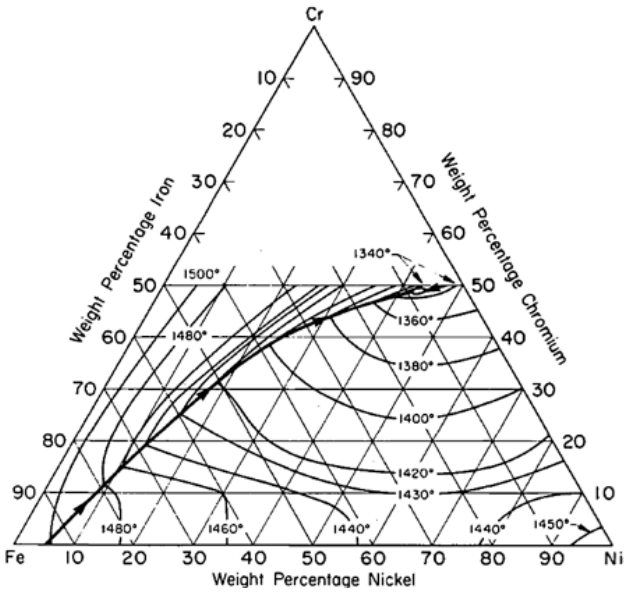



Fig. 2.1 Surface reaction in steel and stainless steel.

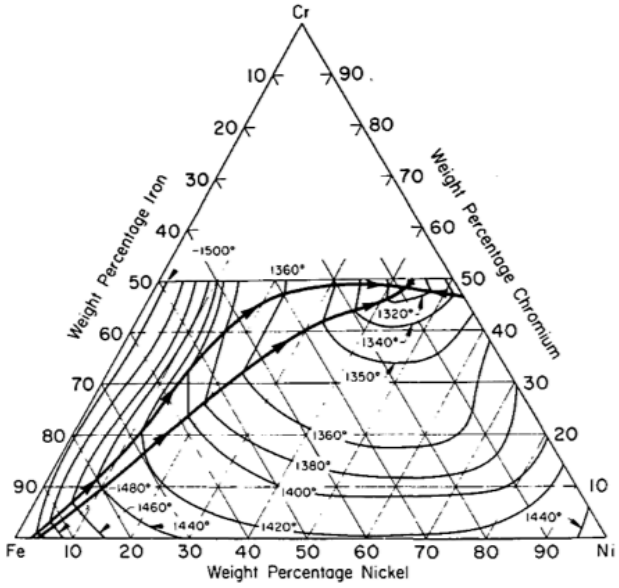
While the Fe–Cr system forms the basis, modern stainless steels, besides Cr, also contain a host of other alloying elements whose presence enhances specific properties. Ferritic stainless steels are classified in the 400 series, usually with 10 mass% to 30 mass% chromium content, and are often chosen for their excellent corrosion resistance and elevated temperature oxidation resistance. Austenitic stainless steels are classified in the 200 and 300 series, with 16 mass% to 30 mass% chromium and 2 mass% to 20 mass% nickel for enhanced surface quality, formability, increased corrosion and wear resistance. The presence of nickel improves corrosion resistance and makes stainless steel more ductile. The presence of molybdenum further enhances the resistance to corrosion in an acid medium. The most common grades is type 310S stainless steel.

## 2.2 Solidification phase relationship in the Fe-Cr-Ni system

Fig. 2.2 shows the ternary phase diagram of the Fe-Cr-Ni system [9-13]. The heavy curved line in Fig. 2.2 (a) shows the tough on the liquidus surface, which is called the line of twofold saturation. The initial solidifying phase is determined by the position of the alloy with respect to the liquidus surface, which under equilibrium conditions toward the eutectic/peritectic before solidification is complete. The line declines from the binary Fe-Ni reaction temperature to the ternary eutectic point at 49(mass%)Cr-43(mass%)Ni-8(mass%)Fe. The Cr-rich (upper) side of this heavy line have $\delta$-ferrite as the primary solidification phase, which means, the first solid phase to form from the liquid. On the other hand, the Ni-rich (lower) side have austenite as the primary solidification phase. The heavy curved lines on the solidus surface in Fig. 2.2 (b) more or less follow the trend of the liquidus trough and converge at the ternary eutectic temperature.




(a) Liquidus surface




(b) Solidus surface

Fig. 2.2 Phase diagram of Fe-Ni-Cr system [10].

### 2.3 Solidification mode of stainless steel welds

Most stainless steel compositions in wide use occur on the iron-rich side of the ternary diagram between 50 and 70 mass% iron. The 70 mass% iron isopleth of the ternary above 1473 K shown in Fig. 2.3 is commonly used to identify the primary solidifying phases for various compositions. This has also been called a pseudo-binary phase diagram. The solidification mode considered as (1) A mode: austenitic, (2) AF mode: austenitic-ferritic or primary austenitic, (3) FA mode: ferritic-austenitic or primary ferritic and (4) F mode: ferritic [14-20].

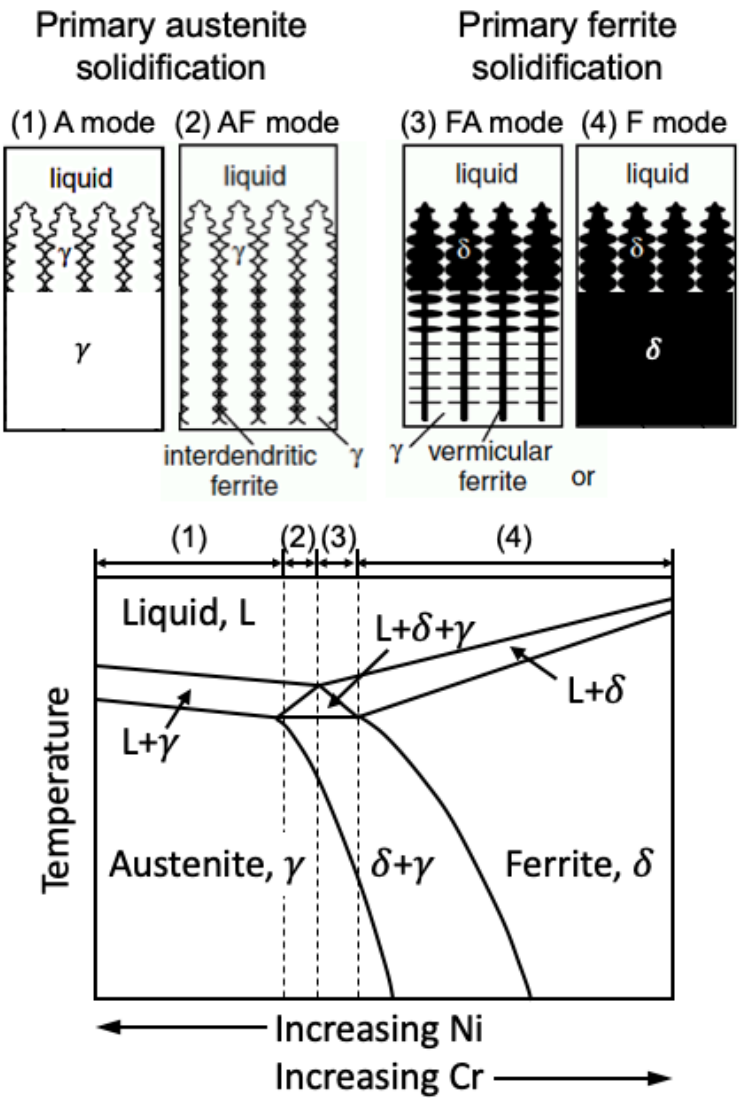



Fig. 2.3 Schematic diagram of solidification mode in Fe-Cr-Ni welds.

In fully austenitic stainless steels, the interdendritic regions are slightly enriched in both Ni and Cr, while in AF mode weld metal significant enrichment of Cr and depletion of Ni occur in the interdendritic regions. For an alloy on the Ni-rich (left) side of the apex of the three-phase eutectic triangle, austenite ($\gamma$) is the primary phase. Alloys solidifying in the A mode will remain unchanged to low temperatures. However, in the AF mode some eutectic ferrite phase would be formed. The light color dendrites shown in Fig. 2.3 (2) are austenite, while the dark particles between the primary dendrite arms are the $\delta$-ferrite that forms the three phases triangle is reached during the terminal

stage of solidification. These are called interdendritic ferrite. Interdendritic ferrite particles also forms between secondary dendrite arms.

A δ-ferrite nucleates in the Cr-rich and Ni-depleted regions as a non-equilibrium phase. When FA and F mode occurs, the dendrite core is significantly enriched in Cr and depleted in Ni. δ-ferrite is the primary solidification phase on the Cr-rich (right) side of the apex. In the Fig. 2.3 (3) and (4) shows δ-ferrite (dark dendrites). The center of the δ-ferrite dendrites, which forms at the beginning of solidification, is Cr rich area, while the outer portions, which form as temperature decreases, have lower chromium contents. During cooling into the $(\delta + \gamma)$ phase region, the outer portions of dendrites having less Cr transforms to austenite, thus leaving behind Cr-rich 'skeletons' of δ-ferrite at the dendrite cores. This skeleton ferrite is called vermicular ferrite. Also, primary δ-ferrite dendrites can transform to lathy or lacy ferrite upon cooling into the $(\delta + \gamma)$ phase region, as shown in Fig. 2.3 (4).

## 2.4 Solidification cracking occurrence in stainless steel

Stainless steel has a problem of solidification cracking during welding, and especially, austenitic stainless steel (Type 310S) has a high solidification cracking susceptibility [21-26]. Before preventing solidification cracking of stainless steel, it is necessary to find out the specific cause of cracking occurrence. It is necessary to understand the mechanism and effect of the solidification mode on solidification cracking susceptibility. The effect of solidification mode and composition on solidification cracking will be discussed in detail in subsequent sections.

### 2.4.1 Solidification cracking initiation and propagation

The mechanism of nucleation of solidification cracking has been studied and developed in various aspects over the past years. To date, solidification nucleation driving forces are well-established; solidification shrinkage, solid contraction in a thermal gradient and a high sensitivity to solute segregation. In 1976, Feurer [27] studied liquid presence between grains and argued that a solidification cracking will initiate as a pore if the liquid is no longer able to fill the inter-granular openings. However, this study only considered the contribution of solidification shrinkage. In 1988, Guven and Hunt [28] explained the role of tensile stresses in the solidification cracking formation. In 2003, Campbell [29] emphasized the importance of thermos-mechanical aspects and simply consider the alloy's solidification temperature range viz., the larger solid-liquid coexistence range, the more susceptible to solidification cracking. In 2015, Kou [30] focused on the grain boundary, such as liquid feeding between grains, separation of grains from each other and lateral growth of grains toward each other.

Numerous models have been proposed for solidification cracking in welds. In 1962, Prokhorov's model [31] focused mainly on the thermomechanical factor of cracking, assuming that cracking could occur if the rate of strain accumulation with temperature drop $d\varepsilon/dT$ exceeded a critical value. In1999, Rappaz [32] proposed a RDG model by extending Feurer approach [27] to included feeding associated with tensile deformation of the solidified material. In 2004, Eskin model [33] include the stress-based models, strain-based models and strain rate based models. This model clarified more recently the strain rate, instead of the strain itself, plays a critical role in the cracking.

Recently, studies on the behavior of solidification cracking have been reported. In 2017 Aucott [34] showed the growth of micro-cavities driven by increasing strain induced to the solidifying steel. These cavities grew through coalescence of micro-cavities to form micro cracks first and then through the propagation of micro cracks. Cracks propagated from the core of the weld towards the free surface along the solidifying grain boundaries. In 2018, on the basis of the previous research, Aucott [35] summarized the mechanism of solidification cracking in three steps (Fig. 2.4).

Stage 1: The cracking occur at solute-enriched liquid pockets where maximum volumetric strain is localized.

Stage 2: Cracks coalesce through inter-granular toward the heat source and propagates through the grain boundaries.

Stage 3: Inter-dendritic cracking occurs along the boundaries between solidifying columnar dendrites with higher liquid fraction.

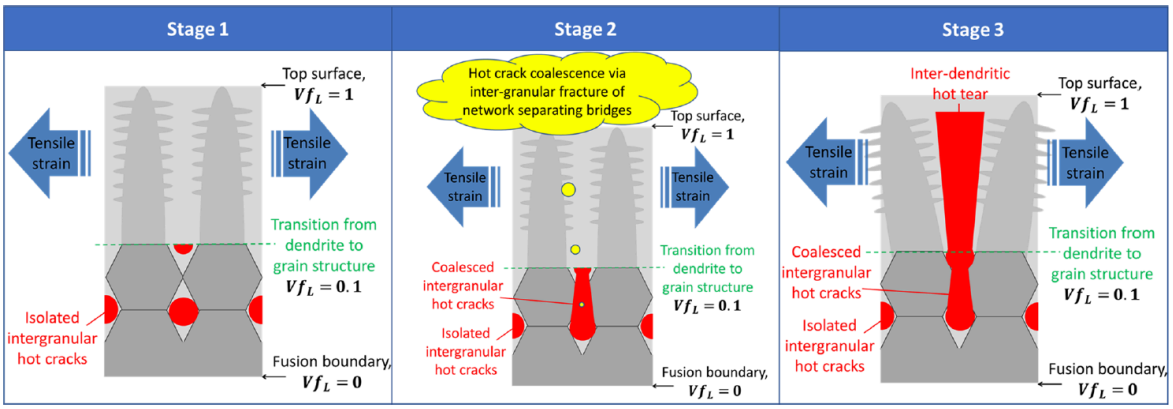



Fig. 2.4 Schematic illustration of solidification cracking propagation mechanism [33].

### 2.4.2 Effect of solidification mode on solidification cracking

Solidification products of austenitic-ferritic welds depend on the content of ferrite and austenite-forming elements. As an approximation, it can be said that a molten pool containing over 25 mass% Cr and about 10 mass% Ni will reproduce delta grains on solidification. $\delta$-ferrite has a great effect on the prevention of the solidification cracking. There are two main reasons for the improved cracking resistance when ferrite is formed during solidification of stainless steel welds.

First, ferrite has the BCC crystal structure as opposed to the FCC crystal structure of austenite. The BCC structure allows more rapid diffusion of impurity elements (and other elements that can form eutectic constituents) in stainless steels [36]. This reduces the segregation of impurity elements along weld metal grain boundaries and reduces the volume fraction of liquid films coating the grain boundaries at the end of solidification. The reduction in the volume fraction of liquid films limits the propagation of solidification cracking. In 1952, Pellini [37] also reported that the solidification temperature range of primary ferrite weld was less than that of primary austenite solidified welds, providing a smaller critical temperature range for crack formation due to the less impurity elements in the residual liquid film.

Secondly, austenite/ferrite interfaces are interlocking ("tortuous") as opposed to fairly straight grain boundary interfaces. This reduced the wetting of liquid films along the grain boundaries at the

end of solidification, and provided a tortuous path that was more resistant to fracture than the straight austenite/austenite boundaries. In 1979, Matsuda [38] reported that cracks were arrested by irregular path offered by a duplex austenite-ferrite structure. The peritectic/eutectic reaction interface arrested remaining pockets of liquid and suppress crack propagation. In addition to this, a number of factors have been proposed to explain the beneficial effects of $\delta$-ferrite on cracking behavior.

-The presence of ferrite refines the grain size of the solidified metal, which results in better mechanical properties and cracking resistance.
-Coarse grain formation in HAZ occurring by recrystallisation and grain growth in fully austenitic metals increase susceptibility to liquiation cracking [39].
-The presence of ferrite results in a larger interface which disperses the concentration of impurity elements at the grain boundaries.

The major factors that make FA/F mode weld metals resistant can be listed as, (a) the higher solubility of S, P (impurity elements), in the ferrite that introduces less of the harmful solute in the interdendritic regions, (b) lower wettability of grain boundaries in a duplex structure and (c) grain refinement during FA mode solidification. The other factors may have a relatively minor but contributory role to play. However, it must be mentioned that the mechanics of the cracking process is still not completely understood.

### 2.4.3 Effect of impurity and alloy elements on solidification cracking

Hull [40] and Borland & Young [36] reviewed the influence of several elements on cracking susceptibility in stainless steels and steel respectively. Accordingly, sulfur, phosphorus, boron, silicon, titanium and niobium were identified as most harmful. They had a strong tendency to segregate at grain boundaries and form low-melting point compounds, resulting in widening the solidification temperature range. Especially, both sulfur and phosphorus were commonly treated and act as impurities that degrade weld ductility and cracking resistance. Fig. 2.5 shows the effect of various elements on the solidification temperature range [41].

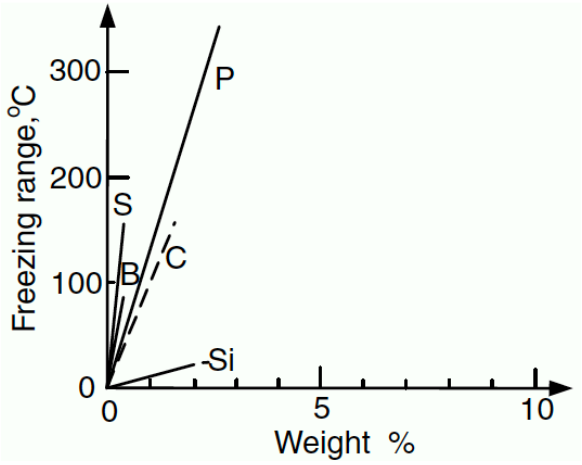



Fig. 2.5 Effect of alloying elements on the solidification temperature range of carbon and low-alloy steels [41].

Sulfur and phosphorus tended to widen the solidification temperature range of steels tremendously. Segregation of phosphorus and sulfur to grain boundaries and formation of residual liquid film believed to be major contributors to hot cracking.

Sulfur has been known to be the most harmful impurity in welding of stainless steels due to the formation of low-melting residual liquid phase along the interdendritic and grain-boundary regions. Sulfur is almost insoluble in all three major constituents of stainless steel, which are chromium, nickel and iron. Sulfur is strongly rejected into the liquid during solidification of austenite, lowering the melting point of the interdendritic liquid. Thus, the potential for forming low-melting eutectics remains strong even with very low contents in austenite [42]. On the other hand, δ-ferrite shows higher solubility for elements like S, P, Si and Nb.

Phosphorus ranks similar to sulfur in the list of elements detrimental to weldability in stainless steels. Sulfur and phosphorus form low-melting eutectics with iron, chromium and nickel. Phosphide eutectics at interdendritic regions have been found to extend the brittle temperature range in varestraint testing to as much as 250 K lower than the solidus in fully austenitic type 310 steel [42]. In 1974, Brooks [43] identified phosphorus as particularly harmful in fully austenitic stainless steels since it has a strong tendency to spread as liquid films. Further, in 1988 Folkhard [13] stated that the low diffusivity of P in both austenite and ferrite phases even at high temperatures suppressed homogenisation.

The harmful effects of sulfur and phosphorus have led to work on addition of other elements that counteract their effects. Manganese additions are well-known to decrease cracking in high-S steels by forming higher-melting MnS-γ eutectics in preference to FeS [40, 44]. Further, the addition of lanthanum, cerium and other rare-earth metals has been found highly effective in binding the P and S as stable compounds [45].

### 2.5 Limits of metallurgical prevention method for solidification cracking

Solidification cracking occurs at the mushy zone [46, 47]. In the final stage of solidification, narrow solid bridges separating areas of low melting liquid are subject to the greatest proportion of the shrinkage induced strains. Solidification cracking occurs due to increase of low melting phase or inherent strain resulting from solidification shrinkage.

Austenitic stainless steel has a high incidence of solidification cracking both in the fusion zone and the partially melted zone of the heat-affected zone. The cracking susceptibility is affected by the presence of low-melting films along grain and sub-grain boundaries. Low-melting elements such as sulfur, phosphorus, silicon and manganese are enriched in the low-melting films [23, 48-50]. Cordea [51] reported that solidification cracking in 310S stainless steel was decreased as a result of reducing sulfur and phosphorus levels of trace amounts. Reducing the silicon content to less than 0.1 mass% was found to be helpful in preventing the continuous liquid film formation along austenite boundaries.

Beneficial effect of δ-ferrite in suppressing the solidification cracking in austenitic stainless steel was first reported in 1941 [52]. Afterwards, Borland [36] and Hull [53] indicated that 5-10 volume percent of δ-ferrite provided optimal resistance to solidification cracking in austenitic stainless steel. Dual phase austenite-ferrite microstructure in as-deposited weld were more resistant to fusion zone solidification cracking than full austenitic microstructure. It is considered that the

greater grain boundary area present in dual phase weldments reduces chances of forming continuous low-melting films along grain boundaries [46, 47]. In addition, δ-ferrite has a great solubility for low-melting elements than austenite during solidification [54].

A number of studies have been conducted to prevent solidification cracking in austenite alloys, but have limitations. Many previous studies reported that reducing low-melting elements (such as sulfur and phosphorus) content increased the solidification cracking resistance [23, 47-50]. However, reducing the sulfur and phosphorus content of stainless steel requires a complicated and costly manufacturing process. Gooch [55] increased manganese contents from 1-2 mass% (normal content) to 5-10 mass% to combine with excess sulfur resulting in increasing solidification cracking resistance. Moreover, Arata [23] increased the carbon content to decrease the extent of micro-fissures due to an increase in the amount of inter-dendritic eutectic was available to backfill the cracks formed at high temperatures. However, these methods resulted in a decrease in the corrosion resistance. Metallurgical prevention methods are effective in preventing solidification cracking, but bring about additional problems. Therefore, we would like to suggest new methods for preventing solidification cracking from a mechanical point of view.

## 2.6 Thermomechanical reason for solidification cracking

A strain is considered to play an important role in the occurrence of thermomechanical cause for solidification cracking. Pellini [37] reported “Strain Theory”. This theory proposed that solidification cracking occurred when an intergranular liquid film was strained beyond some critical value. He indicated that the amount of strain was determined by the film life, as determined by the solidification range and the molten pool cooling rate. When low-melting elements (sulfur or phosphorus) were added to steel, the solidification range would be extended, residual liquid would be exposed to more strain, and there would be a critical strain wouls be reached.

Based on the Pellini’s strain theory [37] Prokhorov [56] and Senda [57] established ductility curves, indicating the minimum ductility required for cracking. Solidification cracking occurred if thermal strain, representing strain across the solid-liquid coexistence area, intersected the ductility curve. Fig. 2.6 shows a schematic example of this approach, where the solidification range defines the solidification initiation temperature ($T_I$) and solidification completion temperature ($T_c$) and the critical ductility curve was determined experimentally [58].

A stress plays a role in any of the cracking mechanisms discussed above including strain due to stress and strain have a relationship through continuum mechanics. In 1972, Chihoski [59] demonstrated how the relative size and location of cells following a moving weld pool would vary with welding parameters, employing an early analysis of the local compression and tension stress cells. Recently, finite element method has been used to evaluate the local stress in weldability studies [60-64]. Zacharia [60] has shown that the trailing end of the mushy zone would experience a tensile stress resulting in cracking by applying a high cross-weld stress in a Sigmajig test (Fig. 2.7).

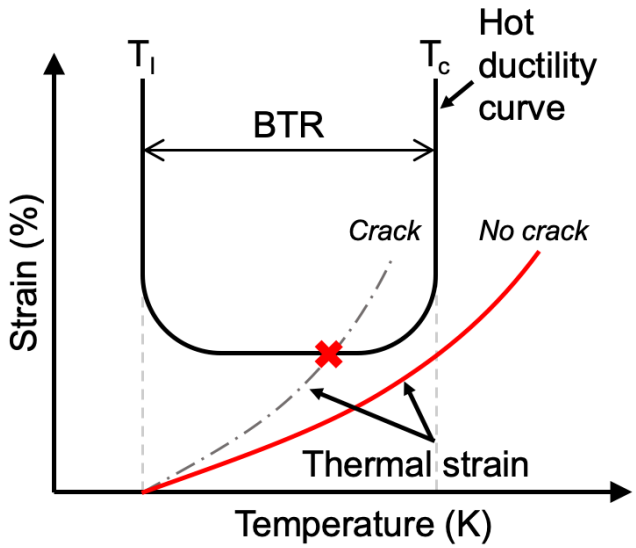



Fig. 2.6 Schematic diagram of hot ductility curve and thermal strain [58].

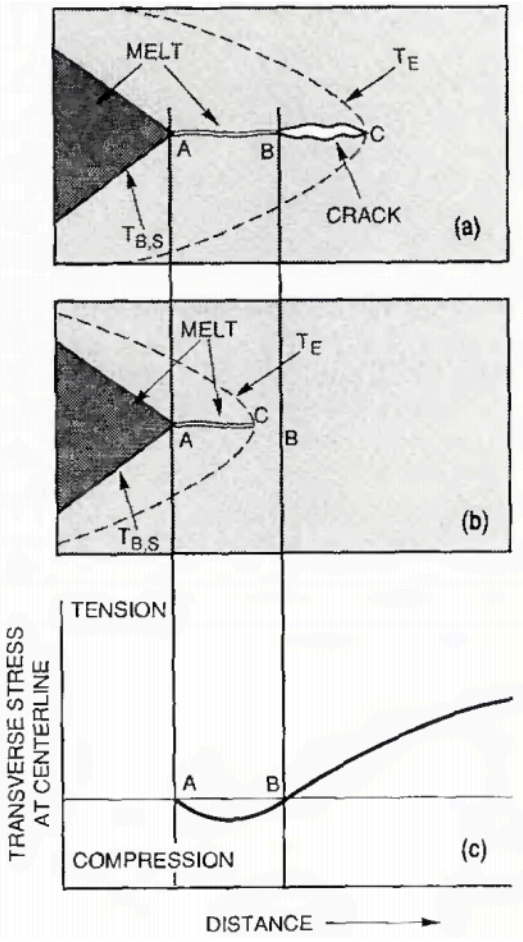



Fig. 2.7 Schematic diagram of two different welds, where the mushy zone of weld avoids solidification cracking by remaining in compression [60].

Besides various experimental, especially Gleeble$^{TM}$ test [65] has been developed in an attempt to measure the strength of mushy zone. A quartz jacket employed to support a molten zone while applying an uni-axial tensile stress. This test has been inconclusive, reflecting the complex nature of deformation of mushy zone.

## 2.7 Evaluation of solidification cracking susceptibility in austenitic stainless steel

The various forms of cracking are generally distinguished by the temperature range over which they generate. "Solidification cracking" is associated with the presence of liquid films along grain boundaries. The cracking occurrence temperature range has been defined as the brittle temperature range (BTR) [66, 67], where the ductility of the weld metal showed a minimum value where weld solidification cracking was possible. The wider the BTR, the more susceptible the material is to solidification cracking. Therefore, the ability to measure the BTR during welding should provide some approximation of material's susceptibility to weld solidification cracking. Several studies of solidification cracking have reported and various theories described the cracking mechanisms. In addition, a number of test techniques have been developed to quantitative assessment of solidification cracking susceptibility.

### 2.7.1 The Transverse Varestraint test

The Varestraint test has been developed to quantify susceptibility to solidification cracking [68]. Lippold et al. [69] developed a new methodology for evaluating cracking susceptibility using the Transverse Varestraint test that provided a measure of the temperature range over which cracking generates (Fig. 2.8).

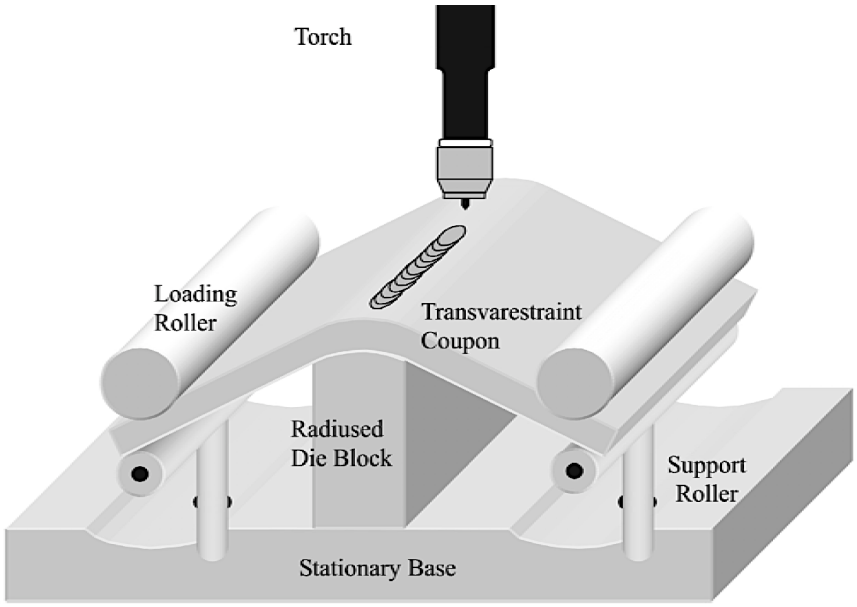



Fig. 2.8 Schematic diagram of transverse varestraint test for evaluating solidification cracking susceptibility [69-71].

This has been termed the solidification cracking temperature range (SCTR) and is a subset of the BTR. To calculate BTR, the temperature history at the centerline of the weld was obtained by inserting a thermocouple behind the arc. The time over which cracking occurs was approximated

by the maximum crack length (MCL) above saturated strain divided by the solidification velocity. Using this approach, SCTR can be calculated using the following relationship, where V represents the welding speed. The SCTR calculation via this approach is shown in Fig. 2.9.

$$SCTR = [Cooling\ rate] \times [MCL/V]$$

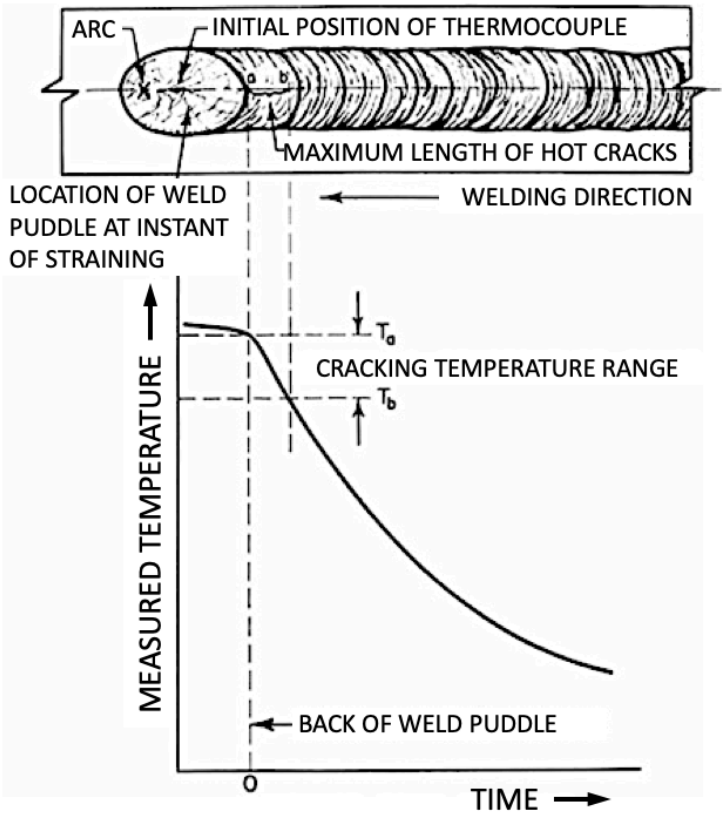



Fig. 2.9 BTR calculation from the SCTR and weld centerline cooling curve.

While the temperature range of cracking is the major component of cracking susceptibility, strain is an essential condition to produce cracking. The BTR can be expressed as a region in temperature-strain space, as shown in Fig. 2.10. Fig. 2.10 shows that the cracking continues down to a lower temperature as strain is increased and that it saturates at a certain minimum temperature. A minimum strain ($\varepsilon_{min}$) is required to initiate cracking called the cracking threshold and also critical strain rate for cracking to occur, as shown in the Fig. 2.10.

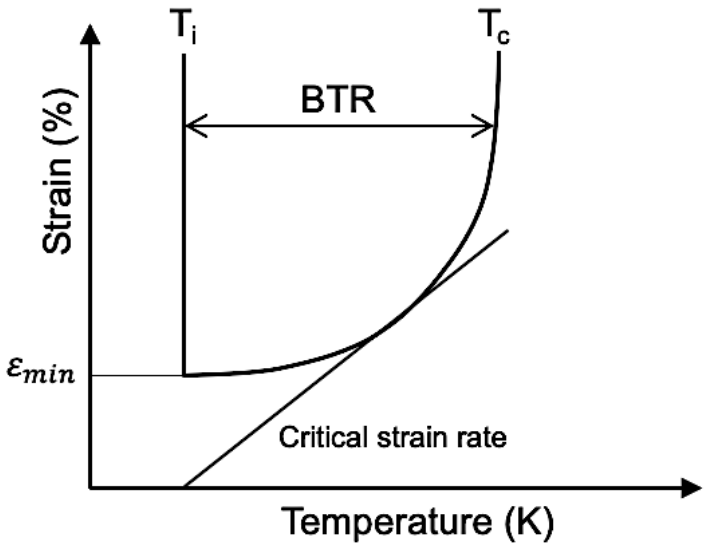
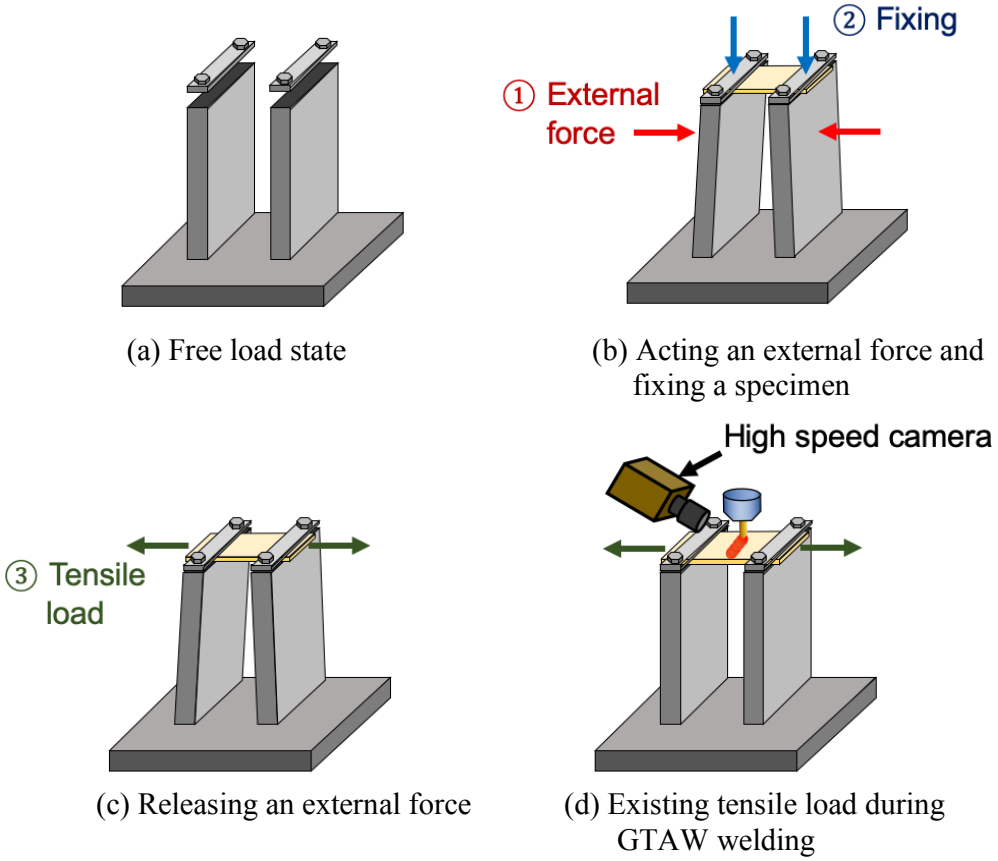



Fig. 2.10 Brittleness temperature range (BTR) during solidification of metal in the strain-temperature graph [57].

### 2.7.2 In-situ observation method in U-type hot cracking test

Based on the concept of deformation energy, the Transverse Varestraint test is well known to provide solidification cracking susceptibility viz. hot ductility curve. However, the strain obtained is the macro-strain of the specimen in the Transverse Varestraint test, which neglects the strain concentration at the trailing edge of the weld pool. The true critical strain for solidification cracking should be local strain happening near the trailing edge of molten weld pool and within the temperature range between the liquidus and the solidus. Many studies using the In-Situ Observation (MISO) has been reported [72-75]. Especially, Matsuda [76] evaluated the local strain in the solidification cracking tips during Gas Tungsten Arc Welding (GTAW). It was found that the Transverse Varestraint test could not provide the appropriate strain in the cracking.

Recently, the U-type hot cracking test has been developed to quantitatively evaluate liquation cracking susceptibility in welding [77]. By adjusting the distance of two restraint beams, different tensile load was performed on the specimen so that weld cracking occurred in the specimen. The schematic diagram of U-type hot cracking test is shown in Fig. 1.12. The external load is applied by fixing the specimen on the restraint beams with initial deflection (Fig. 2.11 (a), (b)). During the GTAW, the specimen is stretched by the transverse tensile load, causing the occurrence of solidification cracking at the centerline of weld bead (Fig. 2.11 (c)). In addition, a high speed camera focused on the trailing edge of the molten pool to record the dynamic deformation. A macro lens is used to observe magnified image and a metal halide lamp is employed for supplying strengthened lightening (Fig. 2.11 (d)).




(a) Free load state

(b) Acting an external force and fixing a specimen

(c) Releasing an external force

(d) Existing tensile load during GTAW welding

Fig. 2.2 Schematic diagram of U-type hot cracking test in in-situ observation method.

### 2.7.3 Difference between Transverse Varestraint test and U-type hot cracking test

The Transverse Varestraint test can evaluate the ductility of weld metal by very simple procedure. Also, hot ductility curve which gives the threshold at which solidification cracking occurrence can be constructed easily. From the hot ductility curve many valuable parameters such as BTR, $\varepsilon_{min}$, and critical strain rate are utilized to discuss the crack susceptibility. F. Matsuda [78, 79] introduced the Means of In-Situ Observation (MISO) technique for $\varepsilon_{min}$ measurement. The $\varepsilon_{min}$ value measured via Transverse Varestraint test is much smaller compared with the MISO technique combined with tensile hot cracking test. Table 2.1 summarizes the value of $\varepsilon_{min}$ measured with the MISO technique and with the Transverse Varestraint test [80-82]. The value of $\varepsilon_{min}$ measured with MISO technique is fairly higher than that measured with the Transverse Varestraint test. However, $\varepsilon_{min}$ measured with the MISO technique combined with the Transverse Varestraint test gives the similar value to that measured with the MISO technique combined with the tensile hot cracking test. This suggests that the low value of $\varepsilon_{min}$ in the conventional Transverse Varestraint test may be caused by disregard for the local strain concentration near the solidification front in excess of nominal strain evaluated by the thickness of specimen and the radius of bending block [80]. In this study, solidification cracking was evaluated using the U-type hot cracking test. Therefore, applying MISO technique combined with the U-type hot cracking test would be appropriate to measure the $\varepsilon_{min}$ rather than the Transverse Varestraint test.

Table 2.1 Comparison of $\varepsilon_{min}$ between the MISO technique and the Transverse

* Submerged arc weld metal ** Designation follows Japan Industrial Standard (JIS)

| Material | | $\varepsilon_{min}$ (%) | | | | | |
|---|---|---|---|---|---|---|---|
| | | MISO technique | | Ordinary Transverse Varestraint test | | | |
| | | Tensile test | Transvers Varestraint test | Ref. 78 | Ref. 80 | Ref. 81 | Ref.82 |
| Plain carbon steel | 08C | 4.9 | - | - | - | - | - |
| | 0.8C-S | 4.3 | - | - | - | - | - |
| | SW* (0.12% C) | - | - | - | 0.5 – 0.75 | - | - |
| | 16C | 4.3 | - | - | - | - | - |
| | SS41** (0.22% C) | - | - | - | < 0.15 | - | - |
| | 30C | 3.4 | - | - | - | - | - |
| | 30C-P | 2.0 | 1.7 | < 0.5 | - | - | - |
| | 50C | 2.1 | - | - | - | - | - |
| | S55** (0.55% C) | - | - | - | < 0.15 | - | - |
| Austenitic stainless steel | SUS304 (L)** | 9.0 | - | - | 0.5 - 0.75 | - | 0.6 |
| | SUS310S** | 2.3 | - | - | < 0.15 | - | 0.08 |
| Aluminum alloy | A5052** | 1.6 | - | - | - | < 0.1 | - |
| | A5083** | 2.1 | - | - | < 0.15 | < 0.1 | - |

# Chapter 3 Proposal and establishment of solidification cracking prediction method

## 3.1 Introduction

Austenitic stainless steel governed by the $Cr_{eq}/Ni_{eq}$ ratio and the P+S content of steel [12, 84-86] is potentially susceptible to solidification cracking. The 310S stainless steel has higher susceptibility to solidification cracking than other types of stainless steels, as it contains residual $\delta$-ferrite from solidification due to its fully austenitic structure; further, the presence of any impurity elements such as P and S greatly influence solidification cracking [25, 87-91]. The susceptibility to solidification cracking during welding is disadvantage for any application of 310S stainless steel, because the fractures in the material due to solidification cracking are directly related to safety problems.

The solidification cracking initiation mechanism during arc welding of stainless steel has been studied previously [92-97]. Lippold [85] reported that the cracking was associated with a shift in weld solidification conditions. Shinozaki [86] reported that a coarse columnar grain size in the weld metal showed a high solidification cracking susceptibility compared with a fine grain size. Based on the Pellini's strain theory [37], Prokhorov [56] and Senda [57] established ductility curves, indicating the minimum ductility required for cracking. Solidification cracking occurred if thermal strain, representing strain across the solid-liquid coexistence area, intersected the ductility curve. However, quantitative assessment of solidification cracking prediction is not adequate. In order to predict solidification cracking occurrence, a hot ductility curve and knowledge of the thermal strain according to welding conditions are necessary. Depending on the presence of any intersection between these two curves, solidification cracking could be predicted.

In this chapter, to predict solidification cracking during gas tungsten arc welding (GTAW) of 310S stainless steel in a U-type hot cracking test, the hot ductility curve and thermal strain was calculated by metallurgical analysis method and finite element method, respectively. A method for the prediction of solidification cracking occurrence was proposed and experimentally verified.

## 3.2 Materials and experimental procedures

### 3.2.1 Material

A type 310S stainless steel with solidification mode A was used. The size of specimen is 100×50×2 mm. The chemical composition of the stainless steel is shown in Table 3.1. For the removal of the surface metal oxides and other tarnishes, the specimen was cleaned by ethanol prior to welding.

Table 3.1 Chemical composition of 310S stainless steel (mass %).

| C | S | P | Cr | Ni | Si | Mn | Co | Fe |
|---|---|---|---|---|---|---|---|---|
| 0.05 | 0.001 | 0.024 | 24.98 | 19.21 | 0.68 | 0.85 | 0.08 | Bal. |

### 3.2.2 U-type hot cracking test

The U-type hot cracking test was performed to occur the solidification cracking by applying stress to the specimen. Fig. 3.1 shows schematic diagram of U-type hot cracking test. The procedure of U-type hot cracking test is following sequence. First, bend the restraint beam with external stress. After that, fix the specimen on top and remove the external stress. From the bent restraint beam, the tensile stress will be applied to the specimen during welding and solidification cracking occurs. In this study, U-type hot cracking test was conducted under the stress condition of 12-17 kN. The specific conditions of the GTAW and the U-type hot cracking test are shown in Table 3.2.

Table 3.2 The conditions of the GTAW in the U-Type hot cracking test.

| Parameters | Values |
|---|---|
| Welding speed (mm/s) | 5 |
| Welding current (A) | 110 |
| Loading strain (kN) | 12-17 |
| Arc length (mm) | 1 |
| Electrode radius (mm) | 2.4 |
| Electrode extension | 15 |
| Electrode angle (°) | 50 |
| Shielding gas | Ar |
| Gas flow rate (l/min) | 20 |

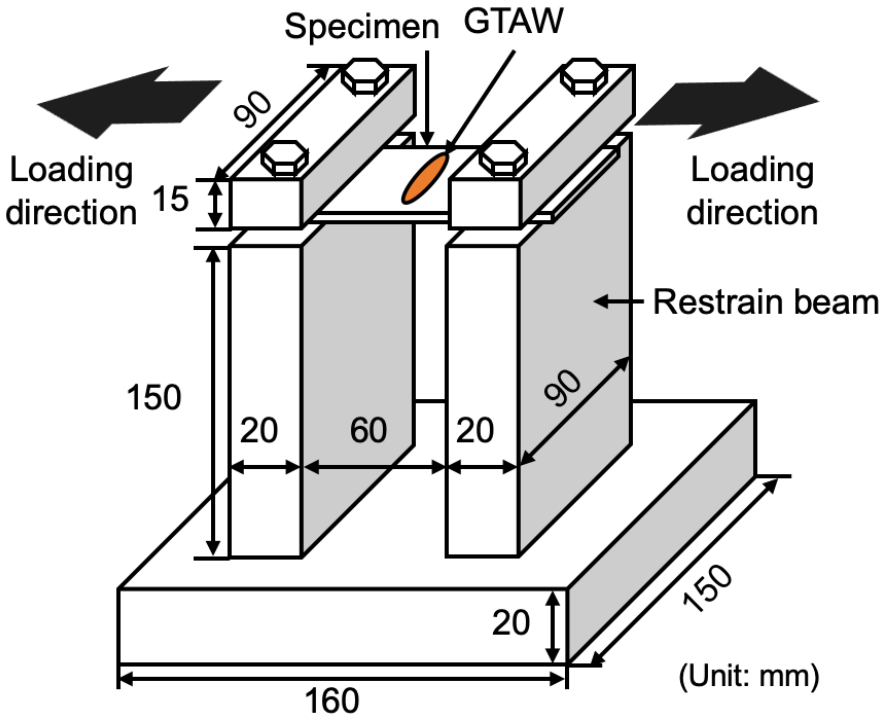



Fig. 3.1 Schematic diagram of the U-Type hot cracking test in GTAW.

### 3.2.3 Solidification cracking observation

Fracture surface of the material in the weld bead was observed by scanning electron microscope (SEM). A high-speed camera was used to measure the critical strain during the U-type hot cracking test (shooting speed: 1000 fps). The images taken using the high-speed camera were converted to the strain curve using the Dipp Motion Pro 2D software program.

### 3.3 Solidification cracking in U-type hot cracking test

Fig. 3.2 shows the weld bead surface after the U-type hot cracking test according to the stress conditions. The cracks did not occur in the condition of 11 kN, but under the conditions of 13kN the cracking occurred at bead location of 35 mm. In the condition of 15kN the cracking occurred at bead location from 30 to 35 mm and in 17 kN the largest crack was observed (bead location: 25-35 mm).

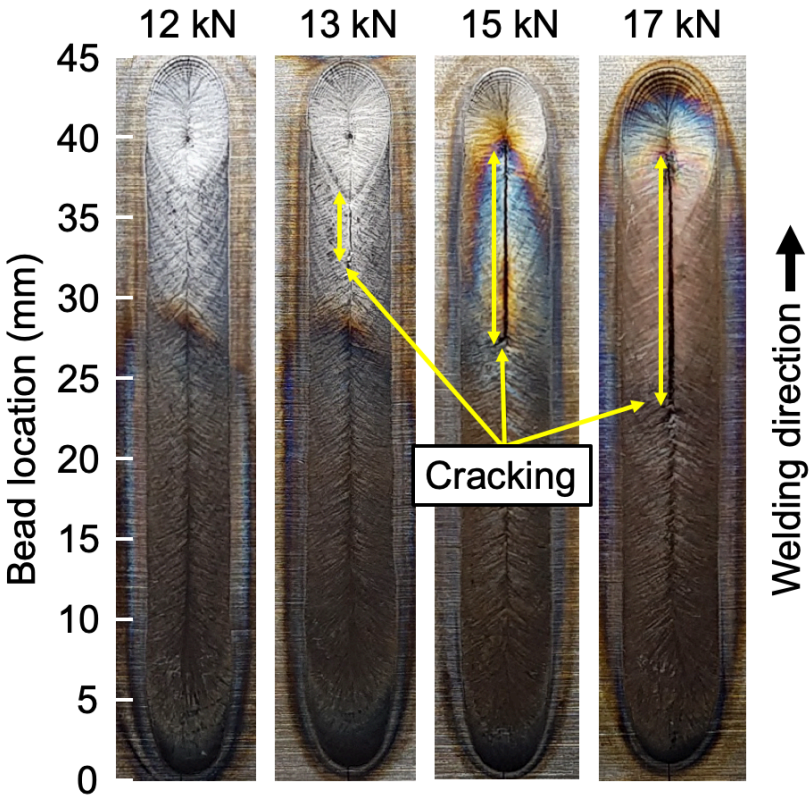
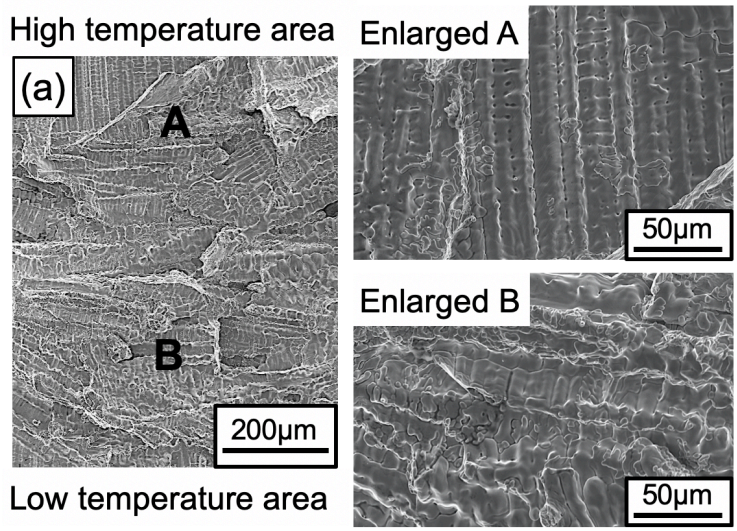
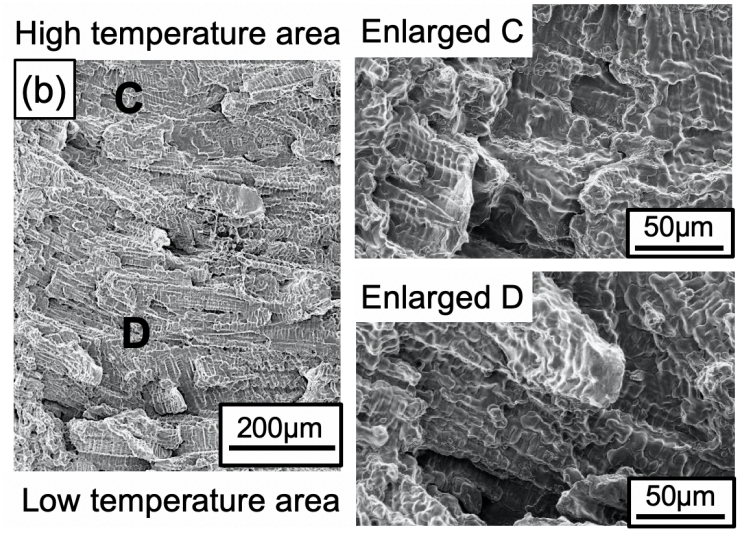



Fig. 3.2 Appearance of the bead surface after the U-Type hot cracking test in the GTAW according to the different stress conditions.

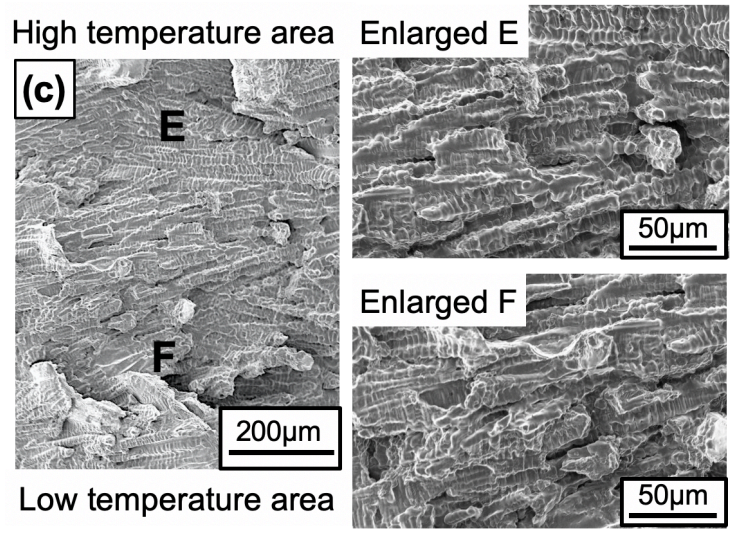
Fig. 3.3 shows the fractography of a crack surface that occurred during the U-type hot cracking test according to the loaded stress conditions (13-17 kN) using SEM. The fracture surface was divided into Regions A-F. These regions were observed from the magnified SEM images (enlarged regions A-F). The fracture morphologies in the high temperature area indicated a dendritic structure, which was regarded as solidification cracking (enlarged region A, C and E). The dendrite structure was also observed in the lower temperature area (enlarged region B, D and F). From the Fig. 3.3, dendrites were observed on the fracture surface, which confirmed the occurrence of solidification cracking.




(a) Fracture microstructure of 13 kN




(b) Fracture microstructure of 15 kN




(c) Fracture microstructure of 17 kN

Fig. 3.3 SEM microstructure of the fracture surface after the U-type hot cracking test.

### 3.4 Basic concept of solidification cracking prediction model

From an thermomechanical point of view, the occurrence of high temperature cracks can be represented by the intersection of thermal strain and hot ductility curve (Fig. 2.6). Based on the Pellini's strain theory [37], Prokhorov [56] and Senda [57] established ductility curves, indicating the minimum ductility required for cracking. Building upon the strain limitation concepts of Prokhorov [56] established ductility curves, defining the maximum strain tolerated before cracking occurs. Cracking will occur if the thermal strain, representing strain of the solid-liquid co-existence zone, intersects the hot ductility curve.

In order to design the solidification cracking prediction model, we approached numerical analysis method to calculate the thermal strain and hot ductility curve according to the welding conditions. The thermal strain according to bead location was calculated using the finite element method. The hot ductility curve was represented by the solidification initiation/completion temperature calculated from metallurgical analysis method in addition to a critical strain measured by the high-speed camera. The specific explanation of solidification cracking prediction model is described in Chapter 3.5-3.9.

### 3.5 Thermal strain calculation using finite element method

#### 3.5.1 Finite element model

The finite element analysis for the thermal strain calculation during the U-type hot cracking test was designed by Quick welder software (Research Center of Computational Mechanics (RCCM), Japan). Exploiting the resulting symmetry, half size of the U-type hot cracking test was established to decrease the calculation time of the finite element method (Fig. 3.4).

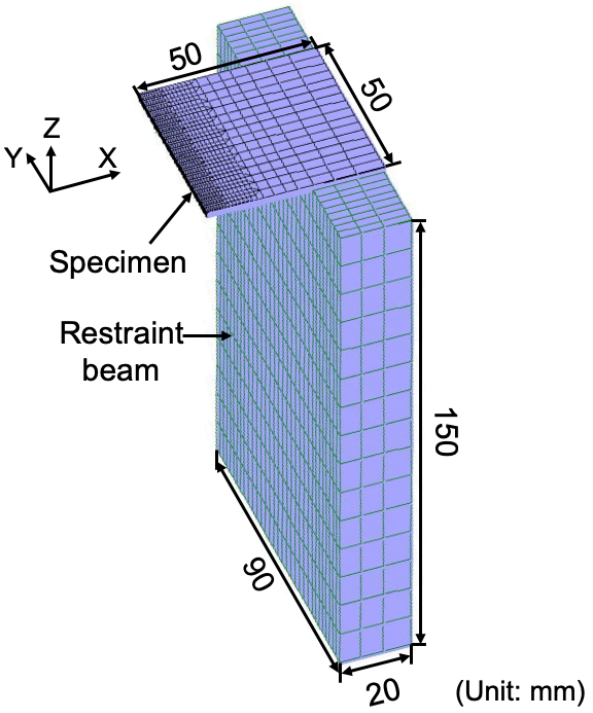



Fig. 3.4 Three dimensional finite element of workpiece.

In the U-type hot cracking test, the restraint beam bended by an external load in order to apply tensile stress to the specimen. The bent restraint beam was restored by the expanded specimen during the welding. Therefore, the tensile stress loaded on the specimen did not constant but decreased. To reproduce this phenomenon, the restraint beam was included in the model and tensile stress loaded from bent restraint beam. The restraint beam of U-type hot cracking test made by carbon steel. The material constants of carbon steel is as follows; Youngs modulus: 205 GPa, Poisson's ratio: 0.3, thermal expansion: $12.18 \times 10^{-5}$ /K, yield strength: 685 MPa, thermal conductivity: 0.053 J/s·m·k, temperature: 298 K. During the welding process, there is no temperature change in the restraint beam, therefore, material constants at room temperature are required rather than the property values according to the temperature. However, material constants of 310S stainless steel according to temperature is essential to calculate the thermal strain of the welds during the U-type hot cracking test. Fig. 3.5 shows the mechanical properties of the 310S stainless steel. Material constants of 310S steel used in this model were referred by Ref. 98-103.

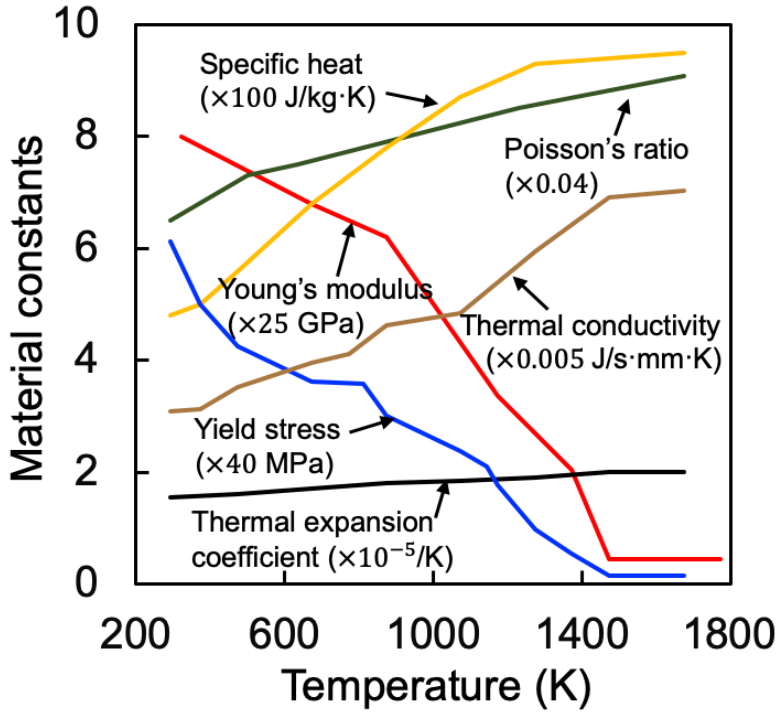



Fig. 3.5 Material constants of 310S stainless steel according to temperature.

### 3.5.2 Comparison of temperature properties and thermal strain between experiment and simulation

In order to confirm the validity of the finite element model during U-type hot cracking test of GTAW, weld bead shape, temperature history and thermal strain were compared. The weld bead shape of GTAW calculated by the simulation was compared with the experimental result (Fig. 3.6). The calculated geometry of the fusion zone was determined by the melting temperature (1673 K) of 310S stainless steel. The depth and width of the weld bead was consistent. The comparison data of the bead shape showed that the simulation and experimental results match well.

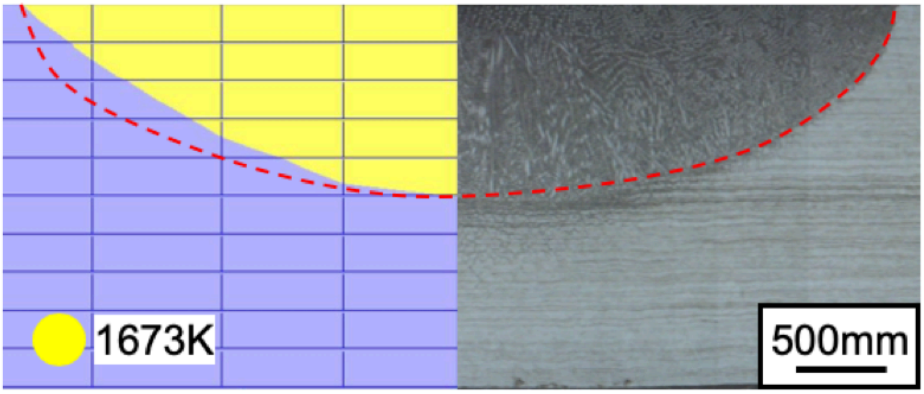
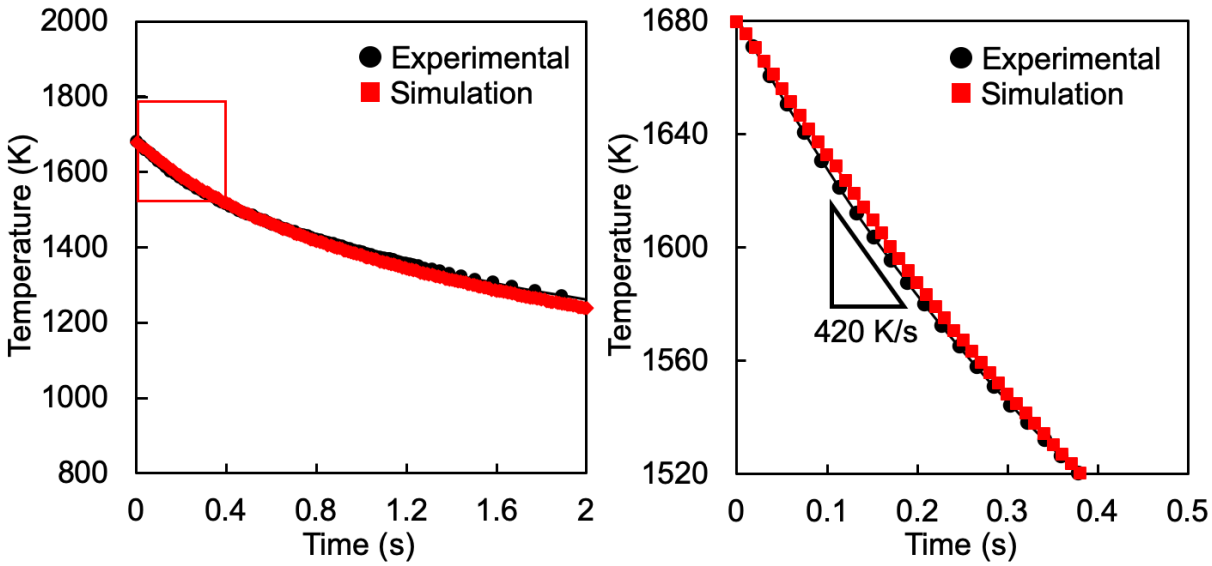



Fig. 3.6 Weld bead shape comparison.

Fig. 3.7 shows temperature history comparison. Fig. 3.7(b) indicates the cooling rate in a solid-liquid co-existence area calculated in Chapter 3.6 (420 K/s). The temperature history in GTAW was measured using a quartz thermocouple which could be measured up to 2473 K. Comparing the temperature history curve between experimental and finite element method, it was confirmed that the both results matched well.




(a) Temperature range: 2000 – 800 K (b) Temperature range: 1680 – 1520 K

Fig. 3.7 Temperature history comparison between experimental result and simulation result.

Fig. 3.8 shows strain-time comparison (loaded stress: 13 kN). The thermal strain according to the gage length was different. However, in the gage length of 2-3 mm, the same values were obtained. The experimental measurement method and difference of thermal strain according to gage length is described in detail in Section 3.5. The experimental and simulation results were in good agreement in both temperature history and strain-time curve. Therefore, the finite element method verified the identical results with the experimental results with respect to the weld bead morphology, temperature history and strain-time curve. The thermal strain according to welding condition was calculated by the finite element method.

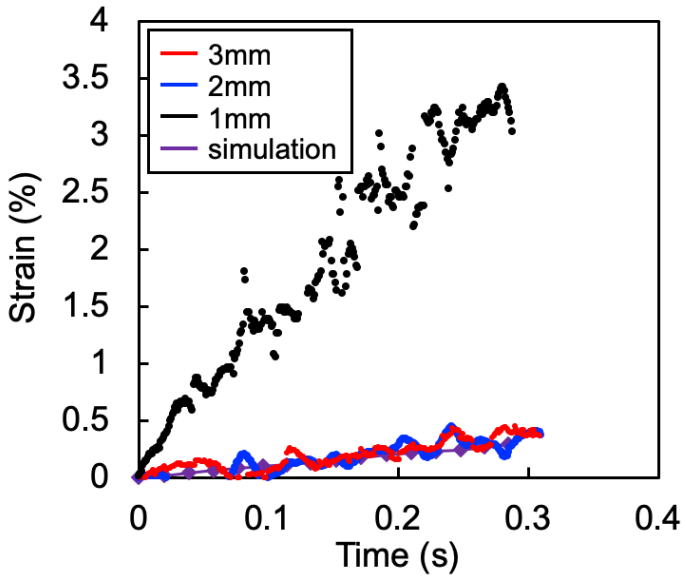
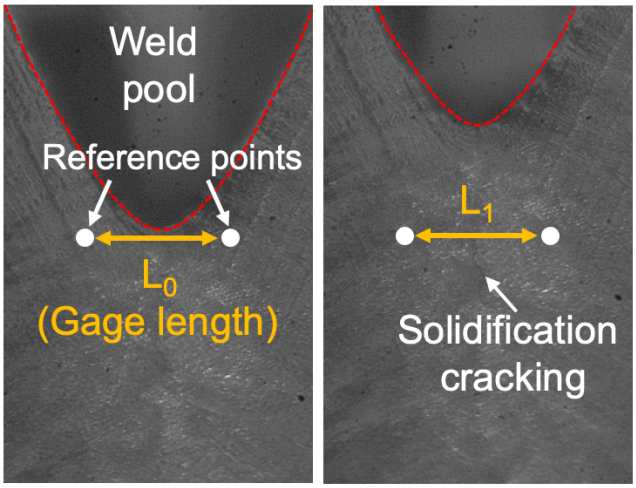



Fig. 3.8 Thermal strain comparison between the thermal elastic-plastic analysis and the in-situ observation method according to the gage length.

### 3.6 Critical strain measurement by in-situ observation technique

The in-situ observation technique is photographic analysis technique that measures the strain of weld bead during solidification. Fig. 3.9 shows pictures of the solidification and solidification cracking occurrence sequence during the U-type hot cracking test. Prior to measure strain curve, two reference points were considered facing each other across the crack initiation point. The distance between two reference points parallel to tensile stress were set as $L_0$ (gage length). The length change between two points ($L_1$) over time was measured using the Dipp Motion Pro 2D software, and the strain-time curve measured by the equation below.

$$\varepsilon(\%) = \frac{L_1 - L_0}{L_0} \times 100 \qquad (1)$$




(a) $T=T_0$ (b) $T=T_1$

Fig. 3.9 Measurement of critical strain using the high speed camera.

Fig. 3.10 shows the dependence of strain-time curve on the gage length in 310S stainless steel. The strain curve increased with an increase in gage length and its scatter was large in the condition of 1mm. Constants gage length cannot be chosen in in-situ observation method, because reference points are considered spontaneously. Therefore, gage length between 2-3mm was determined to be utilized. Matsuda [78] revealed that strain concentration occurred at grain boundaries of columnar crystals from the analysis of the microstructure of the weld metal. Therefore it is understood that the scatter of strain curve in the 1mm condition of gage length in Fig. 3.8 occurred due to the nonuniform strain distribution caused by strain concentration at grain boundaries.

In order to measure the critical strain according to the loaded stress conditions, the in-situ observation method was performed at 12-16 kN. Fig. 3.10 is a strain-time curve measured using Dipp Motion Pro 2D software. During the U-type hot cracking test of each stress condition, the critical strain (ductility required for cracking) was measured. Cracks did not occur in the condition of 12kN, but the cracks occurred in different times at 13-16kN conditions. This result was expressed as the critical strain of the hot ductility curve.

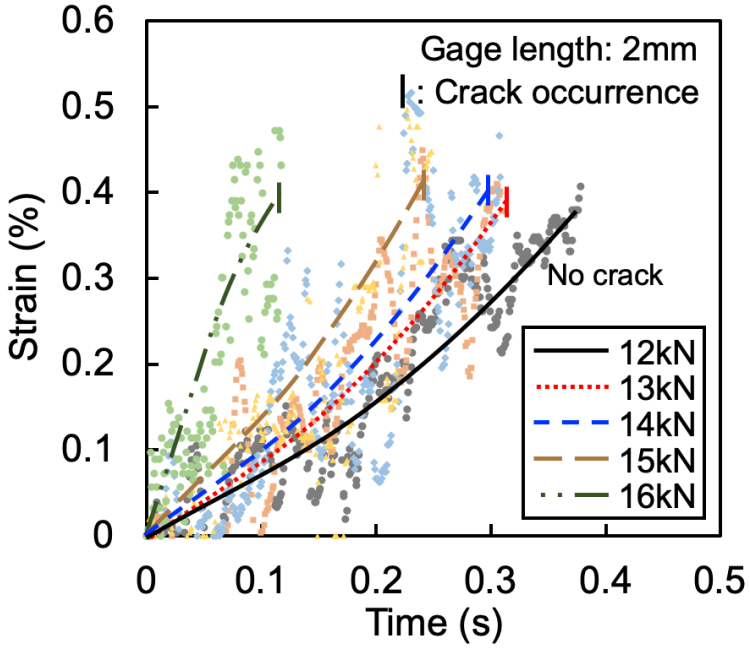



Fig. 3.10 Results of critical strain curves according to loaded stress conditions.

### 3.7 Theoretical approach to solidification cracking susceptibility of GTAW

The solidification brittleness temperature range (BTR) of the material can be expressed by the interval between the solidification initiation temperature and the solidification completion temperature. The BTR of 310S stainless steel was discussed by employing a numerical calculation of the solid/liquid coexistence temperature range. During the welding process, segregation of the solute elements occurs in the residual liquid due to solute element diffusion from the solid (dendrite structure) to the liquid phase. Therefore, the solidification completion temperature is different from the nominal solidus temperature. The solidification initiation temperature and solidification completion temperature were calculated by the KGT and the solidification segregation models, respectively. The validity of this metallurgical model was confirmed in our previous study [104].

### 3.7.1 Calculation of solidification initiation temperature

The solidification initiation temperature was expressed by dendrite-tip temperature. The Kurz-Giovanola-Trivedi (KGT) model, a dendrite growth theory, was extended to multiple system for the calculation[105-108].

The dendrite-tip temperature ( $T_{tip}$ ) can be expressed as the temperature decreased by supercooling $(\Delta T)$ from the equilibrium liquidus temperature ($T_l^{eq}$);

$$T_{tip}(=T_s) = T_l^{eq} - \Delta T \tag{2}$$

$$\Delta T = \Delta T_c + \Delta T_r + \Delta T_k + \Delta T_{cell} \tag{3}$$

$\Delta T_c$ is the constitutional supercooling, $\Delta T_r$ is the supercooling due to curvature of solid liquid interface, $\Delta T_k$ is the kinetic supercooling and $\Delta T_{cell}$ is the cellular supercooling.

Constitutional supercooling $(\Delta T_c)$ is defined as;

$$\Delta T_c = m_i^{eq} C_i^0 - m_i^V C_i^L \tag{4}$$

$m_i^{eq}$ is the equilibrium liquidus gradient of alloy elements, $m_i^V$ is the velocity dependent liquidus gradient, $C_i^0$ is the initial composition of each elements and $C_i^L$ is the liquid concentration at the dendrite-tip. Because equilibrium partitioning cannot be assumed in a rapid solidification process, the theory that considers the deviation from the equilibrium partitioning discussed by Boettinger et al. [109]. The deviation from the equilibrium partitioning was considered and the variation of the partition coefficient with growth velocity was suggested Aziz [110].

$$m_i^V = m_i^{eq}\left\{1 + \frac{k_i^{eq} - k_i^V\left(1 - \ln\frac{k_i^V}{k_i^{eq}}\right)}{1 - k_i^{eq}}\right\} \tag{5}$$

$$k_i^V = \frac{k_i^{eq} + \frac{a_0 V}{D_i^L}}{1 + \frac{a_0 V}{D_i^L}} \tag{6}$$

V is the dendrite growth velocity, $k_i^V$ is the velocity-dependent partitioning coefficient, $k_i^{eq}$ is the equilibrium partitioning coefficient of each element, $D_i^L$ is the temperature dependent diffusion coefficient of the elements in liquid and $a_0$ is the length scale related to the interatomic distance. $C_i^L$ can be explained by the following equations (7-9).

$$C_i^L = \frac{C_i^0}{1 - (1 - k_i^V) I_v(P_i^C)} \tag{7}$$

$$I_V(P_i^C) = P_i^C exp(P_i^C) \int_{P_i^C}^{\infty} \frac{exp(-z)}{z} dz \tag{8}$$

$$R = 2\pi \left( \frac{\Gamma}{\sum_i m_i G_{C,i} \xi_{C,i} - G} \right)^{1/2} \tag{9}$$

$P_i^C$ is the solute Peclet number, $I_V(P_i^C)$ is the Ivantsov's solution, G is the temperature gradient, V is the welding speed and $\xi_i^C$ is the absolute stability coefficient determined as;

$$\xi_i^C = \begin{cases} 1 - \dfrac{2k_i^V}{\sqrt{1 + \left(\dfrac{2\pi}{P_i^C}\right)^2} - 1 + 2k_i^V} & \left(P_i^C \le \dfrac{\pi^2}{\sqrt{k_{V,i}}}\right) \\ \dfrac{\pi^2}{k_i^V P_i^C} & \left(P_i^C \ge \dfrac{\pi^2}{\sqrt{k_{V,i}}}\right) \end{cases} \tag{10}$$

The curvature supercooling ($\Delta T_r$) is expressed as [91, 111];

$$\Delta T_r = -\frac{2\Gamma}{R} \tag{11}$$

and $\Gamma$ is the Gibbs-Thompson parameter.

The kinetic supercooling $\Delta T_k$ is shown below equation (12) [91, 111];

$$\Delta T_k = \frac{V}{u_0} = \frac{R_g T_m^2}{\Delta \mathrm{H}_f V_0} V \tag{12}$$

$u_0$ is the linear interface kinetic coefficient, $V_0$ is the sonic velocity in the liquid, $\Delta \mathrm{H}_f$ is the enthalpy of fusion and $T_m$ is the liquidus temperature of iron.

The cellular supercooling ($\Delta T_{cell}$) is defined as follows [91, 111, 112];

$$\Delta T_{cell} = \frac{GD}{V} \tag{13}$$

With the above equation, the solidification initiation temperature ($T_s$) could be expressed by the following equation (14);

$$T_s = T_l^{eq} - \sum_i m_i^{eq} C_i^0 \left\{ 1 - \frac{1 + \dfrac{k_i^{eq} - k_i^V (1 - ln \dfrac{k_i^V}{k_i^{eq}})}{1 - k_i^{eq}}}{1 - (1 - k_i^V) I_v(P_i^c)} \right\} - \frac{2\Gamma}{R} - \frac{R_g T_m^2}{\Delta H_f V_0} V - \frac{GD}{V} \tag{14}$$

where, $m_i^{eq}$ is the equilibrium liquidus gradient, $C_i^0$ the initial composition, $k_i^{eq}$ the equilibrium partitioning coefficient, $k_i^V$ the velocity-dependent partitioning coefficient, $I_v(P_i^c)$ the Ivantsov solution, Γ the Gibbs–Thompson parameter, $T_m$ the liquidus temperature of pure iron, $\Delta H_f$ the enthalpy of fusion, $V_0$ the sonic velocity in liquid, G the temperature coefficient, and V the solidification velocity. The G indicates cooling rate/welding speed. The cooling rate according to welding conditions will affect the solidification cracking susceptibility.

The material constants used in the calculations are shown in Table 3.3 and 3.4. The calculation conditions are also listed in Table 3.5. The calculation result of solidification initiation temperature was 1680 K.

Table 3.3 Conditions for numerical calculations.

| | |
|---|---|
| Dendrite radius (μm) | 10 |
| Number of mesh division | 100 |
| Solidification rate (mm/s) | 5 (same in all welding condition) |

Table 3.4 Material constants used for the solidification initiation temperature calculation.

| Constants | Value |
|---|---|
| Equilibrium liquidus temperature (K) | 1679 |
| Length scale for solute trapping (μm) | $5.0\times10^{-3}$ |
| Gas constant (J/mol·K) | 8.3145 |
| Liquidus temperature of pure Fe (K) | 1803 |
| Sonic velocity in liquid (μm/s) | $2.0\times10^{9}$ |
| Gibbs-Thomson coefficient (Km) | $3.2\times10^{-7}$ |
| Enthalpy of fusion (J/kg) | 237201 |

Table 3.5 Material constants used in the numerical analysis of solidification segregation.

| Constants | C | S | P | Cr | Ni | Si | Mn |
|---|---|---|---|---|---|---|---|
| Equilibrium partition coefficient in $\gamma$ | 0.40 | 0.02 | 0.11 | 0.88 | 0.95 | 0.61 | 0.85 |
| Equilibrium liquidus gradient in $\gamma$ (K/mass%) | -39.6 | -21.0 | -20.6 | -1.96 | -2.20 | -12.1 | -3.71 |
| Diffusion coefficient in liquid ($10^{-7}m^2/s$) | 5.20 | 41.4 | 0.43 | 2.67 | 4.92 | 0.51 | 4.6 |
| Activation energy for diffusion in liquid (kJ/mol) | 19.1 | 87.9 | 33.5 | 67.2 | 68.0 | 38.4 | 70.6 |
| Diffusion coefficient in $\gamma$ ($10^{-4}m^2/s$) | 2.30 | 0.75 | 8.70 | 0.17 | 0.77 | 0.30 | 0.16 |
| Activation energy for diffusion in $\gamma$ (kJ/mol) | 148 | 236 | 273 | 264 | 281 | 252 | 262 |

### 3.7.2 Calculation of solidification completion temperature

The solidification completion temperature was based on the segregation concentration of the solute in the residual liquid during solidification. The solidification segregation model is based on the non-equilibrium solidification diffusion model proposed by Morishita et al [113]. The finite difference method was used assuming that the dendrite cross-section is a two dimensional hexagonal (Fig. 3.11).

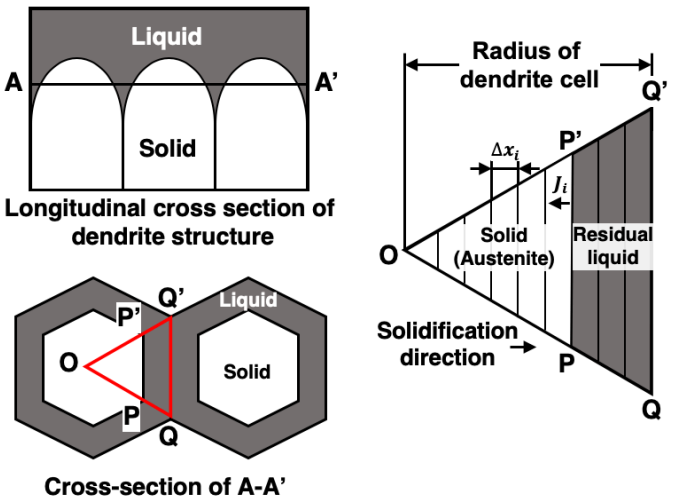



Fig. 3.11 Schematic illustration of the analysis model for calculation of solidification completion temperature. (solidification segregation model).

The distribution of the solute elements during the solidification process was determined by solving the diffusion equation for both solid and liquid phases. The diffusive flux $J_i$ from a segment $i$ to a segment $i+1$ is given by Fick's law;

$$J_i = D\frac{C_{i+1} - C_i}{\Delta x} \tag{15}$$

$D$ is the diffusion coefficient of solute, $C_i$ is the concentration in segment $i$ and $\Delta x$ is the segment width. The solute concentrations of liquid and solid phase at the solid-liquid interface were calculated by the following equation (16);

$$C_i^S = k_{nes}^{S/L} \cdot C_{i+1}^L \tag{16}$$

$k_{nes}^{S/L}$ is the velocity dependent partitioning coefficient.

The variation of each solute concentration with the solidification is expressed by the following equation (17);

$$\Delta C_i = \frac{2D\Delta t}{\Delta x_i(S_i + S_{i-1})}\left\{S_i\frac{C_{i+1}^b - C_i^b}{\Delta x_i} - S_{i-1}\frac{C_i^b - C_{i-1}^b}{\Delta x_{i-1}}\right\} \tag{17}$$

The $S_i$ is the surface area from element 1 to element $i$ (equation 18);

$$S_i = \frac{1}{\sqrt{3}}\left(\sum_{k=1}^{i} \Delta x_k\right)^2 \tag{18}$$

Considering the law of conservation of mass segregation concentration was calculated using the equation (19) following below.

$$\left(\sum_{k=1}^{N} \Delta x_k\right)^2 \cdot C_0 = \sum_{i=1}^{N}\left\{\left(\sum_{k=1}^{i} \Delta x_k + \sum_{k=1}^{i-1} \Delta x_k\right) \cdot \Delta x_i \cdot C_i^S\right\} + \sum_{i=j+1}^{N}\left\{\left(\sum_{k=1}^{i} \Delta x_k + \sum_{k=1}^{i-1} \Delta x_k\right) \cdot \Delta x_i \cdot C_i^L\right\} \tag{19}$$

Tables 3.3-3.5 list the material constants and calculation conditions. The segregation concentration of each solute element derived by the solidification segregation model was converted into temperature using Thermo-Calc software program and the result of solidification completion temperature was 1520 K.

### 3.8 Evaluation of solidification cracking susceptibility in GTAW

A hot ductility curve was obtained based on a combination of the solidification initiation and completion temperatures, in addition to the critical strain. The solidification initiation and completion temperatures in GTAW were 1680 K and 1520 K, respectively. The BTR calculated by the metallurgical analysis was determined to be 160 K. The horizontal axis of the measured critical strain (Fig. 3.10) was converted from time to temperature using the cooling rate (Fig. 3.7). The solidification initiates at 0 s in Fig. 3.10 at the temperature of 1680 K. The time axis is then modified to a temperature axis by calculating the temperature reduction amount according to the cooling rate (420 K/s). Fig. 3.12 shows the hot ductility curve of GTAW.

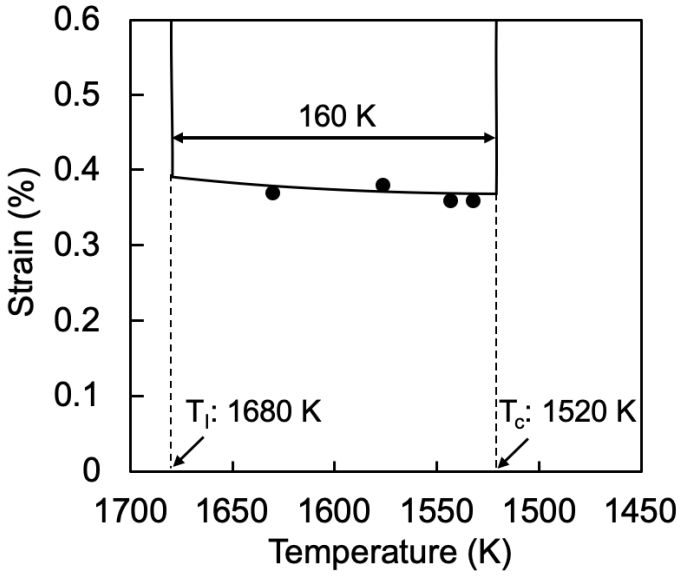
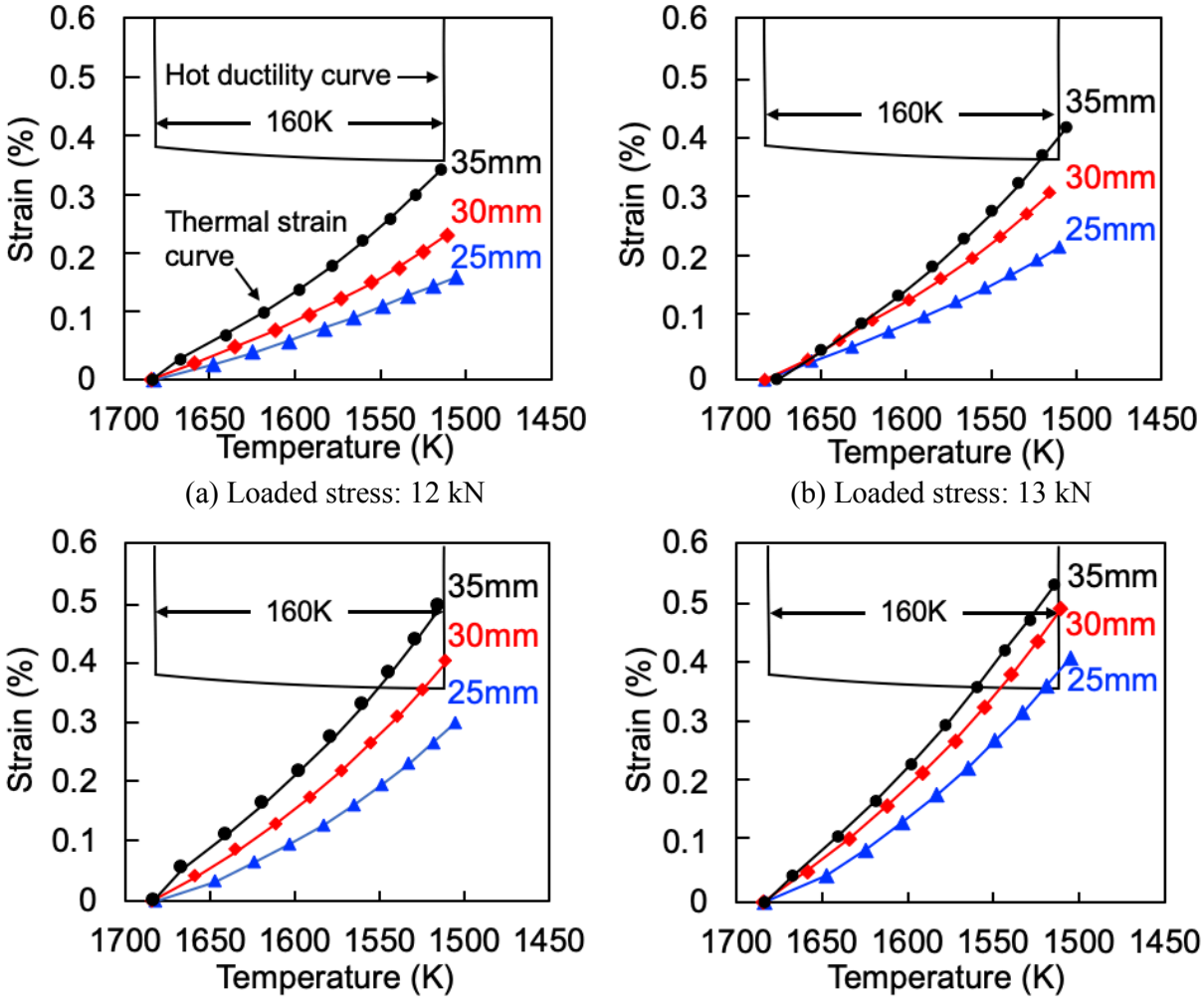



Fig. 3.12 Hot ductility curve in GTAW during U-type hot cracking test.

### 3.9 Prediction results of solidification cracking

Building upon the strain limitation concepts of Prokhorov [56] established ductility, the maximum strain tolerated before cracking was defined. Cracking will occur if the thermal strain, representing strain of the solid-liquid co-existence zone, intersects the hot ductility curve. Fig. 3.13 shows the high temperature ductility and thermal strain according to bead location and loaded stress conditions.



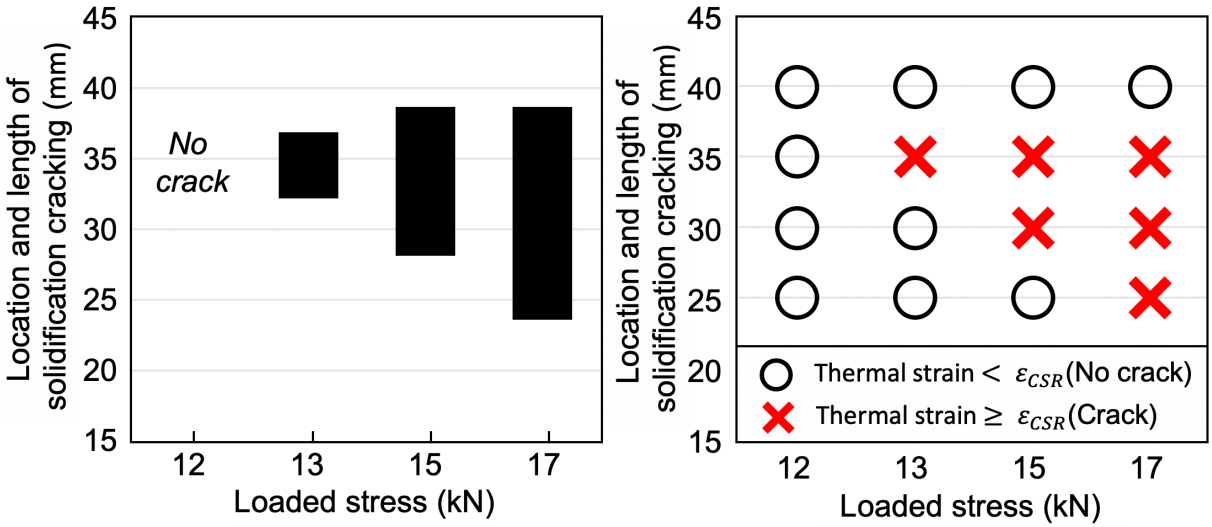

(a) Loaded stress: 12 kN (b) Loaded stress: 13 kN

(c) Loaded stress: 15 kN (d) Loaded stress: 17 kN

Fig. 3.13 Comparison between the thermal strain and the hot ductility curve in the different loaded stress conditions.

With each loaded stress condition, the thermal strain along the welding direction increased due to an increase in the amount of heat input on the specimen during welding. In addition, these curves were changed by variations in the loaded stress. For the condition of 12 kN, the intersection between the hot ductility curve and the thermal strain did not appear. However, as the loaded stress was increased, the intersection of these two curves also increased, which implied that the solidification cracking was elongated according to the loaded stress. In Fig. 3.13 (b), at a bead location of 35 mm, the hot ductility curve intersected the thermal strain at a point when solidification cracking was expected to occur. As the stress increased, the point of intersection of these two curves increase

with increasing slope of the thermal strain. Therefore, the length of the solidification cracking was also elongated. In Fig. 3.14, the location and length of the solidification cracking observed during the actual U-type hot cracking test (a) were compared with the prediction result (b). Fig. 3.14 shows the corresponding results between the actual U-Type hot cracking test (a) and the solidification cracking prediction model (b). Therefore, it was possible to predict the occurrence, as well as the length of the solidification cracking using the crack prediction model.




(a) Experiment result (b) Prediction model result

Fig. 3.14 Comparison between the actual U-type hot cracking test result.

### 3.10 Proposal of thermal strain control for solidification cracking prevention

The thermal strain and hot ductility curve in Fig. 3.13 show the solidification cracking behavior according to the tensile stress during the U-type hot cracking test. The hot ductility curve was constant due to the constant GTAW condition (Fig. 3.12). However, thermal strain was differed by loaded stress.

The thermal strain under different loads in the U-type hot cracking test was calculated by using the finite element method. The solidification was started with the weld metal cooling down. When the temperature fell down below the coherent temperature, the weld metal started exhibiting the characteristic of solid metal. Fig. 3.13 shows the thermal strain with temperature drop during solidification temperature range, which is considered as the mechanical driving force of solidification cracking. It could be seen that the thermal strain was increased with an increase in the loaded stress, and it became to cross the hot ductility curve when the initial load exceeded 13 kN, which meant that solidification cracking was much possible to occur due to the high thermal strain rate. Therefore, the thermal strain was increased with an increase in tensile stress. In addition, as welding progressed, the slope of the thermal strain was also increased due to an increase in the amount of deformation of the weld. As welding progressed, the slope of thermal strain was increased by accumulated temperature of the specimen during the welding.

From the solidification cracking prediction model, we found that the main factor governing the behavior of the solidification cracking was not hot ductile curve but thermal strain, due to the

increased in loaded stress. Therefore, we focus on the thermal strain control to prevent solidification cracking.

### 3.11 Summary

In this chapter, solidification cracking prediction model was designed to predict the solidification cracking that occurs during U-type hot cracking tests in GTAW of 310S stainless steel. A solidification cracking occurrence during the U-Type hot cracking test in the GTAW was observed through the relationship between the hot ductility curve and thermal strain.

The summarized conclusions are as follows;

1) The hot ductility curve was obtained based on a combination of the solidification initiation and completion temperatures, in addition to the critical strain. Solidification initiation and completion temperatures were calculated by metallurgical analysis model; viz. KGT model (supercooling) and solidification segregation model, respectively.

2) The thermal strain was calculated using the finite element model. The finite element method verified the identical results with the experimental results with respect to the weld bead morphology, temperature history and strain-time curve.

3) The intersection between the hot ductility curve and the thermal strain increased with an increase in the loaded stress. In the actual test, solidification cracking did not occur under the conditions of 12 kN, but the cracks elongated according to the loaded stress. The solidification cracking occurrence in the actual test corresponded with the prediction results.

# Chapter 4 Effects of laser in-situ post heating on solidification cracking behavior

## 4.1 Introduction

Cr-Ni base austenitic stainless steel is applied to various energy industries such as fuel cells, gas and nuclear power because of its beneficial properties including corrosion resistance, and its maintenance and mechanical properties under a demanding service environment. However, stainless steel, such as 310S, is highly susceptible to solidification cracking during welding; several studies have attempted to resolve this problem.

A stainless steel has a problem of solidification cracking during welding, and especially, austenitic stainless steel (Type 310S) has a high solidification cracking susceptibility [83, 84]. The FCC structure disturbs rapid diffusion of impurity elements (low melting elements such as S and P) in stainless steels [36]. This increases the segregation tendency of impurity elements along weld metal grain boundaries and increases the volume fraction of liquid films coating the grain boundaries at the end of solidification. An increase in the volume fraction of liquid films accelerates the propagation of solidification cracking.

To date, the mechanism of solidification cracking propagation has been studied and developed in various aspects over the past years. In 1988, Guven and Hunt [28] explained the role of tensile stresses in the solidification cracking formation. In 1999, Rappaz [32] proposed the RDG model associated with tensile deformation of the solidified material. In 2015, Kou [30] focused on the grain boundary, such as liquid feeding between grains, separation of grains from each other and lateral growth of grains toward each other. Several factors were reported on the solidification cracking propagation, however, thermomechanical aspect of occurrence of solidification cracks is insufficient.

The objective of this chapter is the quantitative assessment and understanding of thermomechanical factors affecting the solidification cracking behavior. Solidification cracking can be elucidated by the intersection between the hot ductility curve and thermal strain. The laser beam was irradiated behind the molten pool during the GTAW to change the solid-liquid co-existence zone and the solidification cracking behavior was compared. Based on welding conditions, the hot ductility curve and thermal strain were calculated using a theoretical analysis method and simulation, respectively. The quantitative evaluation of factors affecting the solidification cracking behavior was compared.

## 4.2 Materials and experimental procedures

### 4.2.1 Material

A type 310S stainless steel with solidification mode A was used. The size of specimen is 100×50×2 mm. The chemical composition of the steel is shown in Table 3.1. For the removal of the surface metal oxides and other tarnishes, the specimen was cleaned by ethanol prior to welding.

### 4.2.2 U-type hot cracking test with in-situ laser post heating

An in-situ laser post heating was conducted to control solid-liquid co-existence zone of the weld bead during the U-type hot cracking test (Fig. 4.1). The loaded stress condition is 13 kN. A fiber laser beam was irradiated behind the molten pool during the GTAW. In this study, U-type hot cracking test was conducted under the stress condition of 13 kN. The specific conditions of the GTAW and the U-type hot cracking test are shown in Tables 4.1 and 4.2.

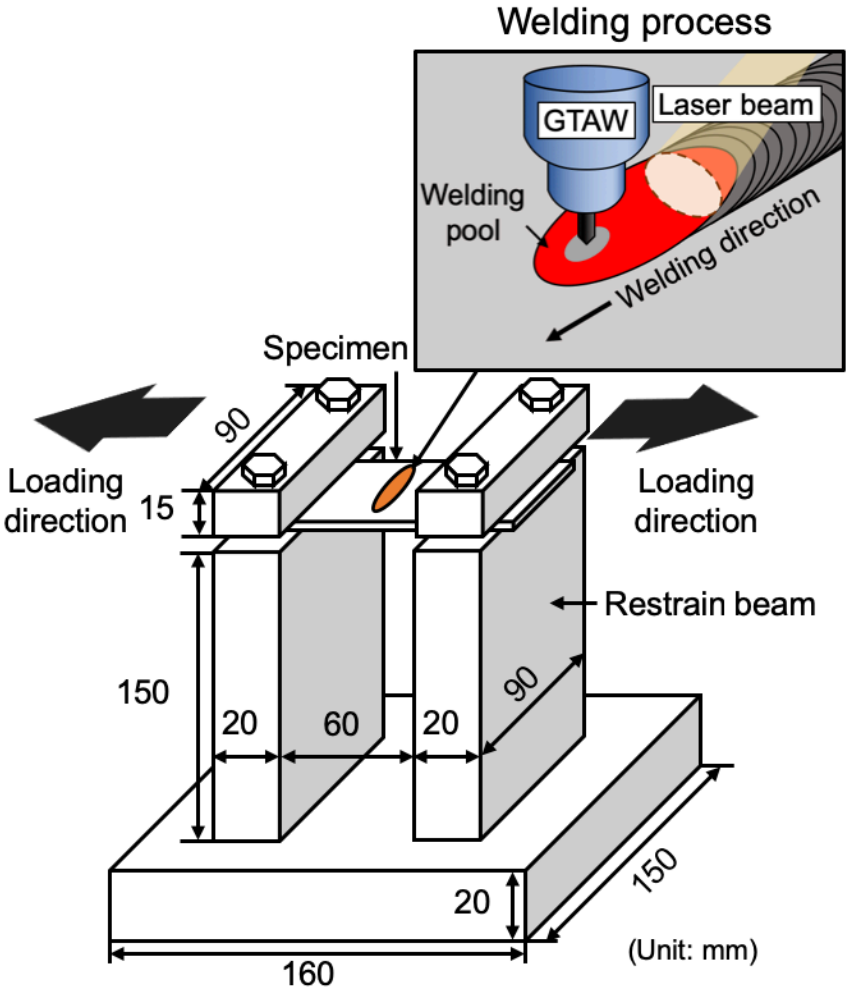



Fig. 4.1 Schematic illustration of the GTAW-laser welding during the U-Type hot cracking test.

Table 4.1 Laser beam conditions in U-type hot cracking test.

| | Parameters | Values |
|---|---|---|
| Laser | Distance between GTAW and laser (mm) | 10 |
| | Laser power (kW) | 0-0.4 |
| | Laser angle (°) | 32 |
| | Defocus length (mm) | 200 |
| | Laser spot size (mm) | 10 |

Table 4.2 GTAW conditions in U-type hot cracking test.

| | Parameters | Values |
|---|---|---|
| GTAW | Welding speed (mm/s) | 5 |
| | Welding current (A) | 110 |
| | Arc length (mm) | 1 |
| | Electrode radius (mm) | 2.4 |
| | Electrode extension (mm) | 15 |
| | Electrode angle (°) | 50 |
| | Shielding gas | Ar |
| | Gas flow rate (l/min) | 20 |

The U-type hot cracking tests were conducted under following conditions;

1. Laser power change
2. Distance change between laser and arc
3. Laser spot size change

In laser power change test, laser beam power of 0.2 kW and 0.4 kW were irradiated in the molten pool. In distance change between heating sources test, distance was changed by 8 mm, 10 mm and 15 mm (laser power: 0.2 kW). The laser in-situ post heating was performed under conditions of 8 mm, 10 mm and 12 mm laser spot size (laser power: 0.2 kW). The effect of heat input on solidification cracking during U-type hot cracking test under three laser conditions was investigated. The laser conditions were set within a range where the bead penetration depth did not change.

### 4.2.3 Solidification cracking observation

Optical microscope (OM) was used to observe the surface of the weld bead. Fracture surface of the material in the weld bead was observed by scanning electron microscope (SEM). In-situ observation method was performed under 13 kN stress conditions to compare the difference in critical strain according to the heat input change of molten pool. A high-speed camera was used to measure the critical strain rate during the U-type hot cracking test (shooting speed: 1000 fps). The images taken using the high-speed camera were converted to the strain curve using the Dipp Motion Pro 2D software program.

## 4.3 Solidification cracking according to laser beam condition

The solidification cracking behavior according to welding conditions was observed using OM. Figs. 4.2-4.4 show the weld bead surface after U-type hot-cracking test results for the various welding conditions (Loaded stress: 13 kN). In the GTAW process (Fig. 4.2), cracks were observed in the weld bead (bead location: 35 mm). However, the degree of cracking increased upon the application of 0.2 kW laser heating (bead location: 30-35 mm). The largest cracks were observed

with 0.4 kW laser heating (bead location: 25-35 mm). The solidification cracking increased according to an increase in laser power.

Fig. 4.3 shows the weld bead surface according to distance change between laser and arc (loaded stress: 13 kN and laser power: 0.2 kW). In the condition of 8 mm, cracks were observed in the weld bead (bead location: 30-35 mm). In the condition of 10 mm, the degree of cracking was constant upon the application of 10 mm condition (bead location: 30-35 mm). The largest crack was observed in the condition of 15mm (bead location: 25-35 mm). The solidification cracking was increased according to distance between heating sources increase.

Fig. 4.4 shows the weld bead surface according to laser spot size change (loaded stress: 13 kN and laser power: 0.2 kW). In the beam size condition of 8 mm, cracks were observed in the weld bead (bead location: 30-35 mm). However, the degree of cracking was slightly decreased upon the beam size of 10 mm (bead location: 30-35 mm). The smallest cracks were observed under the condition of 12 mm (bead location: 30-35 mm). Drastic change of the solidification cracking was not observed according to the change in laser spot size.

The fractograph according to welding conditions was observed using SEM images. Fig. 4.5 shows the fracture microstructure according to laser power change. Fig. 4.6 and Fig. 4.7 show the fracture microstructure according to distance change between heating sources and laser spot size change, respectively. The fracture surface was divided into Regions a-i. These regions were observed from the magnified SEM images (enlarged Regions a-i). As can be seen from both images, the solidification cracking surface indicated the dendritic structure.

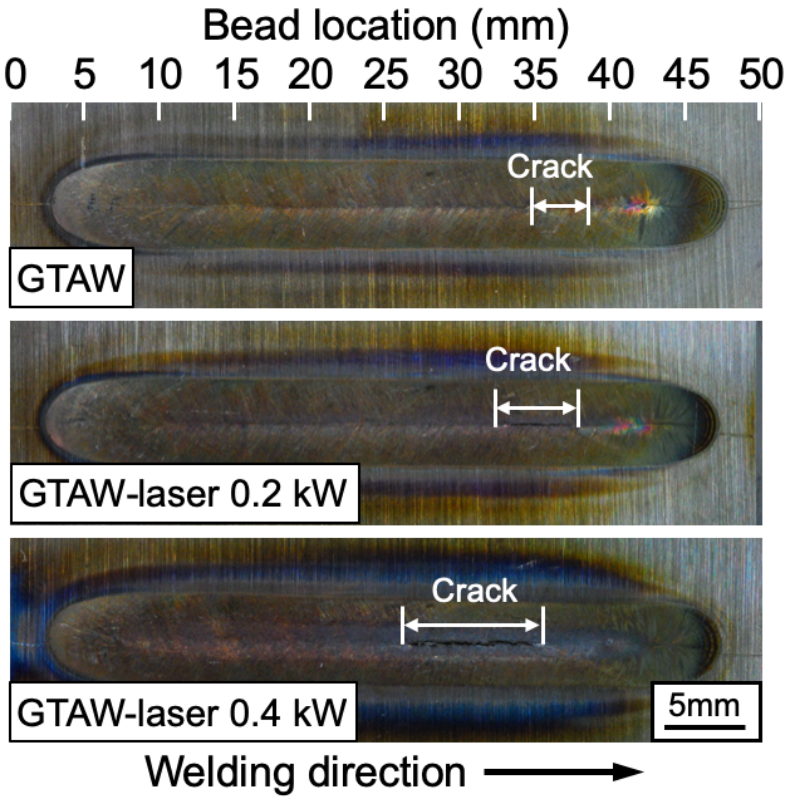



Fig. 4.2 Observation of the solidification cracking behavior according to laser power change. (Distance between heat source: 10 mm, Laser spot size: 10 mm)

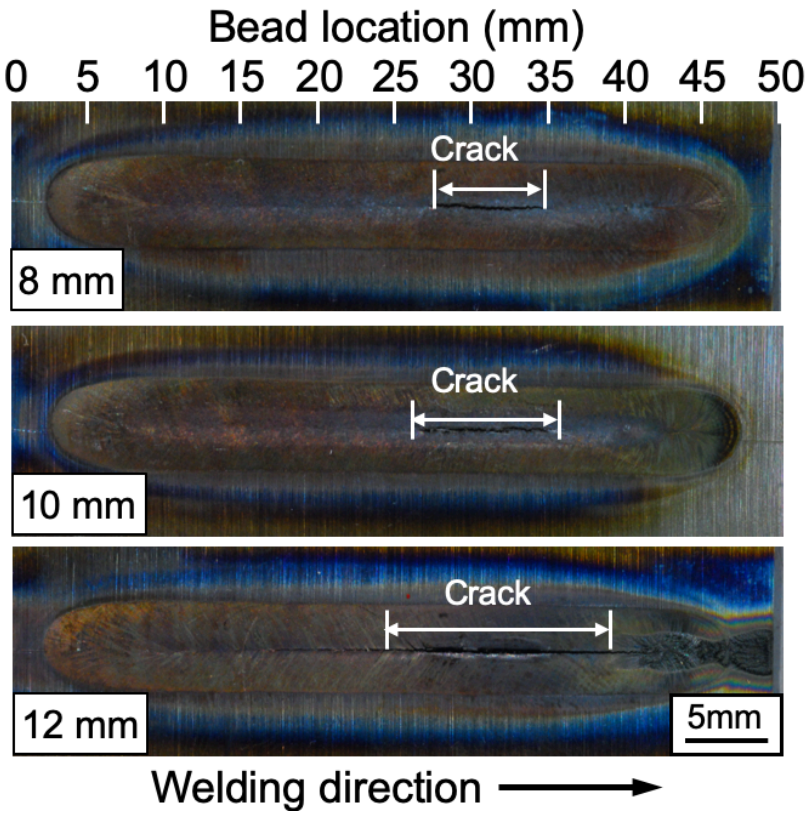



Fig. 4.3 Observation of the solidification cracking behavior according to distance change between laser and GTAW. (Laser power: 0.2 kW, Laser spot size: 10 mm)

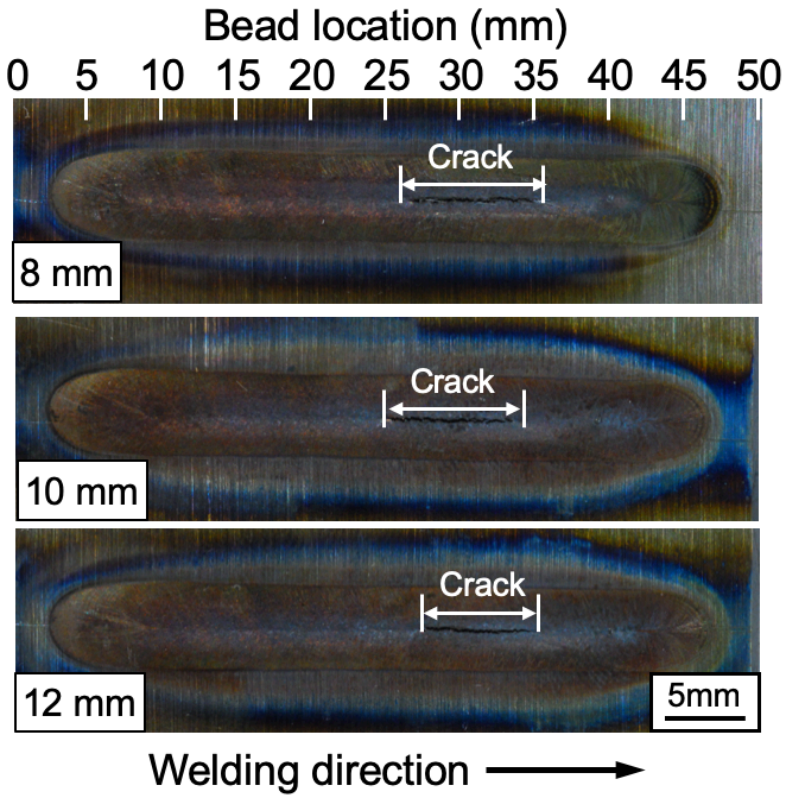



Fig. 4.4 Observation of the solidification cracking behavior according to laser spot size change. (Distance between heat source: 10 mm, Laser power: 0.2 kW)

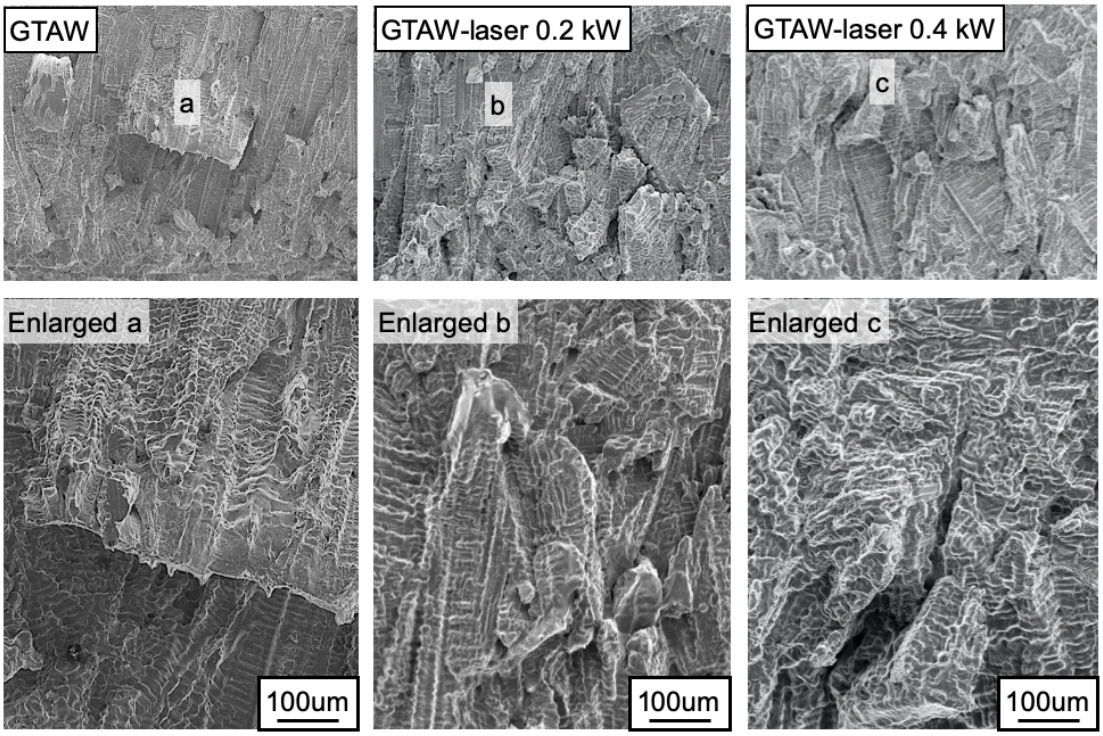



Fig. 4.5 Fractography observation according to laser power change.
(Distance between heat source: 10 mm, Laser spot size: 10 mm)

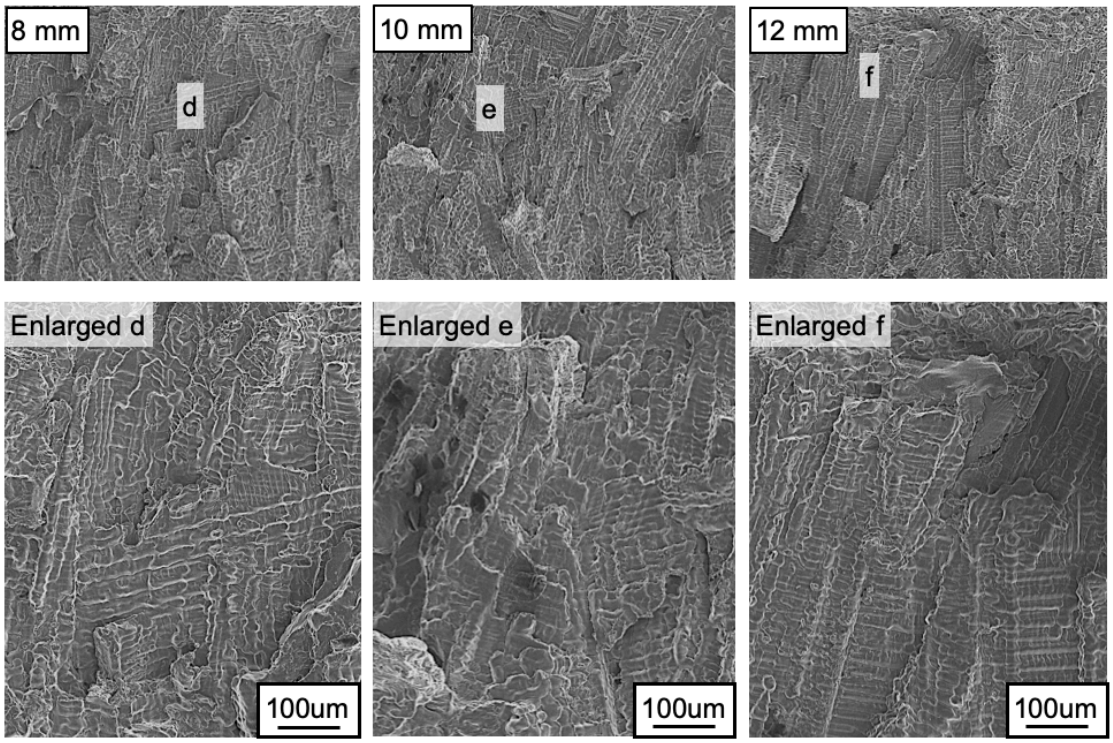



Fig. 4.6 Fractography observation according to distance change between laser and GTAW.
(Laser power: 0.2 kW, Laser spot size: 10 mm)

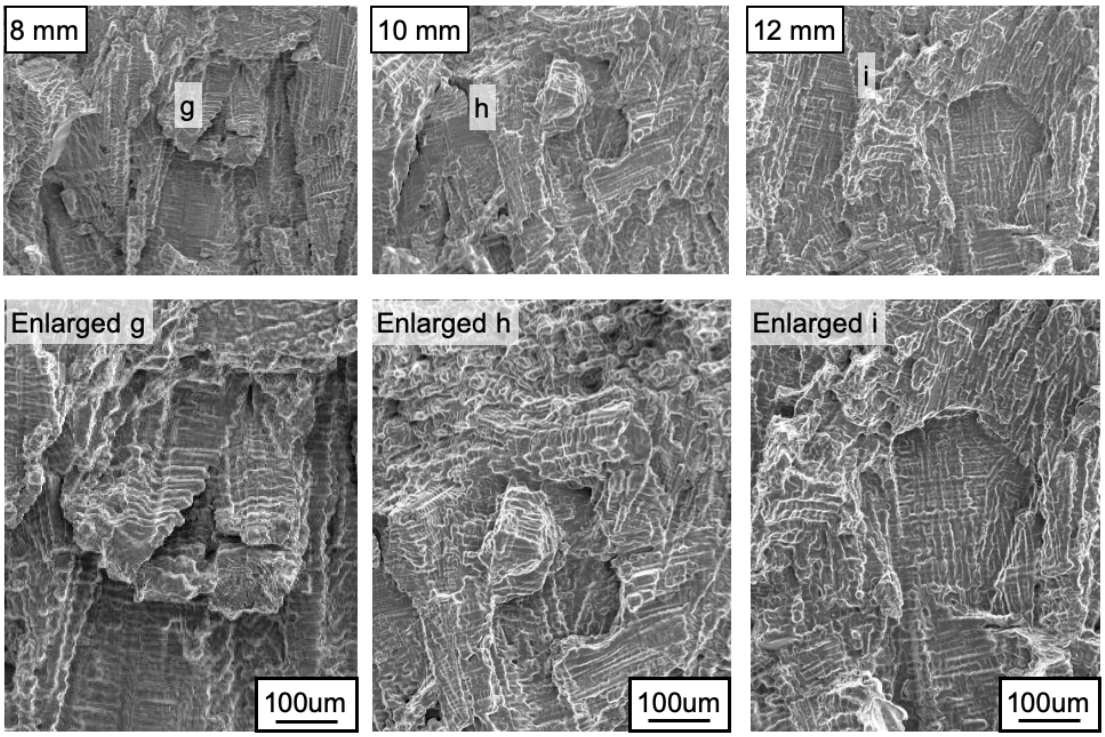



Fig.4.7 Fractography observation according to laser spot size change.
(Distance between heat source: 10 mm, Laser power: 0.2 kW)

## 4.4 Thermal strain calculation using finite element method

### 4.4.1 Finite element model

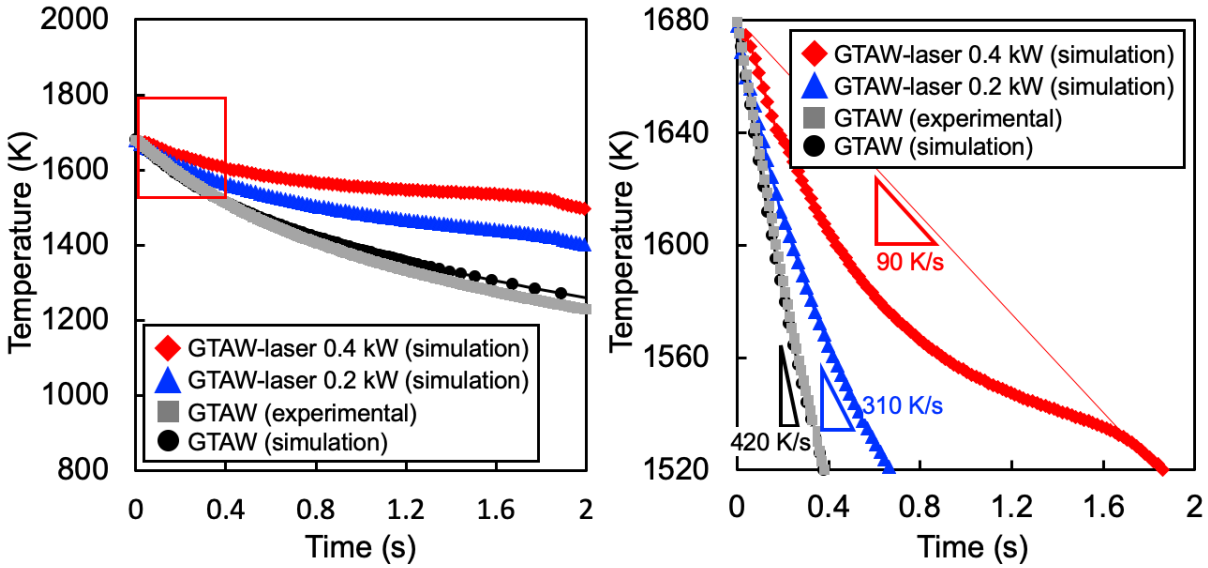
The finite element method for the U-type hot cracking test was designed by Quick welder software. Exploiting the resulting symmetry, half size of the U-type hot cracking test was established to decrease the calculation time of the finite element method (Fig. 3.4). The material constants used in this model is same as the Fig. 3.5.

### 4.4.2 Comparison of weld bead shape and temperature history between experiment and simulation

In order to confirm the validity of the finite element model during U-type hot cracking test of GTAW and GTAW-laser (laser power change), weld bead shape and temperature history were compared. Table 4.3 shows the bead morphology comparison between experimental and calculated results. The bead sizes from the simulation and experimental results were in good agreement, with an error of less than 10%. The strain curve comparison has been already confirmed in Fig. 3.8. The temperature history of the weld bead was measured by inserting a thermocouple into the weld pool during the GTAW (Fig. 4.8). Fig. 4.8(a), (b) indicate the cooling rate in a wide temperature range and a solid-liquid co-existence area, respectively. The experimental and simulation results were in good agreement both temperature history. Therefore, the finite element method verified the identical results with the experimental results with respect to the weld bead morphology and temperature history. Therefore, the GTAW-laser weld temperature history was replaced by the simulation result (Fig. 4.8).

Table 4.3 Weld bead geometries comparison between the experimental and simulation results.

| Welding process | Width of weld bead (mm) | | Depth of weld bead (mm) | |
|---|---|---|---|---|
| | Experiment | Simulation | Experiment | Simulation |
| GTAW | 5.14 | 5.11 | 0.99 | 1.04 |
| GTAW-laser 0.2 kW | 5.15 | 5.11 | 1.01 | 1.04 |
| GTAW-laser 0.4 kW | 5.18 | 5.11 | 1.10 | 1.04 |

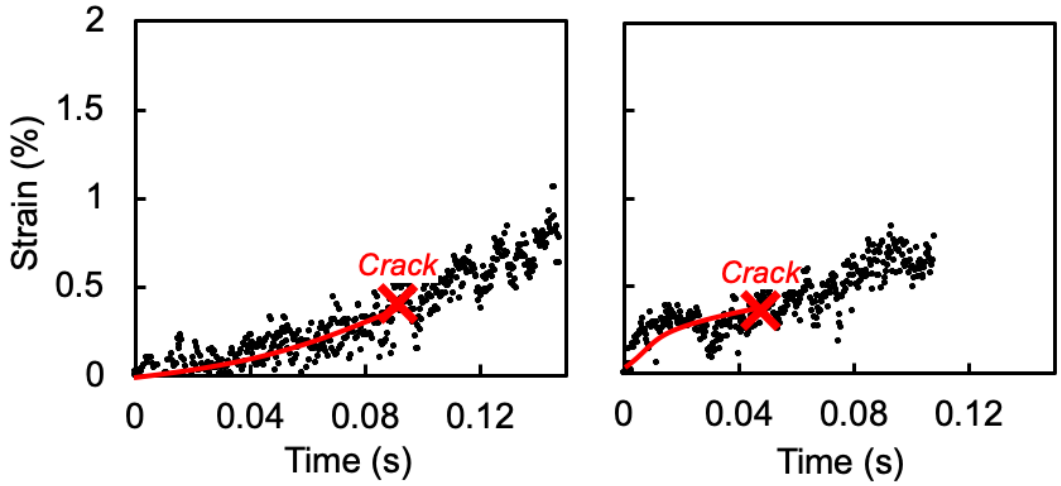



(a) Temperature range: 2000 – 800 K (b) Temperature range: 1680 – 1520 K

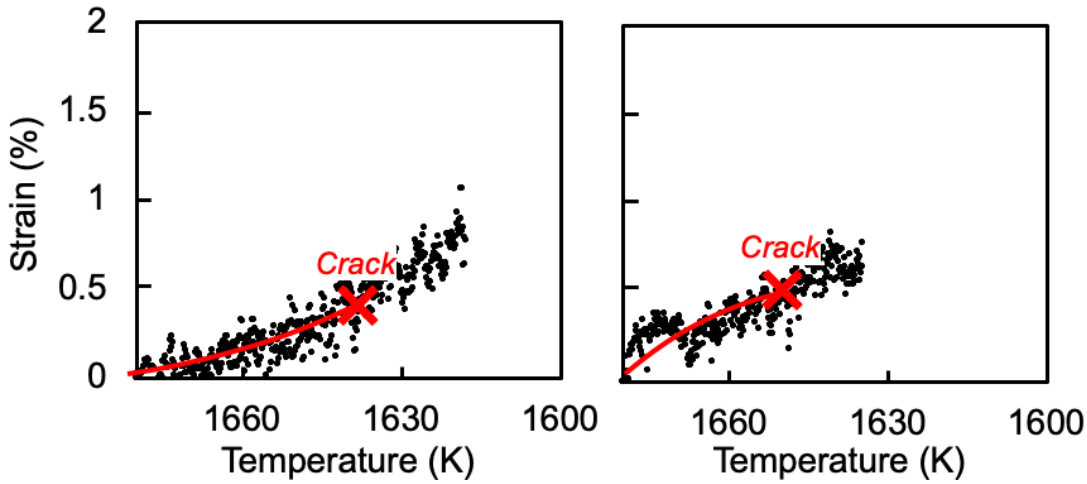
Fig. 4.8 Temperature history comparison.

### 4.5 Critical strain measurement in laser in-situ post heating

In the U-type hot cracking test of GTAW-laser welding, the in-situ observation method was used to measure the critical strain required for hot ductility curve. The in-situ observation method explained in Chapter 3.5. In this chapter, the effect of laser in-situ post heating on critical strain was observed via in-situ observation technique. The solidification cracking was generated by irradiating laser power of 0.2 kW and 0.4 kW under 13kN stress condition. In this test, the critical strain at which solidification cracking occurred was measured with a high-speed camera to compare the critical strain according to the cooling rate of the molten pool. The horizontal axis of the measured critical strain (Fig. 4.9) was converted from time to temperature using the cooling rate (Fig. 4.8). The solidification initiates at 0 s in Fig. 4.9(a), (b) at the temperature of 1680 K. The time axis is then modified to a temperature axis by calculating the temperature reduction amount according to the cooling rate (GTAW-laser 0.2 kW: 310 K/s and GTAW-laser 0.4 kW: 90K/s). Fig. 4.9(a') and (b) show the strain-temperature results in GTAW-laser 0.2 kW and GTAW-laser 0.4 kW, respectively. In Fig. 4.10, the critical strains according to the laser power change (Fig. 4.9) and in GTAW condition (Fig. 3.10) were compared. The critical strain showed a constant value regardless of the change in cooling rate of molten pool. Therefore, the critical strain of the hot ductility curve was used as the value measured under the GTAW condition (Fig. 3.10).




(a) GTAW-laser 0.2 kW (b) GTAW-laser 0.4 kW




(a) GTAW-laser 0.2 kW (b) GTAW-laser 0.4 kW

Fig. 4.9 Strain- time and strain-temperature curve according to laser power.

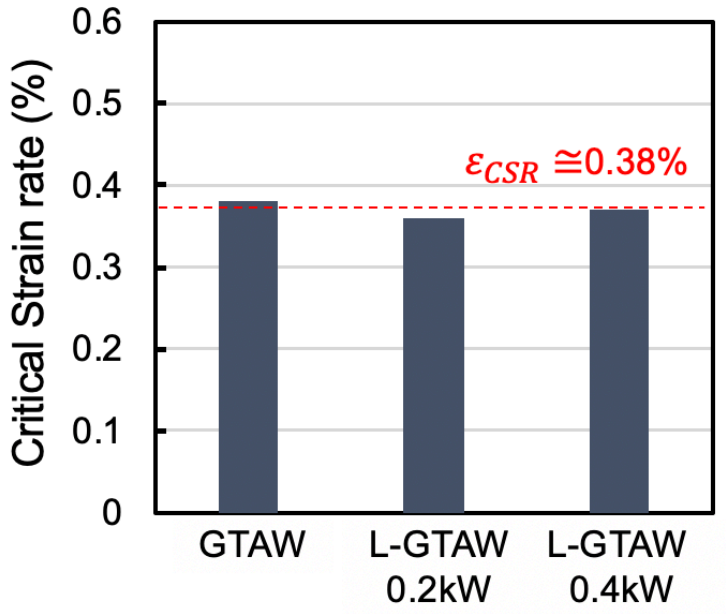



Fig. 4.10 Critical strain according to cooling rate of molten pool.

## 4.6 Theoretical approach to solidification cracking susceptibility in GTAW-laser welding

During the welding process, segregation of solute elements occurs along with dendrite growth because a solid phase exhausts solute elements into the remaining liquid phase. Consequently, the solute content of liquid is continuously increased during the solidification. Therefore, the true solidification temperature deviates from the normal solidus temperature. In this chapter, the BTR according to welding conditions was calculated by metallurgical analysis method explained in Chapter 3.6. Table 4.4 shows conditions for numerical calculations. Cooling rate according to welding conditions were calculated by finite element method.

Tables 4.5-4.7 show the solidification initiation temperature according to laser conditions results calculated by KGT model. As the laser power increased, the solidification initiation temperature increased. The temperature was constant according to heat source distance change. The difference in temperature did not appear when the laser spot size increased. By laser in-situ post heating, solidification initiation temperature was slightly increased when compared to GTAW condition. There was also no temperature difference among the laser adopted welding processes.

Table 4.4 Conditions for numerical calculations.

| | | | |
|---|---|---|---|
| Dendrite radius (μm) | | 10 | |
| Number of mesh division | | 100 | |
| Solidification rate (mm/s) | | 5 | |
| Laser power | GTAW | L-GTAW 0.2 kW | L-GTAW 0.4 kW |
| Cooling rate (K/s) | 420 | 310 | 90 |
| Distance between heat sources (mm) | 8 | 10 | 12 |
| Cooling rate (K/s) | 230 | 226 | 226 |
| Laser spot size (mm) | 8 | 10 | 12 |
| Cooling rate (K/s) | 250 | 226 | 190 |

Table 4.5 Solidification initiation temperatures according to laser power.

| Laser power | GTAW | L-GTAW 0.2 kW | L-GTAW 0.4 kW |
|---|---|---|---|
| Solidification initiation temperature (K) | 1680 | 1681 | 1685 |

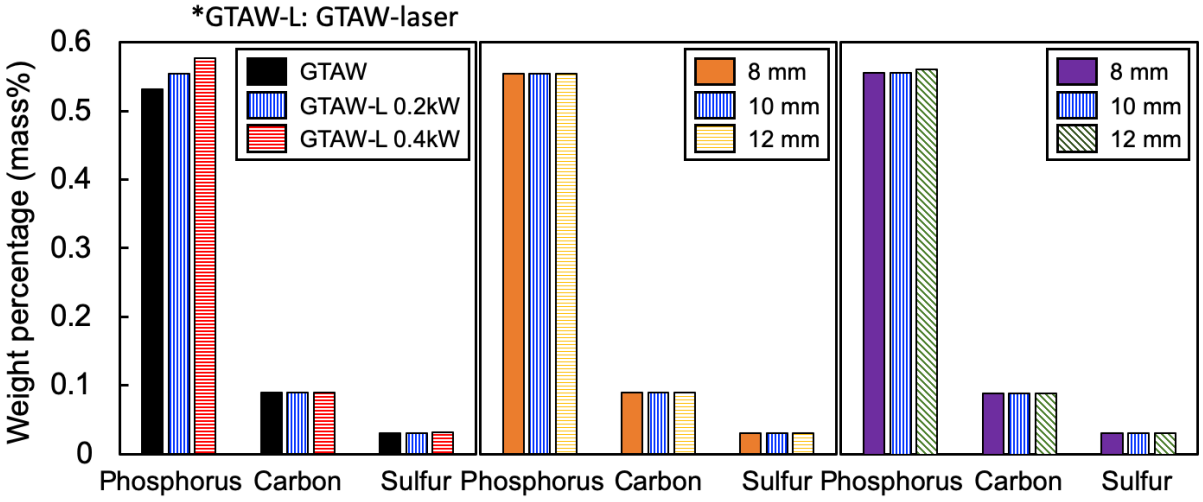
Table 4.6 Solidification initiation temperatures according to distance between heat sources.

| Distance change (mm) | 8 | 10 | 12 |
|---|---|---|---|
| Solidification initiation temperature (K) | 1681 | 1681 | 1681 |

Table 4.7 Solidification initiation temperatures according to laser spot size.

| Laser spot size (mm) | 8 | 10 | 12 |
|---|---|---|---|
| Solidification initiation temperature (K) | 1681 | 1681 | 1681 |

Fig. 4.11 shows the amount of segregation concentration in residual liquid during solidification using solidification segregation model. Fig. 4.11(a) shows a comparison of segregation amounts of low-melting-point elements P, C and S according to laser power. The decreased in cooling rate according to laser power (Table 4.4) was promoted the increased segregation. Fig. 4.11(b) compares the concentration according to distance change between laser and GTAW. Compared to GTAW, segregation concentration was increased with decreasing the cooling rate. However, significant change in cooling rate and segregation amount were not observed according to the change in the distance between the heat sources. The change in segregation amount according to laser spot size is shown in Fig. 4.11(c). As the laser spot size increased, the cooling rate was decreased (Table 4.4) and the segregation amount were slightly increased.




(a) Laser power (b) GTAW-laser distance (c) Laser spot size

Fig. 4.11 Solidification segregation concentration according to welding conditions.

Tables 4.8-4.10 show the solidification completion temperature. The Thermo-Calc software was employed for the conversion of the segregation concentration to the temperature. An increase in low-melting point elements by laser process reduced the solidification completion temperature compare with the GTAW.

Table 4.8 Solidification completion temperatures according to laser power.

| Laser power | GTAW | L-GTAW 0.2 kW | L-GTAW 0.4 kW |
|---|---|---|---|
| Solidification completion temperature (K) | 1520 | 1517 | 1515 |

Table 4.9 Solidification completion temperatures according to distance between heat sources.

| Distance between heat sources (mm) | 8 | 10 | 12 |
|---|---|---|---|
| Solidification completion temperature (K) | 1517 | 1517 | 1515 |

Table 4.10 Solidification completion temperatures according to laser spot size.

| Laser spot size (mm) | 8 | 10 | 12 |
|---|---|---|---|
| Solidification completion temperature (K) | 1517 | 1517 | 1516 |

### 4.7 Evaluation of solidification cracking susceptibility in GTAW-laser welding

Tables 4.11-4.13 show the BTR according to welding conditions. A hot ductility curve was obtained based on a combination of the BTR and critical strain. The critical strain was employed from the results of GTAW (Fig. 4.12).

The BTR was increased with increasing laser power (160-170 K). The significant change in BTR was not observed with the change in distance between the heat sources. Increased laser spot size enlarged BTR (164 K). Fig. 4.12 shows the hot ductility curve according to welding conditions (BTR: 160-166 K).

Campbell [29] emphasized the importance of thermos-mechanical aspects and simply consider the alloy's solidification temperature range viz., the larger solid-liquid co-existence range, the more susceptible to solidification cracking. However, there was no significant change in the solidification cracking susceptibility for all welding conditions. This implies that the change in the hot ductility curve does not significantly cause an increase in solidification cracking behavior.

Table 4.11 Calculated BTR results according to laser power.

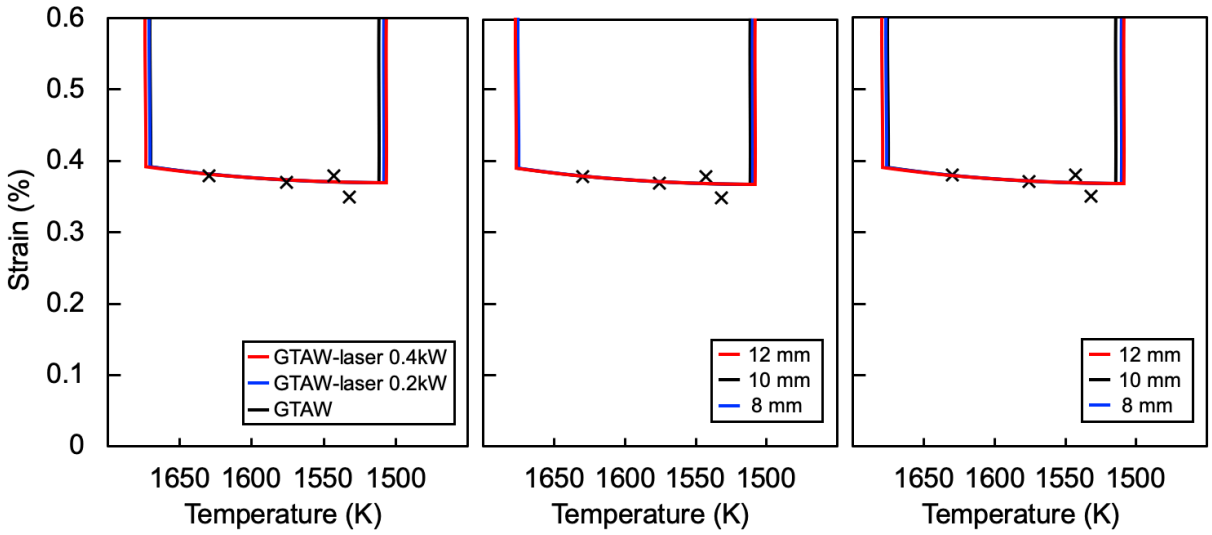
| Laser power | GTAW | L-GTAW 0.2 kW | L-GTAW 0.4 kW |
|---|---|---|---|
| BTR (K) | 160 | 164 | 170 |

Table 4.12 Calculated BTR results according to distance between heat sources.

| Distance change (mm) | 8 | 10 | 12 |
|---|---|---|---|
| BTR (K) | 164 | 164 | 166 |

Table 4.13 Calculated BTR results according to laser spot size.

| Laser spot size (mm) | 8 | 10 | 12 |
|---|---|---|---|
| BTR (K) | 164 | 164 | 164 |



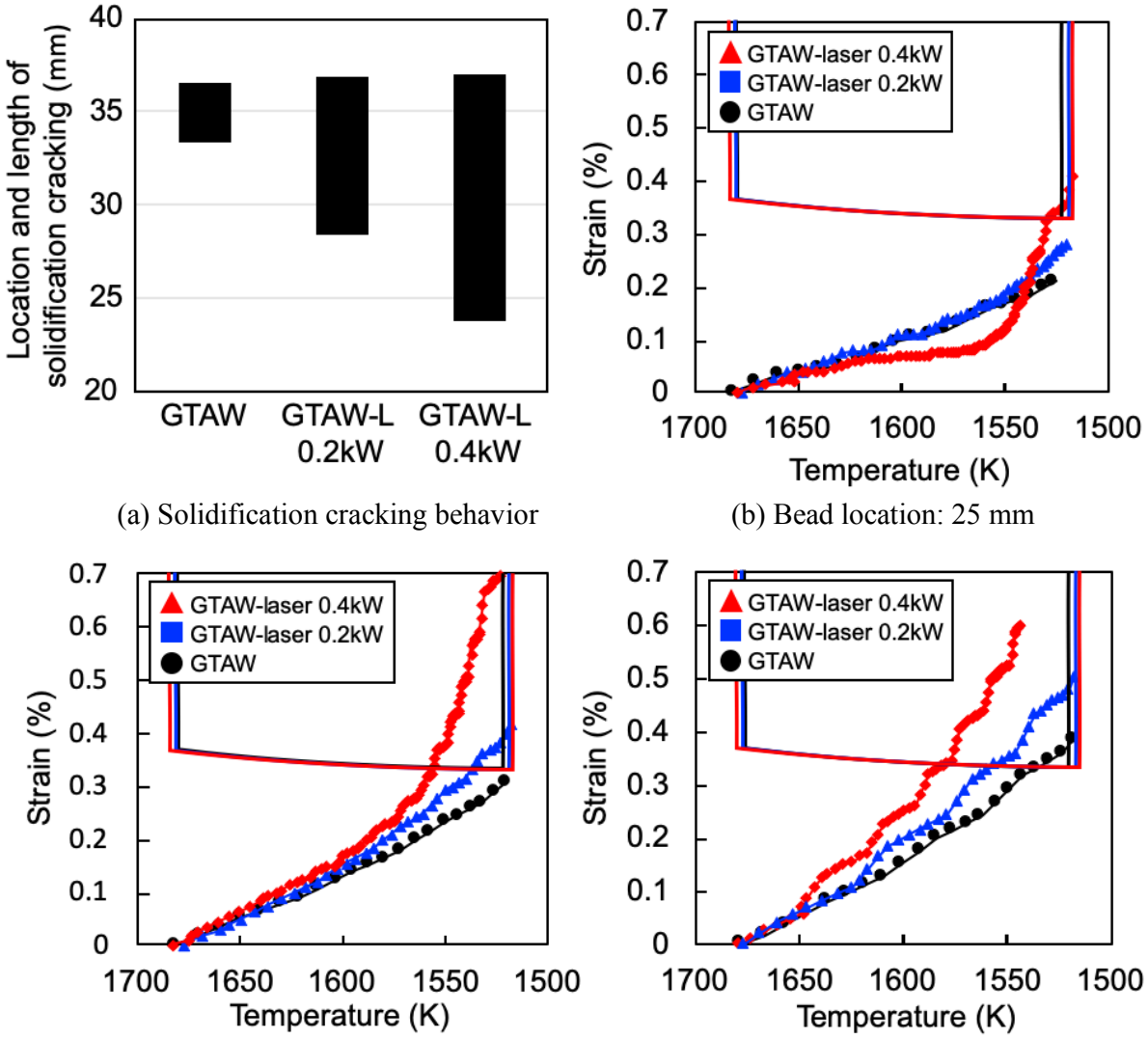

(a) Laser power (b) GTAW-laser distance (c) Laser spot size

Fig. 4.12 Hot ductility curves according to welding conditions.

## 4.8 Influence of laser in-situ post heating on solidification cracking behavior

### 4.8.1 Effect of laser power on solidification cracking behavior

Fig. 4.13(a) shows experimental solidification cracking behavior according laser power. As the laser power increased, the length of solidification cracking increased. The occurrence of solidification cracking may be expressed through the intersection of the hot ductility and the thermal strain. To show the change in crack length between welding conditions (Fig. 4.13 (a)), thermal strain for each bead location (25-35 mm), were calculated under the loaded stress of 13 kN (Fig. 4.13 (b-d)). In the GTAW-laser 0.4 kW, the largest heat input condition, the thermal strain intersected with the hot ductility curve at all bead locations (Fig. 4.13 (b-d)), resulting in largest solidification crack. The strain curve slope was decreased with lowering heat inputs and the solidification cracking length was shortened due to a decrease in the intersection with the hot ductility curve. Therefore, the change of thermal strain according to laser power change had a great influence on the solidification cracking behavior.




(a) Solidification cracking behavior

(b) Bead location: 25 mm

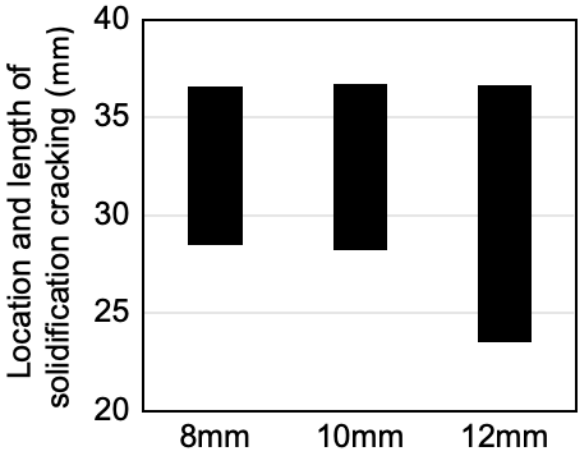
(c) Bead location: 30 mm

(d) Bead location: 35 mm

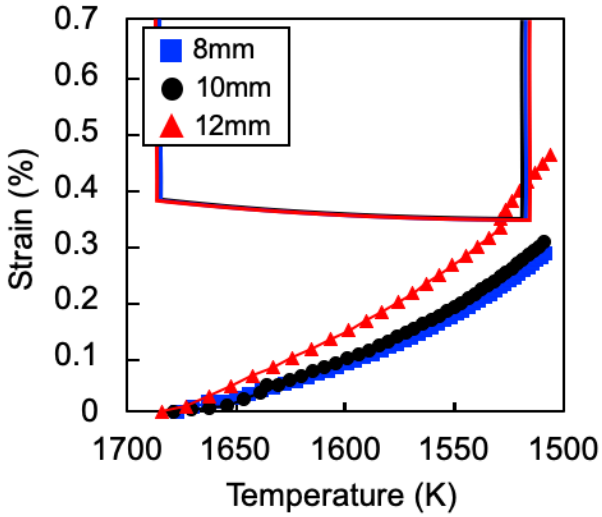
Fig. 4.13 Evaluation of solidification cracking behavior according to laser power change. Hot ductility curve and thermal strain comparison.

### 4.8.2 Effect of heat source distance on solidification cracking behavior

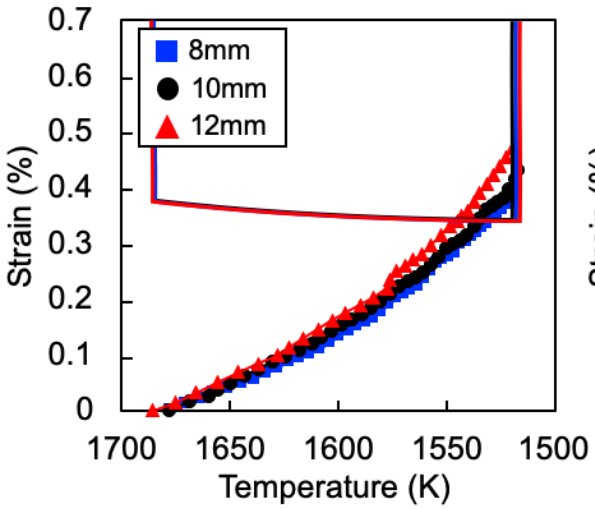
Fig. 4.14(a) shows experimental solidification cracking behavior according to distance between heat source. As the distance between heat sources increased, the length of solidification cracking increased. In order to show the change in crack length between welding conditions (Fig. 4.14(a)), thermal strain for each bead location (25~35 mm), were calculated under the loaded stress of 13 kN (Fig. 4.14(b-d)). In the distance condition of 8 mm the thermal strain intersected with the hot ductility curve in the bead locations of 25 mm and 35 mm (Fig. 4.14(c), (d)). The strain curve slope constants in the condition of 10 mm. In the distance condition of 15 mm, the largest distance condition, the thermal strain intersected with the hot ductility curve at all bead locations (Fig. 4.14(b-d)), resulting in the largest solidification crack. The strain curve slope was increased with increasing distance, and the solidification cracking length was elongated due to an increase in the intersection with the hot ductility curve.



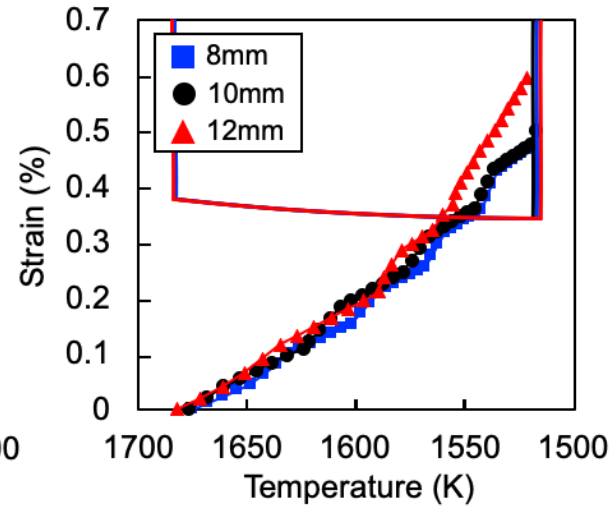

(a) Solidification cracking behavior




(b) Bead location: 25 mm




(c) Bead location: 30 mm

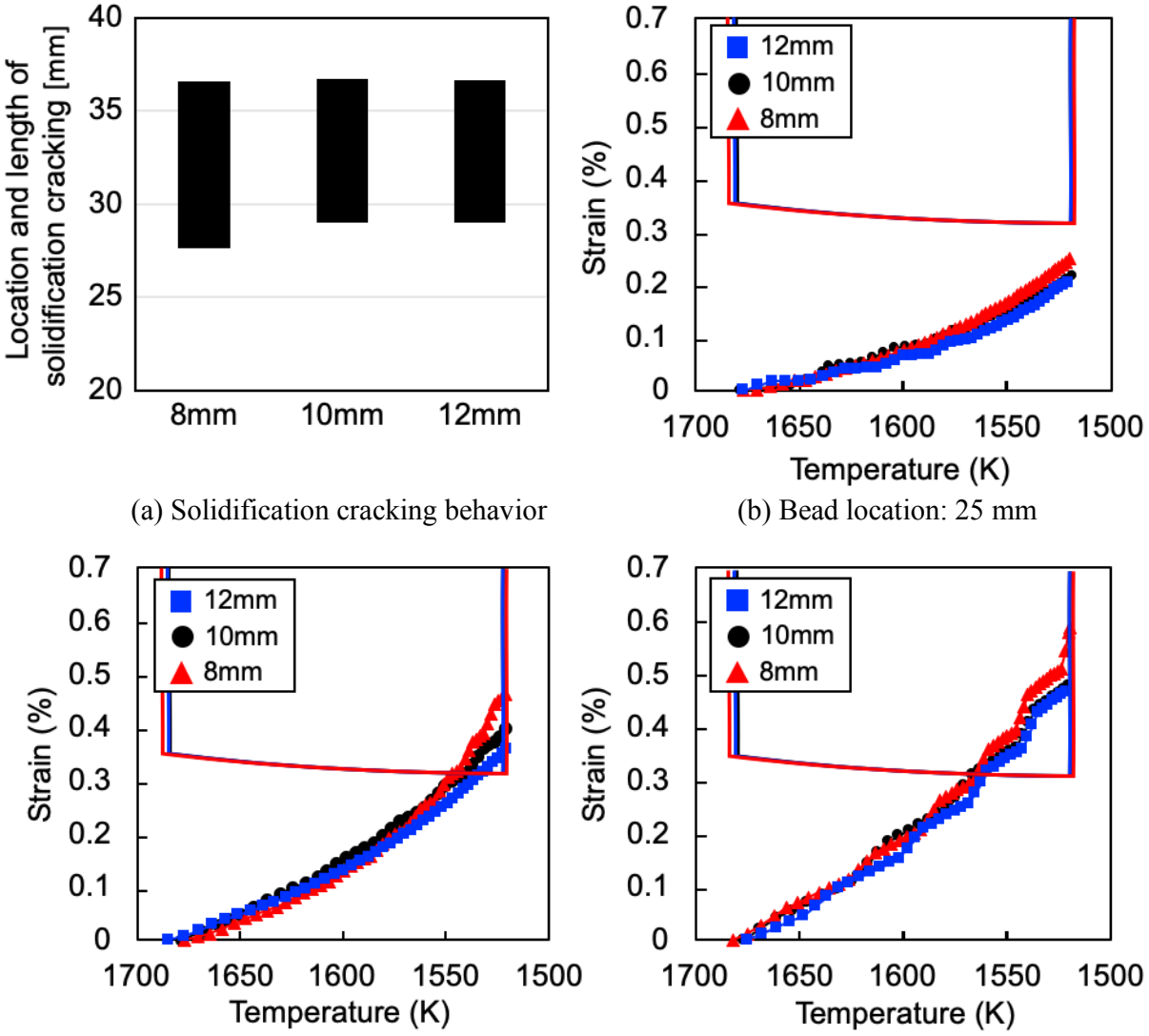



(d) Bead location: 35 mm

Fig. 4.14 Evaluation of solidification cracking behavior according to distance between heat sources change. Hot ductility curve and thermal strain comparison.

### 4.8.3 Effect of laser spot size on solidification cracking behavior

Fig. 4.15(a) shows experimental solidification cracking behavior according to laser spot size change. As the laser spot size decreased, the length of solidification cracking was slightly increased. In order to show the change in crack length according to welding conditions (Fig. 4.15(a)), thermal strain for each bead location (25-35 mm), were calculated under the loaded stress of 13 kN (Fig. 4.15 (b-d)). In the condition of laser spot size 8 mm, the smallest beam size condition, the thermal strain intersected with the hot ductility curve at bead locations of 30-35 mm, resulting in the largest solidification crack. In the size of 10 mm, the thermal strain intersected in the bead locations of 30 mm and 35 mm (Fig. 4.15 (c), (d)). In the size of 12 mm, the thermal strain also intersected in the bead locations of 30 mm and 35 mm (Fig. 4.15 (c), (d)). As the laser spot size decreased, the thermal strain was slightly increased. However, there was no significant change in both the solidification cracking occurrence and thermal strain behavior.




(a) Solidification cracking behavior

(b) Bead location: 25 mm

(c) Bead location: 30 mm

(d) Bead location: 35 mm

Fig. 4.15 Evaluation of solidification cracking behavior according to laser spot size change. Hot ductility curve and thermal strain comparison.

### 4.9 Controlling of thermal strain behavior in laser in-situ post heating

Fig. 4.13-4.15 show the thermal strain with temperature drop during solidification temperature range, which is considered as the mechanical driving force of solidification cracking. It can be seen that the strain was increased by the laser in-situ post heating comparing with the GTAW. As welding progressed, the slope of the thermal strain was also increased due to an increase in the amount of deformation of the weld. The slope of thermal strain was increased by accumulated heat input of the specimen during the welding. In addition, as the laser power increased, in the bead location of 25 mm the thermal strain began to cross the hot ductility curve when the laser power exceeds 0.4 kW, which means that solidification cracking is much possible to occur due to the high thermal strain rate. Therefore, an increase in the heat input increased the thermal strain. However, there was no significant difference in thermal strain behavior according to the distance between heat sources and the laser spot size. The effect of each laser in-situ post heating condition on the thermal strain behavior was considered from the thermomechanical point of view using the final element method.

### 4.9.1 Controlled by laser power

Fig. 4.16 shows the temperature distribution calculated using finite element simulation method. The solid-liquid co-existence area was calculated using the temperature history employed by the finite element method. Solid-liquid co-existence zone lengths of 2.3 mm in GTAW condition, 3.2 mm in GTAW-laser 0.2 kW and 8.8 mm in GTAW-laser 0.4 kW were observed (Table 4.14). The increase in laser power lowered the cooling rate of the molten pool and increased the solid-liquid co-existence zone. Therefore, an increase in the laser power increased temperature distribution of the weld. The length of the solid-liquid co-existence zone increased due to an increase in heat input according to the laser power.

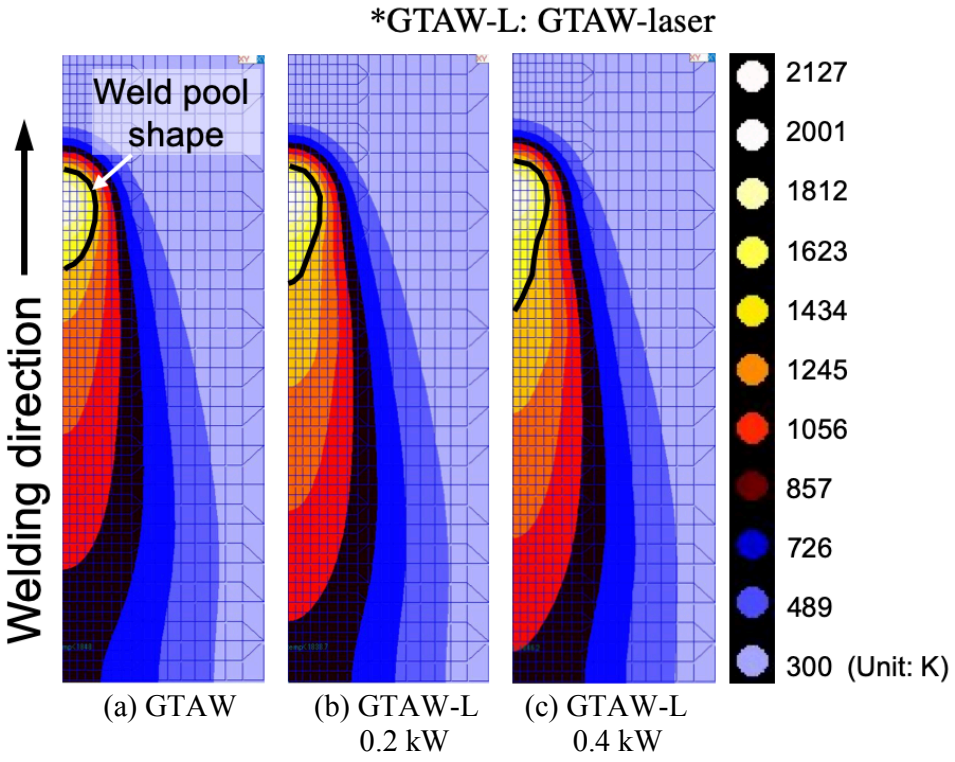


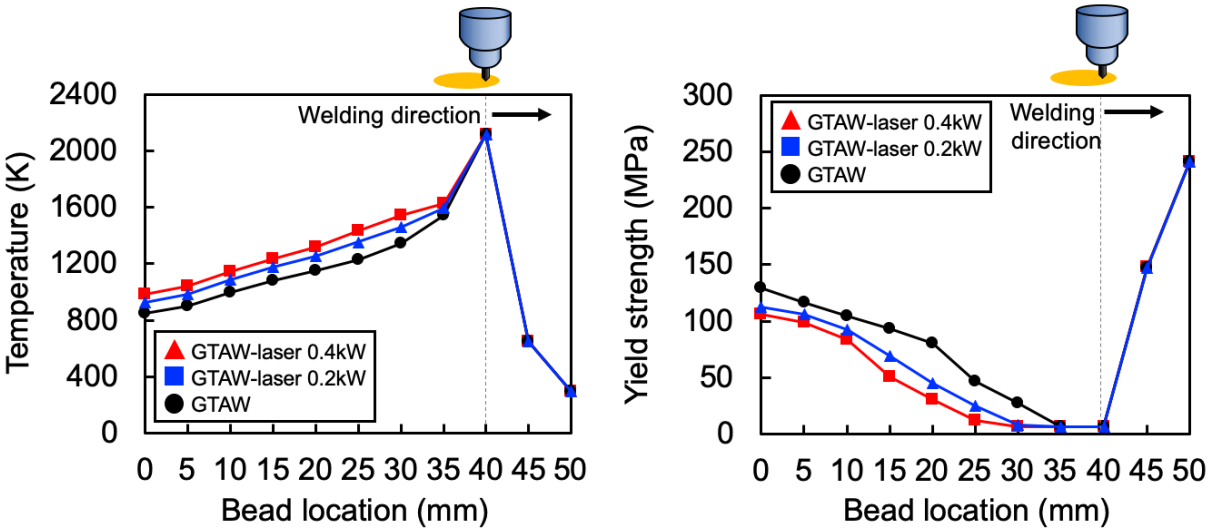

Fig. 4.16 Temperature field calculated by finite element method.

Table 4.14 Length of solid-liquid co-existence zone.

| | Laser power change condition | | |
|---|---|---|---|
| | GTAW | GTAW-laser 0.2 kW | GTAW-laser 0.4 kW |
| Solid-liquid co-existence zone (mm) | 2.3 | 3.2 | 8.8 |

The effect of the increase in the solid-liquid coexistence area with the laser power on the behavior of the thermal strain was investigted. Fig. 4.17 shows the temperature distribution calculated using finite element simulation method. Solid-liquid co-existence zone lengths of 2.3 mm in GTAW condition, 3.2 mm in GTAW-laser 0.2 kW and 8.8 mm in GTAW-laser 0.4 kW were changed. Fig. 4.17 (a) shows the temperature distribution calculated by the finite element simulation method according to the bead location when the heat source passes through an arbitrary location (40 mm). Although the same maximum temperature was obtained at 40 mm, the high temperature

distribution appeared in the GTAW-laser welding condition because of the increased solid-liquid co-existence zone. Under the same welding timing condition, the yield strength distribution was calculated according to the bead location (Fig. 4.17 (b)). For the SUS310S steel, the yield strength decreased in accordance with an increase in temperature (Fig. 3.5). The yield strength was decreased with an increase in temperature. The GTAW-laser welding condition with higher temperature distribution than the GTAW, had low yield strength distribution on the weld bead. The low yield strength distribution was vulnerable to plastic deformation resulting in solidification cracking propagation. Therefore, the decrease in yield strength distribution with increasing laser power enhanced the slope of the thermal strain, resulting in the increased solidification cracking susceptibility.




(a) Temperature distribution (b) Yield strength distribution

Fig. 4.17 Temperature and yield strength distribution calculated by finite element method.

Fig. 4.18 presents the stresses applied to the weld bead during solidification calculated by the finite element simulation method. The stress on the welds increased due to an increase in the solid-liquid co-existence zone. The stress concentration in the solid-liquid co-existence zone was reported as one of the solidification cracking occurrence criterions [120-122]. Due to an increase in the solid-liquid co-existence zone, a greater stress was applied to the weld. As a result, an increase in the solid-liquid co-existence zone became vulnerable to solidification cracking due to an increase in the slope of the thermal strain curve by the yield strength reduction and the increased loaded stress.

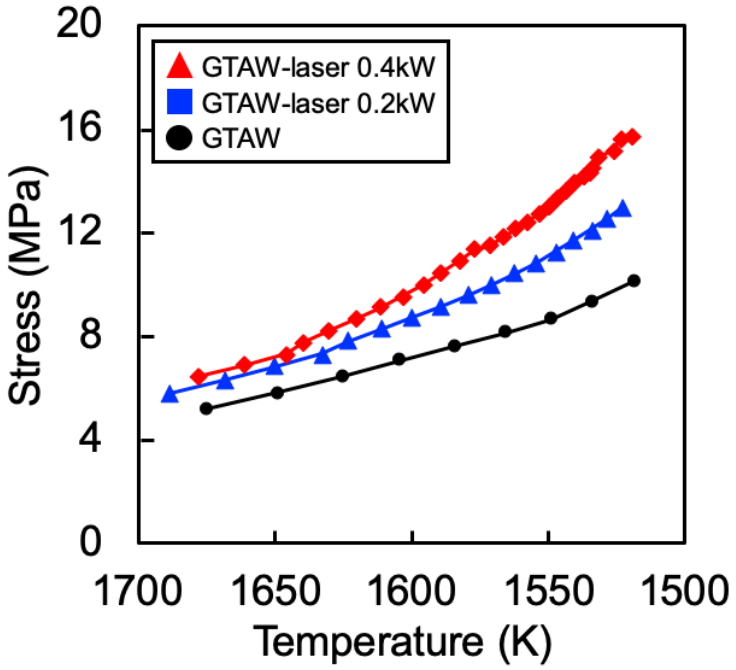


Fig. 4.18 Stress loaded on the weld bead during solidification.

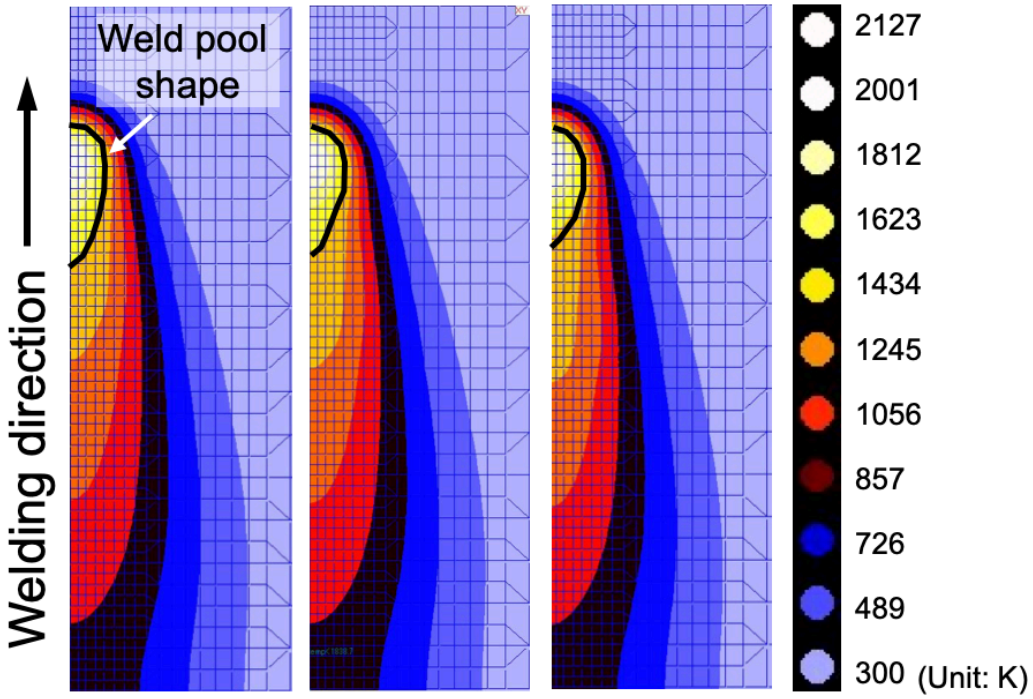
### 4.9.2 Controlled by heat source distance

Fig. 4.19 shows the temperature distribution according to distance change between heat sources calculated using finite element simulation method. The solid-liquid co-existence area was calculated using the temperature history employed by the finite element method. Solid-liquid co-existence zone lengths of 3.0 mm in 8 mm condition, 3.3 mm in 10 mm condition and 3.7 mm in 12 mm condition were investigated (Table 4.15). An increase in distance between heat sources slightly lowered the cooling rate of the molten pool and increased the solid-liquid co-existence zone. Therefore, an increase in the distance between heat sources increased temperature distribution of the weld. The length of the solid-liquid co-existence zone was increased due to an increase in distance.

The effect of an increase in the solid-liquid coexistence area with the laser power on the behavior of the thermal strain was investigated. Fig. 4.20 shows the temperature distribution calculated using finite element simulation method. Solid-liquid co-existence zone lengths of 3.0 mm in 8 mm condition, 10 mm in 10 mm conditions and 12 mm in 12 mm condition were changed. Fig. 4.19(a) shows the temperature distribution calculated by the finite element simulation method according to the bead location when the heat source passes through an arbitrary location (40 mm). Although the same maximum temperature was obtained at 40 mm, the high temperature distribution was appeared in the 12mm condition because of an increase in solid-liquid co-existence zone. Under the same welding timing condition, the yield strength distribution was calculated according to the bead location (Fig. 4.20(b)). For the SUS310S steel, the yield strength decreased in accordance with an increase in temperature (Fig. 3.5). The distance between heat sources with higher temperature distribution than the GTAW, had low yield strength distribution on the weld bead. The low yield strength distribution was vulnerable to plastic deformation resulting in solidification cracking propagation. Therefore, the decrease in yield strength distribution with increasing distance between

heat sources enlarged the slope of the thermal strain, resulting in the increased solidification cracking susceptibility.

Fig 4.21 shows the stress loaded on weld bead during the solidification according to distance between heat sources. Due to the increase in the distance between heat sources, a longer solid-liquid co-existence zone was formed during the welding. The stress on the weld bead was increased due to the solid-liquid co-existence zone resulting in vulnerable to solidification cracking due to an increase in the slope of the thermal strain curve by the yield strength reduction and the increased loaded stress.

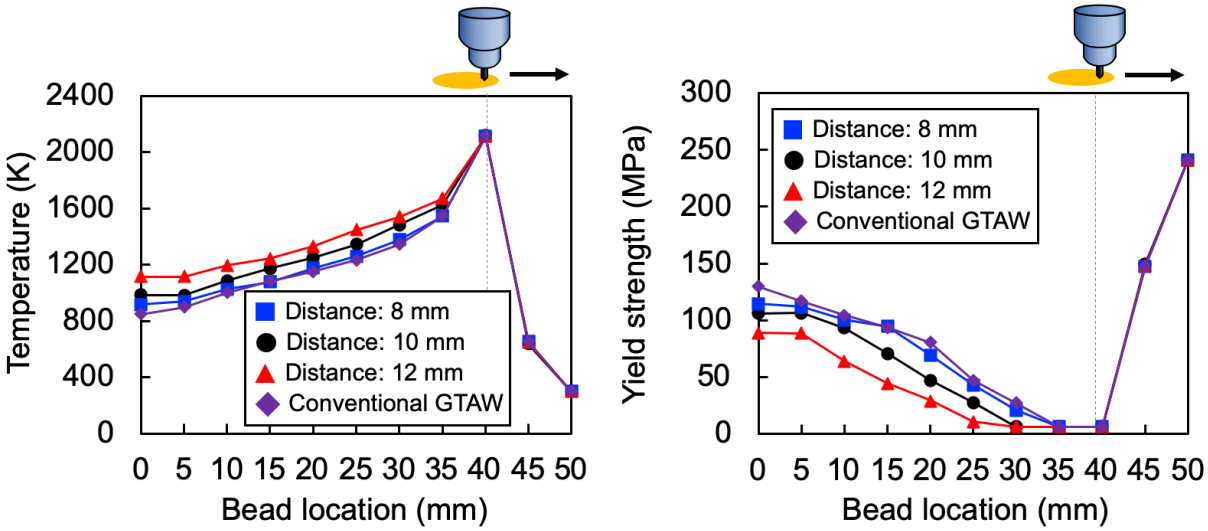



(a) 8 mm (b) 10 mm (c) 12 mm

Fig. 4.19 Temperature field with distance change between heat sources calculated by finite element method.

Table 4.15 Length of solid-liquid co-existence zone.

| | Distance between heat sources | | |
|---|---|---|---|
| | 8 mm | 10 mm | 12 mm |
| Solid-liquid co-existence zone (mm) | 3.0 | 3.3 | 3.7 |




(a) Temperature distribution (b) Yield strength distribution

Fig. 4.20 Temperature and yield strength distribution calculated by finite element method.

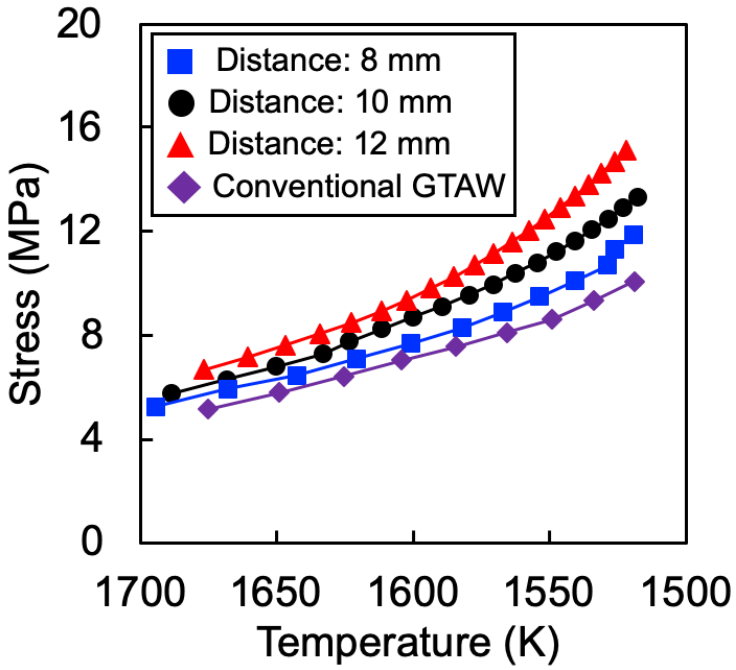
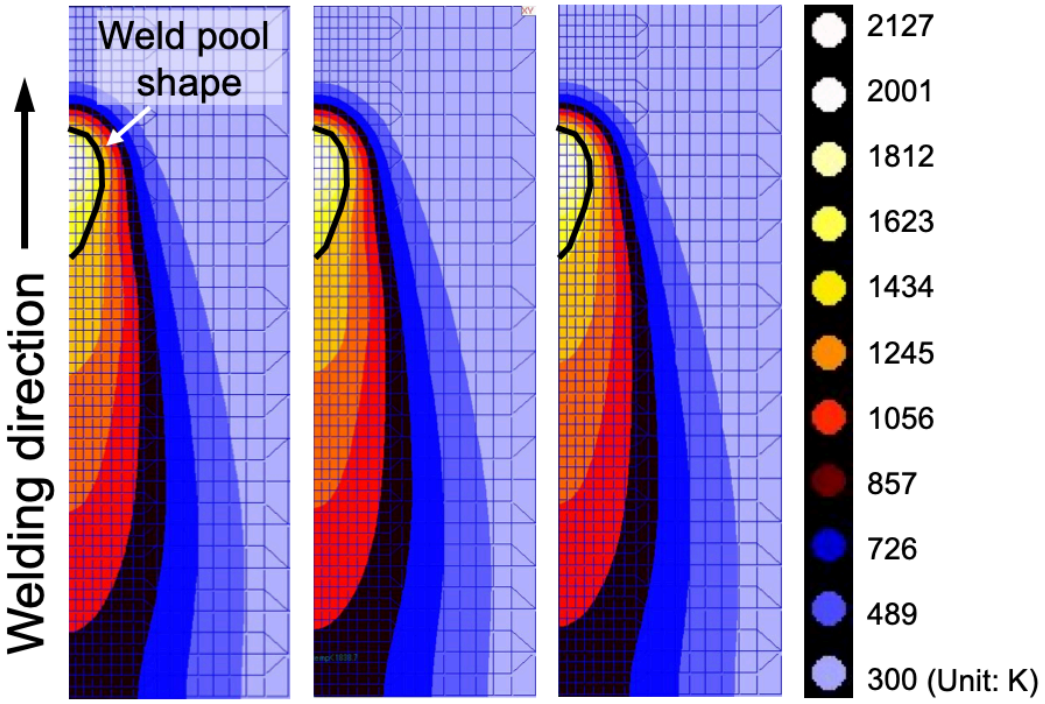



Fig. 4.21 Stress loaded on the weld bead during solidification.

### 4.9.3 Controlled by laser spot size

Fig. 4.22 shows the temperature distribution according to laser spot size change calculated using finite element simulation method. The solid-liquid co-existence area was calculated using the temperature history employed by the finite element method. Solid-liquid co-existence zone lengths of 3.4 mm in 8 mm beam size, 3.3 mm in 10 mm beam size and 3.2 mm in 12 mm beam size were investigated (Table 4.16). An decrease in laser spot size slightly lowered the cooling rate of the molten pool and increased the solid-liquid co-existence zone. As the size of the laser beam

decreased, the amount of heat input was increased due to an increase in the density. Therefore, the decrease in the laser spot size enlarged temperature distribution of the weld. The length of the solid-liquid co-existence zone was elongated due to a decrease in laser spot size.




(a) 8 mm (b) 10 mm (c) 12 mm

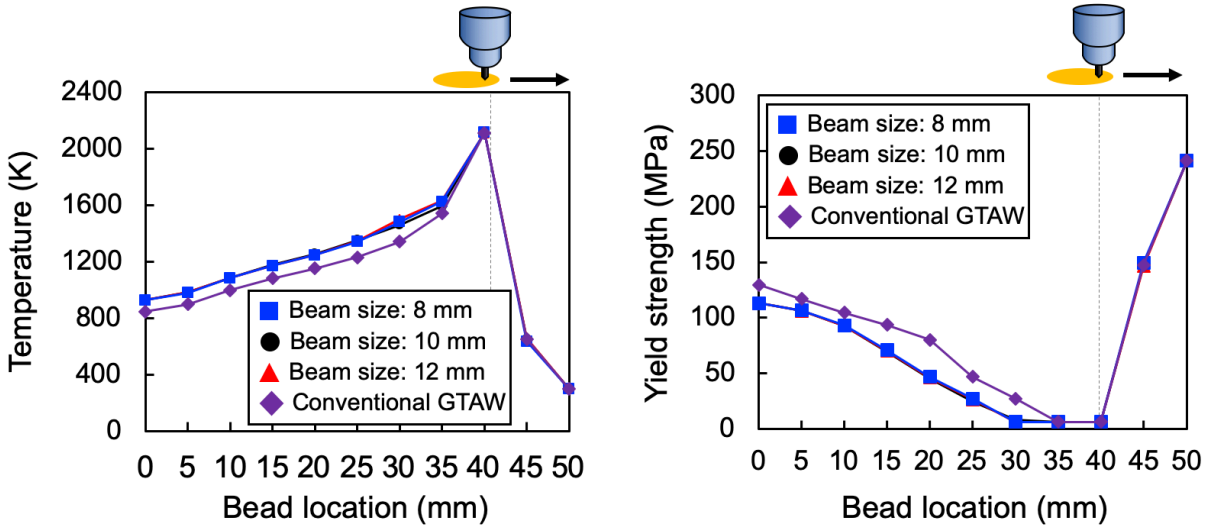
Fig. 4.22 Temperature field with laser spot size change between heat sources calculated by finite element method.

Table 4.16 Length of solid-liquid co-existence zone.

| | Laser spot size | | |
|---|---|---|---|
| | 8 mm | 10 mm | 12 mm |
| Solid-liquid co-existence zone (mm) | 3.4 | 3.3 | 3.2 |

The effect of an increase in the solid-liquid coexistence area with the laser spot size change on the thermal strain behavior was investigated. Fig. 4.23 shows the temperature distribution calculated using finite element simulation method. Solid-liquid co-existence zone was decreased with a decrease in laser spot size. Fig. 4.23(a) shows the temperature distribution calculated by the finite element simulation method according to the bead location when the heat source passes through an arbitrary location (40 mm). Laser in-situ post heating process showed higher temperature distribution than GTAW. However, although the laser spot size was changed, the temperature distribution of weld bead was not significantly changed. Under the same welding timing condition, the yield strength distribution was calculated according to the bead location (Fig. 4.23(b)). For the SUS310S steel, the yield strength decreased in accordance with an increase in temperature (Fig. 3.5). With the laser in-situ post heating process, the yield strength of the weld bead was reduced compared to the GTAW. However, the yield strength according to the change in the laser spot size

was constant. The low yield strength distribution in laser spot size change condition was vulnerable to plastic deformation resulting in solidification cracking propagation. The change in the laser spot size did not have a significant effect on the high temperature cracking behavior because it did not significantly affect the temperature and yield strength distribution of the weld bead.




(a) Temperature distribution (b) Yield strength distribution

Fig. 4.23 Temperature and yield strength distribution calculated by finite element method.

Fig 4.24 shows the stress loaded on weld bead during the solidification according to laser spot size. There was no difference in solid-liquid co-existence zone according to laser spot size change. Although laser in-situ post heating loaded more stress than GTAW, the stress on the weld was constant according to the size of the laser beam has been shown. As a result, laser spot size change did not affect significant solidification cracking behavior.

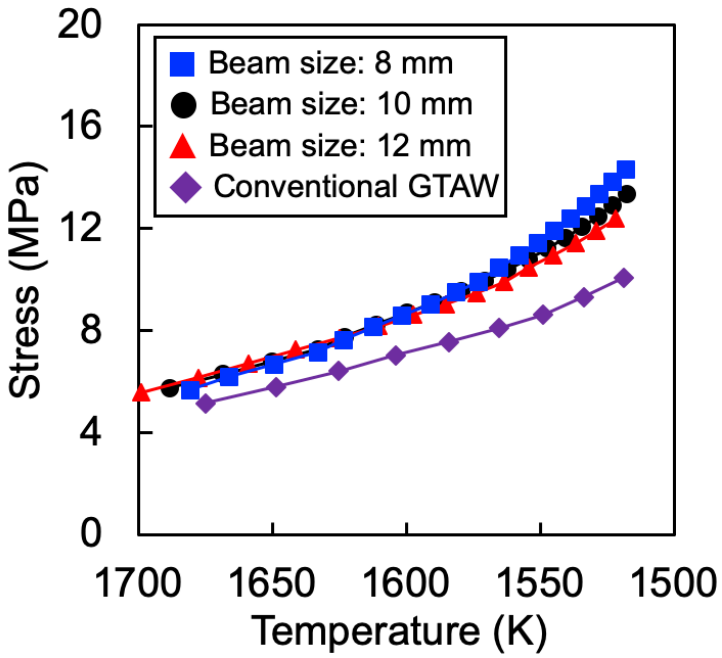



Fig. 4.24 Stress loaded on the weld bead during solidification.

## 4.10 Summary

In this chapter, the laser beam was irradiated behind the molten pool to observe the solidification cracking behavior during the U-type hot cracking test of GTAW. Irradiation of the laser beam of the molten pool increased the solidification cracking than the GTAW. The effect of the change in the solid-liquid coexistence zone of the molten pool on the solidification cracking by changing the laser power, the distance between the heat sources, and the laser spot size was analyzed using the solidification cracking prediction model. The hot ductility curve according to each welding condition was calculated and compared with the thermal strain calculated by the finite element method to compare the solidification cracking behavior.

The summarized conclusions are as follows;

1) The critical strain according to the laser power change was compared using the in-situ observation method. The cooling rate was changed according to the laser power, but the critical strain was constant. Therefore, the critical strain of the hot ductility curve was used as the result of GTAW.

2) Solidification initiation and completion temperature according to welding conditions were calculated through metallurgical analysis. Cooling rate decreased with increasing laser beam power. A decrease in cooling rate increased the solidification initiation temperature. The solidification completion temperature decreased due to an increase in the amount of segregation concentration of the residual liquid. Therefore, the BTR increased with increasing laser power. As the distance change between heat sources increased, the cooling rate decreased and BTR increased. The BTR was constant because there was no change in the cooling rate under the laser spot size change condition. The BTR increased slightly by the laser in-situ post heating process. However, solidification cracking susceptibility did not changed significantly enough to affect the solidification cracking behavior.

3) The slope of thermal strain increased with an increase in the laser power and the solidification cracking increased with an increase in the intersections with the hot ductility curve. As the distance between the heat sources increased, the thermal strain increased, and the solidification cracking increased. The change in the size of the laser beam has no significant effect on the slope of the thermal strain.

4) Increasing the laser power and the distance between heat sources increased the solid-liquid coexistence zone and increased the temperature distribution of the weld beads. Also increased the stress loaded on the weld bead during the solidification. Therefore, a decrease in distribution of yield strength and loaded stress increase on the welded bead, making it vulnerable to plastic deformation, and the solidification cracking increase. Since there was no change in the solid-liquid coexistence area under the laser spot size change, the temperature distribution and yield strength distribution were constant, showing similar solidification cracking behavior.

# Chapter 5 Prevention of solidification cracking by temperature history control via cooling process

## 5.1 Introduction

It is common knowledge that type 310S stainless steel is potentially susceptible to solidification cracking, which is dependent on the $Cr_{eq}/Ni_{eq}$ ratio and P + S content of the steel [1, 12, 17, 83-84]. In particular, the segregation of low melting elements (P and S) during welding has an influence on the susceptibility of solidification cracking [25, 88-90].

Metallurgical prevention methods were proposed to prevent solidification cracking; however, these resulted in secondary problems. Gooch et al. [55] increased the manganese content for combination with excess sulfur. Moreover, Arata et al. [82] increased the carbon content to inhibit the micro-fissures due to an increase in the amount of inter-dendritic eutectic available to backfill the cracks formed at high temperatures. However, these methods resulted in a decrease in the corrosion resistance.

A thermomechanical method was proposed to prevent solidification cracking without secondary problems. Plockikhine [114] exposed a specimen to additional laser irradiation, to prevent solidification cracking during welding (multi-beam technology). Gobel [115] also applied inductive heat around the weld bead, thus preventing solidification cracking. The heat-induced expansion of the specimen decreased the weld bead strain and suppressed solidification cracking without secondary problems. However, these welding processes were complex, and further clarification of the effect of the additional heat input on the specimen is required.

The effect of increasing heat input of weld bead on solidification cracking behavior was investigated by using in-situ laser post heating in Chapter 4. It is necessary to reduce the amount of heat input to suppress the solidification cracking. In this study, a water cooling process was carried out on the back side of the weld bead during gas tungsten arc welding (GTAW) to prevent solidification cracking. A finite element analysis method was employed to analyze the effects of the water cooling process on the occurrence of cracks at high temperatures and the changes in strain of the weld bead.

## 5.2 Materials and experimental procedures

### 5.2.1 Material

A type 310S stainless steel with solidification mode A was used. The size of specimen is 100×50×2 mm. The chemical composition of the steel is shown in Table 3.1. For the removal of the surface metal oxides and other tarnishes, the specimen was cleaned by ethanol prior to welding.

### 5.2.2 U-type hot cracking test with water-cooled GTAW

An water cooling process was conducted to control the solid-liquid co-existence zone of the weld bead during the U-type hot cracking test (Fig. 5.1). A water cooling process was carried out on the back side of the weld bead during gas tungsten arc welding (GTAW) to prevent solidification cracking. In this study, U-type hot cracking test was conducted under the stress condition of 13 kN.

The specific conditions of the water-cooled GTAW and the U-type hot cracking test are shown in Tables 5.1 and 5.2.

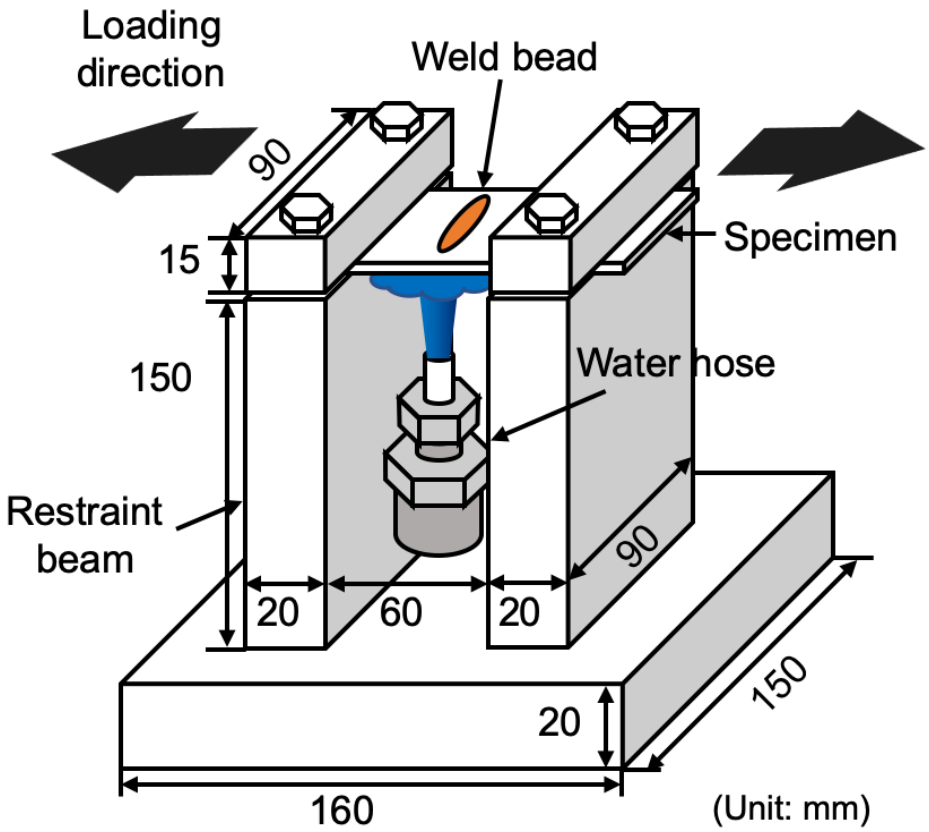



Fig. 5.1 Schematic diagram of the water-cooled GTAW during the U-Type hot cracking test.

Table 5.1 Water-cooled GTAW conditions in U-type hot cracking test.

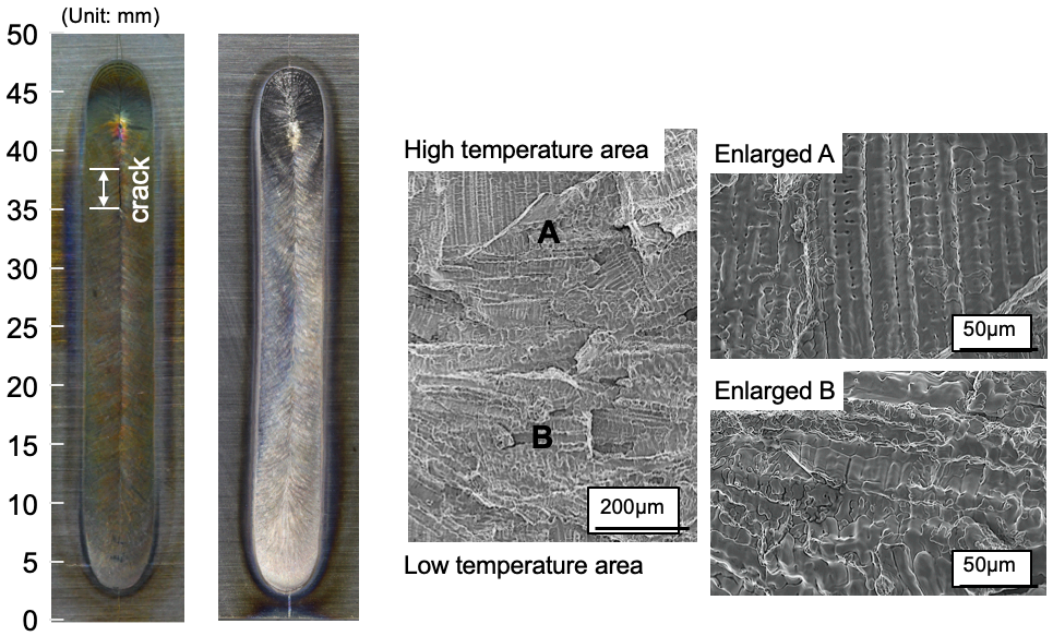
| Parameters | Values |
|---|---|
| Welding speed (mm/s) | 5 |
| Loading stress (kN) | 13 |
| Welding current (A) | 110 |
| Welding current in water-cooled(A) | 115 |
| Arc length (mm) | 1 |
| Electrode radius (mm) | 2.4 |
| Electrode extension (mm) | 15 |
| Electrode angle (°) | 50 |
| Shielding gas | Ar |
| Gas flow rate (l/min) | 20 |
| Water flow rate (ml/s) | 10 |
| Water temperature (℃) | 23 |

### 5.2.3 Solidification cracking observation

Optical microscope (OM) was used to observe the surface of the weld bead. Fracture surface of the material in the weld bead was observed by scanning electron microscope (SEM).

## 5.3 Solidification cracking suppression via water-cooled GTAW

Fig. 5.2 (a) and (b) present the bead surface images after the GTAW and water-cooled GTAW of the U-type hot cracking test (stress condition: 13 kN). There were cracks on the weld bead surface during the GTAW; however, no cracks were observed in the water-cooled GTAW weld beads. Fig. 5.2 (c) presents the SEM images of the GTAW fracture surface. The fracture surface was divided into Regions A and B. These regions were observed from the magnified SEM images (enlarged Regions A and B). As can be seen from both images, dendrite structures were observed. Solidification cracking occurred on the GTAW bead surface, and not on the water-cooled GTAW bead surface.




(a) GTAW (b) Water-cooled GTAW (c) Fracture microstructure of GTAW

Fig. 5.2 The bead surface after the U-type hot cracking test and fracture surface microstructure observed by SEM.

## 5.4 Thermal strain calculation using finite element method

### 5.4.1 Finite element model

The finite element method for the U-type hot cracking test was designed by Quick welder software. Exploiting the resulting symmetry, half size of the U-type hot cracking test was established to decrease the calculation time of the finite element method (Fig. 16). The material constants used in this model is same as the Fig. 3.5. Although the water cooling process was applied during the U-type hot cracking test, the characteristics of other coolant were inputted in finite element method and compared to predict the behavior of solidification cracking according to the degree of cooling. The behavior of the thermal strain was compared by inputting the mechanical

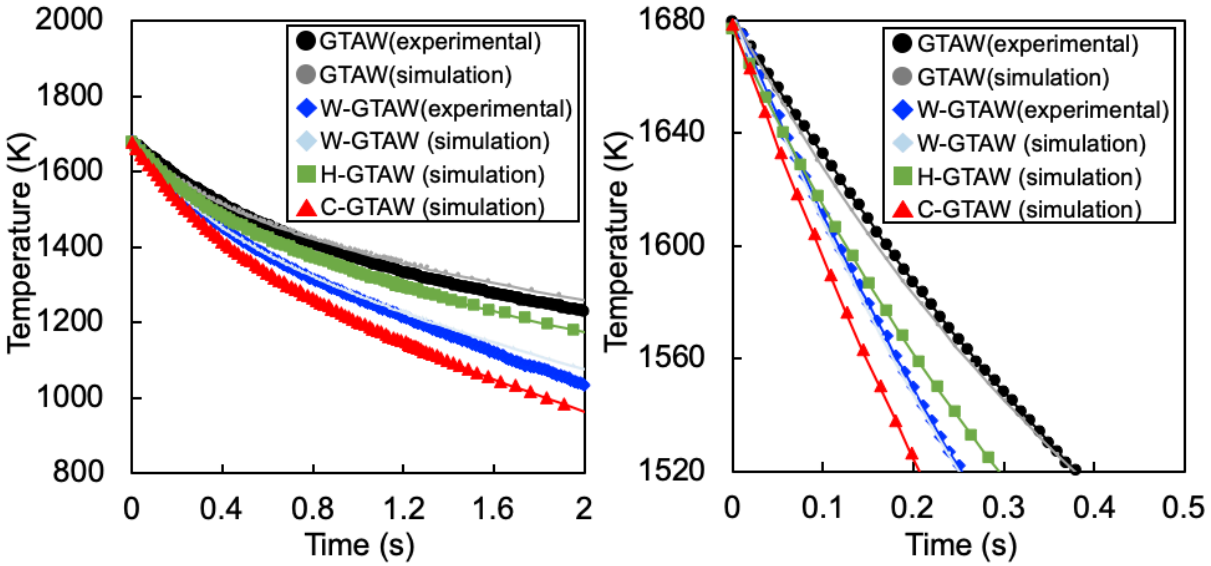
properties of hydrogen and the properties of the random coolant. Table 5.2 indicates the mechanical properties of the coolants.

Table 5.2 Mechanical properties of coolants.

| Coolant | Density (kg/m$^3$) | Temperature (K) | Conductivity(J/s·mm·K) |
|---|---|---|---|
| Air | 1.225 | 298 | $5\times10^{-6}$ |
| He | 0.1786 | | $3\times10^{-4}$ |
| Water | 997 | | $7\times10^{-4}$ |
| Cooler | 1.225 | | $12\times10^{-4}$ |

### 5.4.2 Comparison of weld bead shape and temperature history between experiment and simulation

In order to confirm the validity of the finite element model during U-type hot cracking test of GTAW and water-cooled GTAW, temperature history and weld bead shape were compared. The temperature history of the weld bead was measured by inserting a thermocouple into the weld pool during the GTAW (Fig. 5.3). Table 5.3 shows the bead morphology comparison between experimental and calculated results. The bead sizes from the simulation and experimental results were in good agreement, with a deviation of less than 10%. The experimental and simulation results were in good agreement both temperature history. Therefore, the finite element method verified the identical results with the experimental results with respect to the weld bead morphology and temperature history. The solidification cracking behavior was predicted when He and cooler were used using the final element method.




(a) Temperature range: 2000 – 800 K. (b) Temperature range: 1680 – 1520 K

Fig. 5.3 Time dependent temperature profiles according to welding speed condition

Table 5.3 Comparison of the experimental and simulation results.

| Welding process | Width of weld bead (mm) | | Depth of weld bead (mm) | |
|---|---|---|---|---|
| | Experiment | Simulation | Experiment | Simulation |
| GTAW | 5.14 | 5.11 | 0.99 | 1.04 |
| Water-cooled GTAW | 5.17 | 5.11 | 1.03 | 1.04 |

## 5.5 Theoretical approach to solidification cracking susceptibility

The BTR is characterized by the solidification initiation and completion temperatures. The Varestraint test is one of the most-used methods for the evaluation of the weld solidification cracking susceptibility [116-118]. The BTR is measured by bending the specimen with a bending block on the back of the weld specimen. However, the water cooling process was difficult to carry out during the Varestraint test due to the interruption of the bending block. Therefore, in this study, the solidification initiation and completion temperatures were calculated based on the supercooling and segregation models, respectively. In this chapter, the BTR according to welding conditions was calculated by metallurgical analysis method explained in Chapter 3.6. Table 5.4 shows conditions for numerical calculations. The cooling rate for each condition was measured in Fig. 5.3 (b).

Table 5.4 Conditions for numerical calculations.

| Dendrite radius (μm) | | | 10 | |
|---|---|---|---|---|
| Number of mesh division | | | 100 | |
| Solidification rate (mm/s) | | | 5 | |
| Welding condition | GTAW | H-GTAW | W-GTAW | C-GTAW |
| Cooling rate (K/s) | 420 | 525 | 620 | 760 |

*H-GTAW: He-cooled GTAW, W-GTAW: Water-cooled GTAW and C-GTAW: cooler-cooled GTAW

The solidification initiation temperature was 1680 K under both welding conditions. In the water-cooling GTAW and He-cooled GTAW, the temperatures were constant (1680 K). In the cooler-cooled GTAW, the solidification initiation temperature was 1678 K

Fig. 5.4 shows the amount of segregation concentration in residual liquid during solidification using solidification segregation model. Fig. 5.4 shows a comparison of segregation amounts of low-melting-point elements P, C and S according to welding condition.

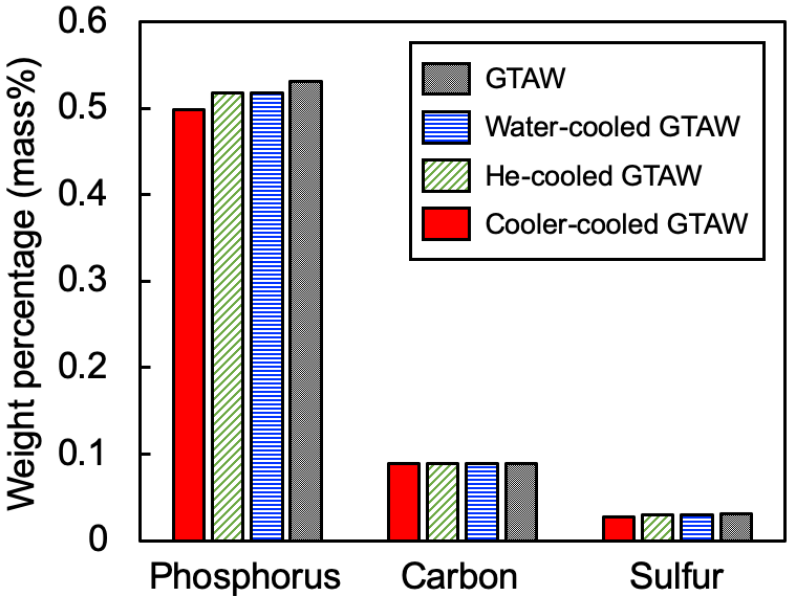


Fig. 5.4 Solidification segregation concentration according to welding conditions.

According to the cooling process, the segregation of P decreased and segregation of C and S also slightly decreased. Under GTAW conditions, the solidification completion temperature is 1520K. In the case of water-cooled GTAW, the solidification completion temperature slightly increased by 1522K due to a decrease in segregation of low-melting point elements. He-cooled GTAW showed the same solidification completion temperature as water-cooled GTAW. In the cooler-cooled GTAW, which has the fastest cooling rate, the segregation concentration decreased the most and the solidification completion temperature was 1523 K. The BTR calculated based on the supercooling model and solidification segregation model was 160 K under the GTAW. In the condition of He-cooled and water-cooled GTAW, the BTR was 159 K. In the case of cooler-cooled GTAW, the BTR was the smallest at 155 K. The BTR was decreased by the increase in conductivity of coolant. However, cooling process did not have an significant influence on the solidification cracking susceptibility.

### 5.6 Evaluation of solidification cracking susceptibility in coolant-cooled GTAW

A hot ductility curve was obtained based on a combination of the solidification initiation and completion temperatures, in addition to the critical strain. Due to an increase in the conductivity of coolant, the cooling rate was increased and solidification segregation concentration in the residual liquid decreased, resulting in decreasing in the BTR. However, cooling process did not have an significant influence on the solidification cracking susceptibility. The critical strain has not changed according to the cooling rate of the weld bead (Fig. 4.10). Therefore, the critical strain was employed from the results of GTAW (Fig. 3.10). Fig. 5.5 shows the hot ductility curves according to welding conditions (BTR: 155-160 K). There was no significant difference in hot ductility curves according to the welding process. This implies that the change in the hot ductility curve does not significantly cause an increase in solidification cracking.

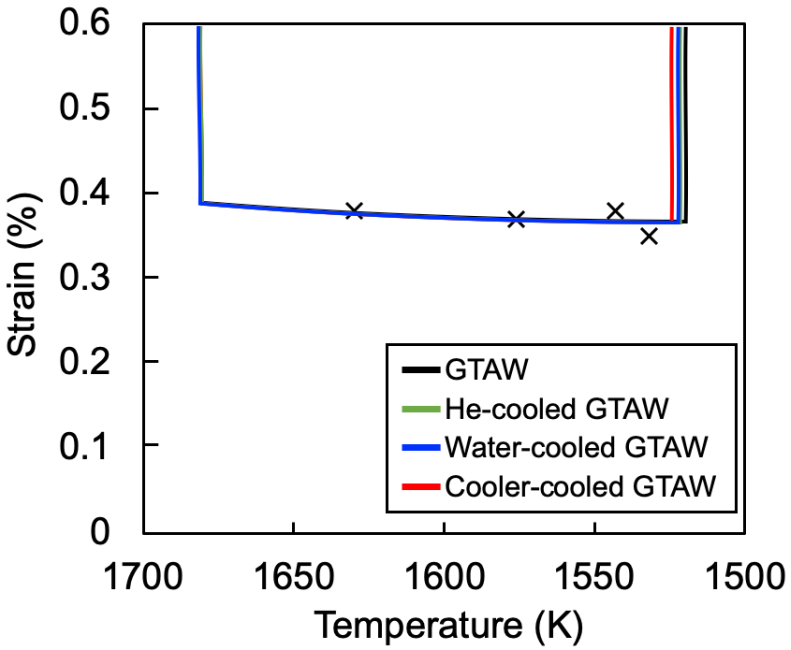
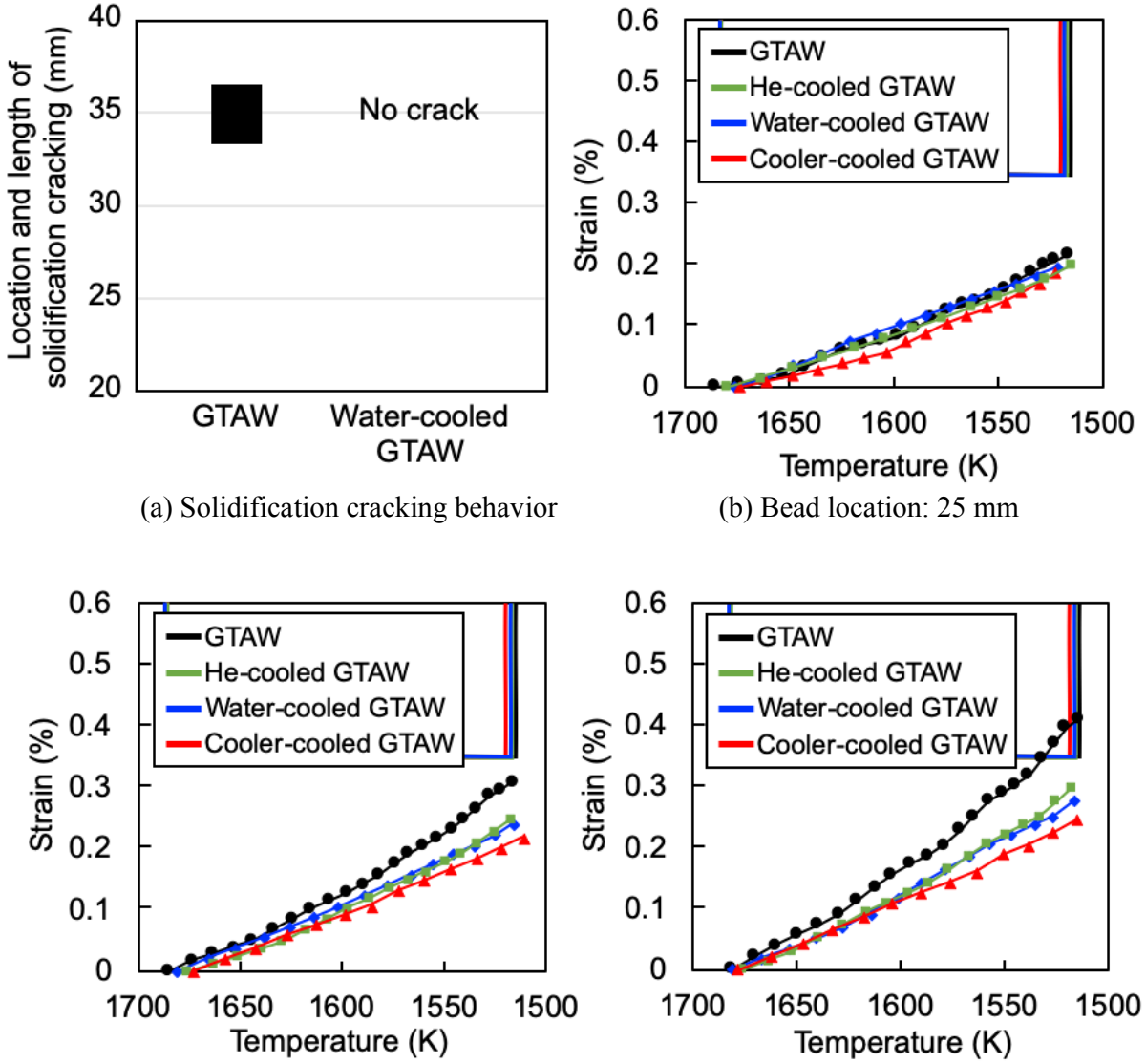



Fig. 5.5 Hot ductility curves according to welding conditions.

### 5.7 Influence of cooling process on solidification cracking behavior

Solidification cracking can be explained by the intersection of the hot ductility curve and thermal strain. Fig. 5.6(a) shows the experimental result and Fig. 5.6(b)-(d) present the hot ductility curve and thermal strain according to welding process and bead location (25-35 mm). The solidification cracking behavior observed by experiment during GTAW and water-cooled GTAW was shown in Fig. 5.6(a). The solidification cracking behavior with other coolant was replaced by the results predicted by ductility curve and thermal strain.




(a) Solidification cracking behavior

(b) Bead location: 25 mm

(c) Bead location: 30 mm

(d) Bead location: 35 mm

Fig. 5.6 Evaluation of solidification cracking behavior according to welding condition. Hot ductility curve and thermal strain comparison

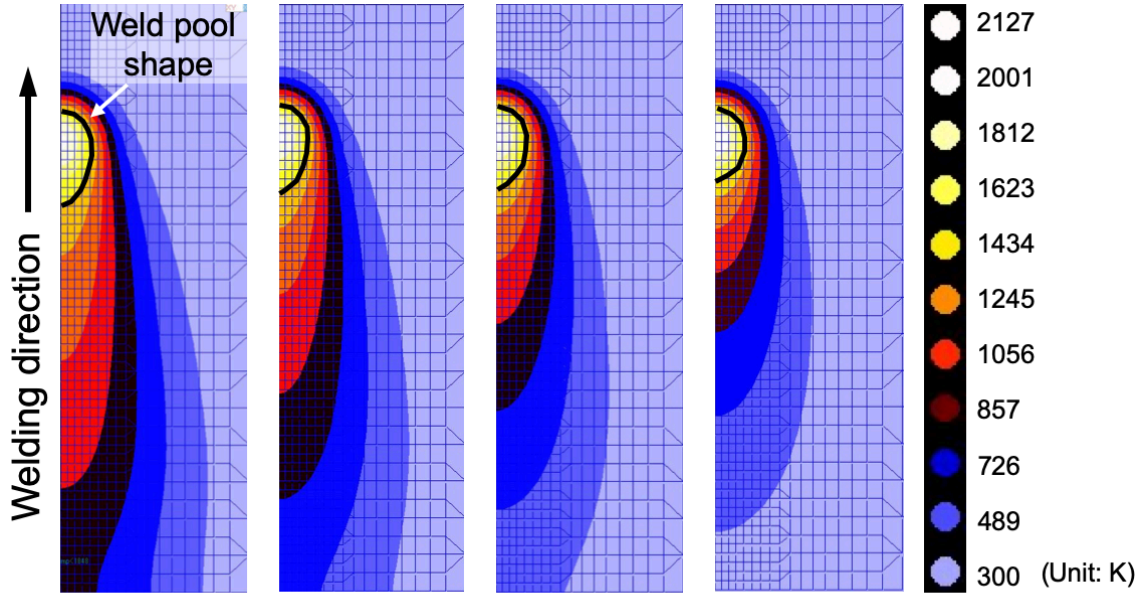
The thermal strain was derived from the finite element analysis results under a stress level of 13 kN in the U-type hot cracking test. The thermal strain of GTAW intersected the hot ductility curve at 35 mm bead location , thus resulting in solidification cracking. However, the thermal strain of the GTAW applied with water-cooling processes decreased below that of the GTAW, and it did not

intersect the hot ductility curve at all bead location (25-35 mm). Also, no intersections were observed in He and cooler-coiled GTAW. As conductivity increased, the slope of the thermal strain decreased. Therefore, the water-cooled GTAW prevented solidification cracking by decreasing the thermal strain of the weld bead. It is also expected that He and high conductivity coolant will prevent solidification cracking in U-type hot cracking test of GTAW.

## 5.8 Governing factors and controlling of thermal strain behavior in coolant-cooled GTAW

### 5.8.1 Temperature distribution

Fig. 5.7 shows the temperature distribution according to cooling process calculated using finite element simulation method. The solid-liquid co-existence zone was calculated using the temperature history employed by the finite element method. Table 5.5 shows solid-liquid co-existence zone according to welding conditions. For the constant weld bead shape under the all welding conditions, the amount of heat input was also increased as the thermal conductivity of the coolant increased. However, despite the increase in the amount of heat input, the solid-liquid co-existence zone was decreased and the cooling rate of the weld bead was increased.



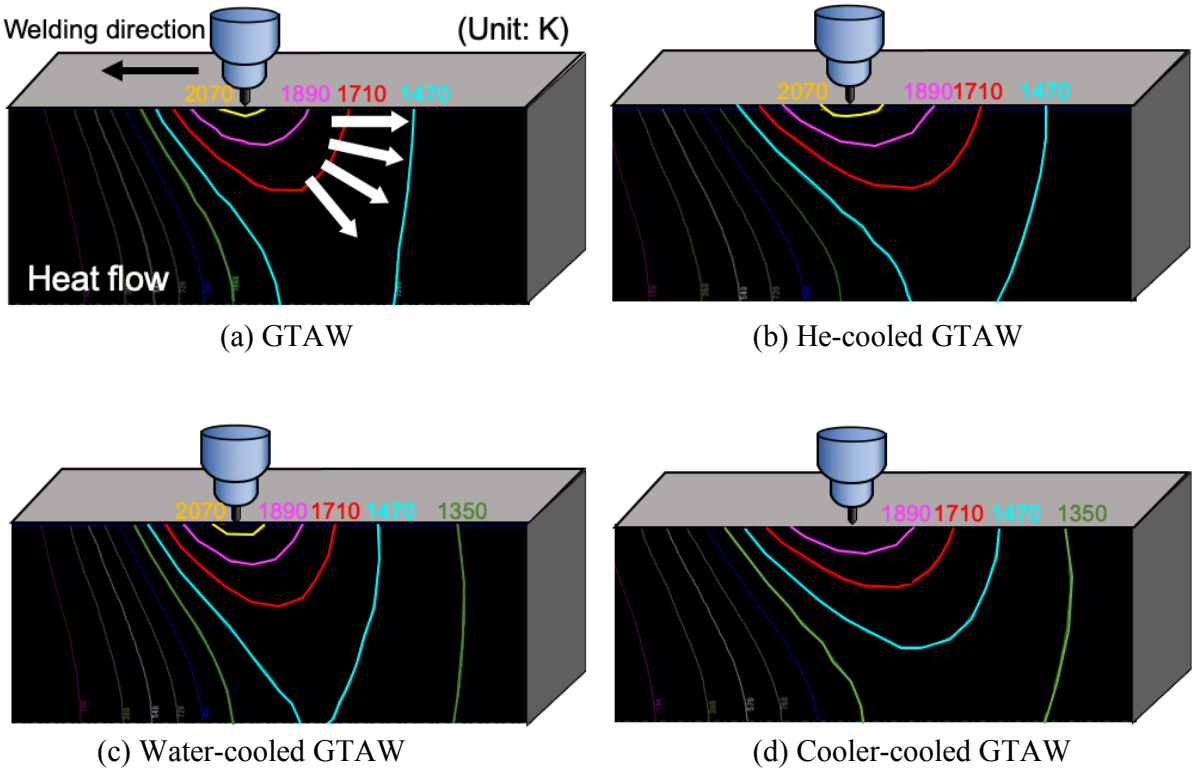

(a) GTAW (b) H-GTAW (c) W-GTAW (d) C-GTAW

Fig. 5.7 Temperature field according to cooling process calculated by finite element method. (H-GTAW: He-cooled GTAW, W-GTAW: water-cooled GTAW and C-GTAW: cooler-cooled GTAW)

Table 5.5 Length of solid-liquid co-existence zone.

| | Welding condition | | | |
|---|---|---|---|---|
| | GTAW | He-cooled GTAW | Water-cooled GTAW | Cooler-cooled GTAW |
| Solid-liquid co-existence zone (mm) | 2.3 | 1.7 | 1.4 | 1.1 |

To compare the effect of the cooling process on the reduction of solid-liquid co-existence zone, the temperature fields of vertical section were compared. Fig. 5.8 shows the temperature distribution during the welding calculated by finite element method. As the conductivity of the coolant increased, the gap between the isothermal lines was narrowed. In the research by Yuan Chen et al. [124], a continuous cooling water flow was imposed on back of a substrate to improve the base cooling effect and to control the heat flow during a laser additive manufacturing. The imposed cooling water flow on the back of the substrate increased the vertical temperature gradient, then the vertical heat dissipation was increased and uniformed, and accordingly, the lateral heat dissipation was weakened. Therefore, the cooling process increased the heat dissipation flow of the welds, increasing the cooling rate, and reducing the solid-liquid co-existence zone.




(a) GTAW (b) He-cooled GTAW

(c) Water-cooled GTAW (d) Cooler-cooled GTAW

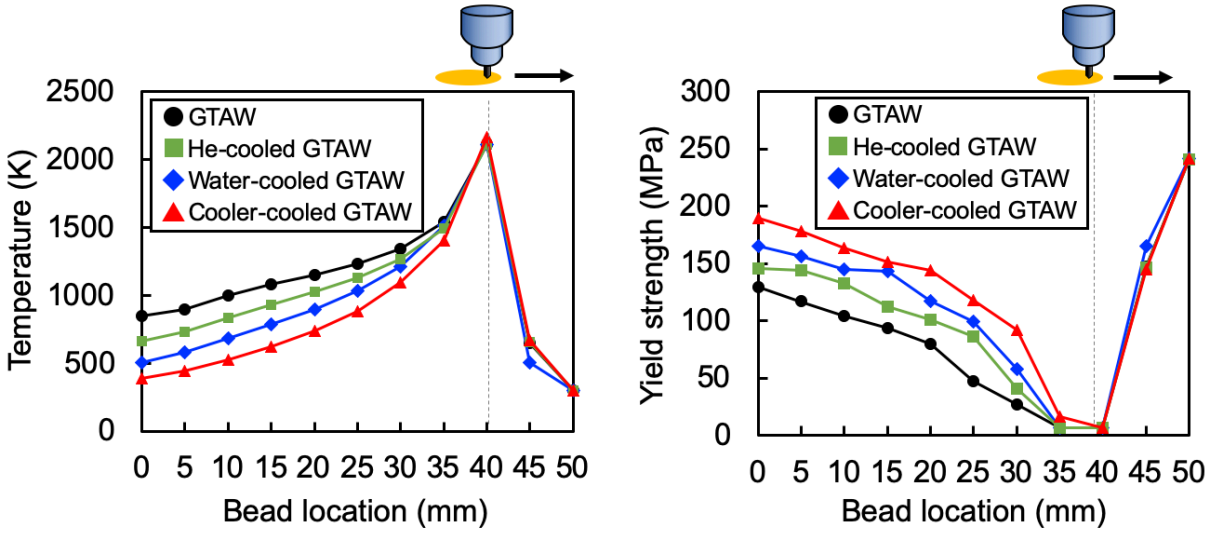
Fig. 5.8 Temperature field for heat dissipation comparison.

### 5.8.2 Controlled by cooling process

The effect of the decrease in the solid-liquid coexistence area with the cooling process on the behavior of the thermal strain was investigated. Fig. 5.9 shows the temperature distribution calculated using finite element simulation method. Fig. 5.9(a) shows the temperature distribution calculated by the finite element simulation method according to the bead location when the heat source passes through an arbitrary location (40 mm). Although the same maximum temperature was obtained at 40 mm, the low temperature distribution was appeared in the cooling-GTAW condition because of a decrease in solid-liquid co-existence zone. As the conductivity of the coolant increased, the cooling degree of the weld bead was increased.

Under the same welding timing condition, the yield strength distribution was calculated according to the bead location (Fig. 5.9(b)). The cooling-GTAW condition with lower temperature

distribution than the GTAW, had high yield strength distribution on the weld bead. The high yield strength distribution is hard to plastic deformation resulting in solidification cracking suppression. Therefore, an increase in yield strength distribution with increasing coolant conductivity decreased the slope of the thermal strain, resulted in the decreased slope of the thermal strain, and it prevented solidification cracking.




(a) Temperature distribution (b) Yield strength distribution

Fig. 5.9 Temperature and yield strength distribution calculated by finite element method.

Fig. 5.10 presents the stresses applied to the weld bead during solidification. The stress applied to the weld bead in cooling GTAW was lower than that in GTAW. As the conductivity of the coolant increased, the stress applied to the weld bead was decreased.

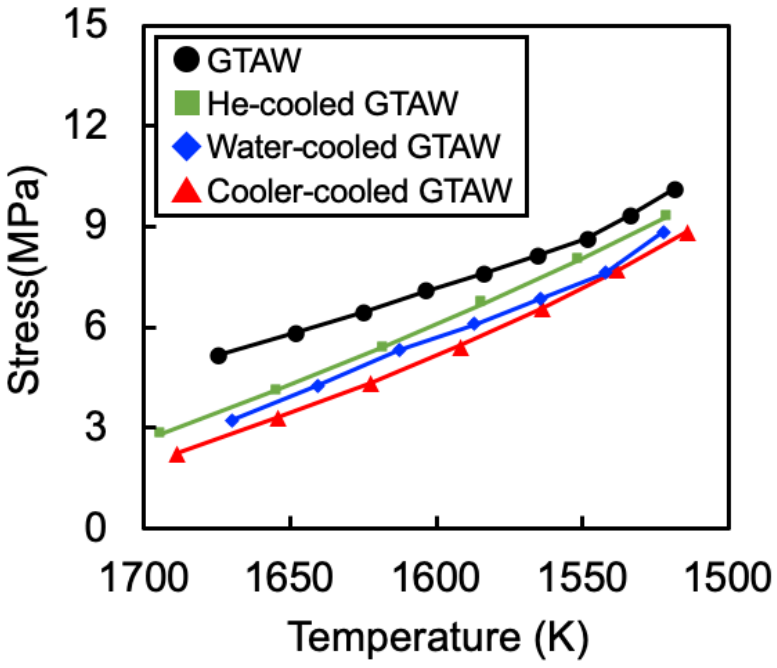



Fig. 5.10 Stress loaded on the weld bead during solidification.

The stress concentration in the solid-liquid co-existence zone was reported as one of the solidification cracking occurrence criterions [120-122]. Due to an decrease in the solid-liquid co-existence zone by the cooling process, a decreased stress was applied to the weld bead. As a result, an decrease in the solid-liquid co-existence zone became suppressive to solidification cracking due to an decrease in the slope of the thermal strain curve by the yield strength reduction and the decreased loaded stress. The relation between stress and strain could be explained by the following Equation (20).

$$\sigma = \mathrm{E} \times \varepsilon \tag{20}$$

where $\sigma$, E and $\varepsilon$ denote the stress, Young's modulus and strain, respectively. The Young's modulus values for each temperature axis in Fig. 5.6 were the same, irrespective of the welding condition, as it was only dependent on the temperature (Fig. 3.5). However, different strain values were obtained due to the different temperature distribution with respect to the welding conditions (Fig. 5.9). The reduction of the thermal strain by the cooling process decreased the stress applied to the weld bead. The decrease in temperature of the specimen by the cooling process during GTAW resulted in an increase in the yield strength, and solidification cracking was prevented due to a decrease in the thermal strain and the stress applied to the weld bead.

## 5.9 Summary

In the Chapter 4, it was found that the increase in heat input was vulnerable to the solidification cracking. Therefore, in this chapter, in order to suppress the solidification cracking, water was flowed on the opposite side of the specimen during GTAW during the U-type hot cracking test. In addition, the finite element method was used to predict the behavior of solidification cracking according to the conductivity change of coolant. The hot ductility curve and the thermal strain was calculated and compared to investigate the solidification cracking behavior. The mechanical properties of the weld bead were compared and analyzed using the finite element method to investigate the behavior of thermal strain.

The summarized conclusions are as follows;

1) From the fact that the critical strain is not affected by the cooling rate, the critical strain according to the cooling process was used as the value measured during GTAW.
2) Solidification initiation and completion temperatures were calculated by KGT model and solidification segregation model respectively. The solidification initiation temperature was not changed. However, the segregation concentration of S, P and C in the residual liquid decreased with increasing cooling rate. Therefore, the solidification completion temperature increased. However, the BTR didn't change enough to affect the solidification cracking behavior change.
3) The thermal strain was calculated using the finite element method. As the conductivity of the coolant increased, the thermal strain slope decreased and intersection between hot ductility

curve did not observed. As a result, the solidification cracking was prevented by the cooling process.

4) Increasing of the coolant conductivity increased the heat dissipation of the weld bead, resulting in increasing the cooling rate and decreasing the solid-liquid coexistence zone. Therefore, the temperature distribution of the weld beads decreased and the yield strength increased. Increasing yield strength suppressed plastic deformation and suppressed the solidification cracking.

# Chapter 6 Effect of temperature distribution of HAZ on solidification cracking

## 6.1 Introduction

Austenitic stainless steel exhibits excellent high-temperature properties and good ductility and is thus widely used in industries such as fuel cells, steam power, and nuclear equipment. However, fully austenitic stainless steel shows great susceptibility to hot cracking [25, 88-90], which is disadvantageous for its successful application.

A type 310S stainless steel is highly susceptible to hot cracking [20, 23, 25]. Therefore, the relationship between welding speed and hot cracking susceptibility of 310S steel was studied. It is common knowledge that solidification brittleness temperature range (BTR) in 310S steel decreases as the welding speed is increased [72, 104]. Wang et al. [73] compared the BTR difference according to welding speed through 2-dimensional temperature measurement. Kadoi et al. [74] demonstrated that the BTR changes based on solidification behavior and microstructure according to welding speed, using a high-speed camera. Also, Chun et al. [116] reported the BTR variation based on the segregation concentration behavior of low-melting point elements (P and S) using a metallurgical analysis model. From a thermomechanical point of view, the occurrence of hot cracking can be elucidated by the intersection of the hot ductility curve and thermal strain [120]. Therefore, in order to explain the hot cracking behavioral changes with regards to the welding condition, not only the hot ductility curve but also the thermal strain must be considered.

Therefore, in this study, we observed the changes in hot cracking during the U-type hot cracking test according to welding condition. The behaviors of the hot ductility curve and the thermal strain was analyzed based on the metallurgical model and finite element method (FEM) results. In addition, this study suggests the optimal welding conditions to suppress hot cracking in full austenitic stainless steel.

## 6.2 Materials and experimental procedure

### 6.2.1 Material

A type 310S stainless steel with solidification mode A was used. The size of specimen is 100×50×2 mm. The chemical composition of the steel is shown in Table 3.1. For the removal of the surface metal oxides and other tarnishes, the specimen was cleaned by ethanol prior to welding.

### 6.2.2 U-type hot cracking test according to welding speed

The U-type hot cracking test was conducted for stress loading (loaded stress: 12 kN) on the weld bead during the GTAW (Fig. 6.1). In order to investigate the optimization welding condition for solidification cracking suppression, the solidification cracking experiments were performed according to different welding speed condition. Arc current was set in the condition where bead shape did not change. Table 6.1 lists the welding conditions.

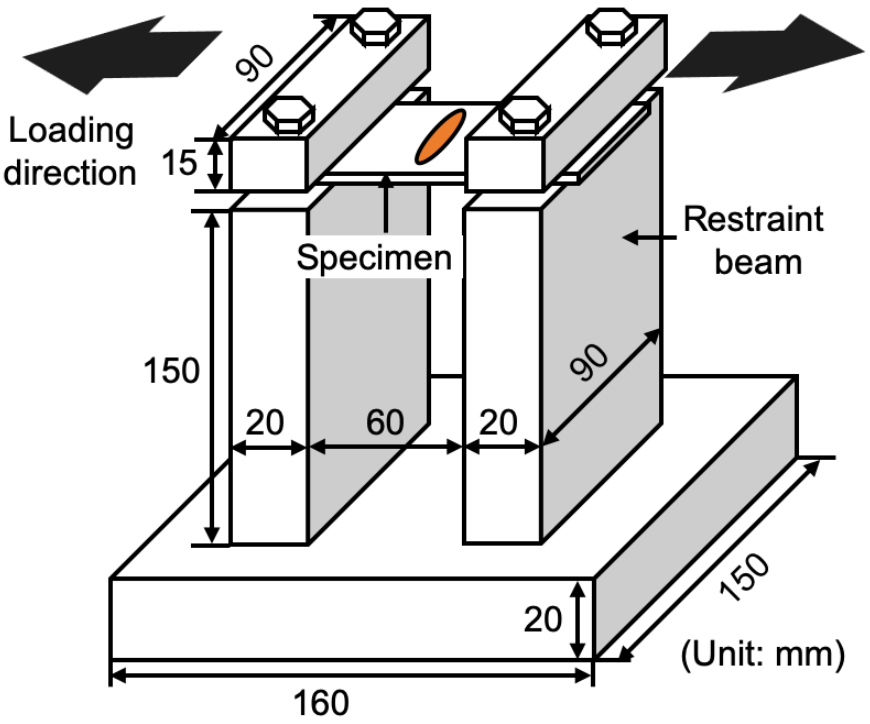



Fig. 6.1 Schematic illustration of U-type hot cracking test.

Table 6.1 GTAW conditions in U-type hot cracking test.

| Parameters | Values | | |
|---|---|---|---|
| Loading stress (kN) | 12 | | |
| Welding speed (mm/s) | 5 | 6 | 7 |
| Welding current (A) | 110 | 120 | 140 |
| Arc length (mm) | 1 | | |
| Electrode radius (mm) | 2.4 | | |
| Electrode extension (mm) | 15 | | |
| Electrode angle (°) | 50 | | |
| Shielding gas | Ar | | |
| Gas flow rate (l/min) | 20 | | |

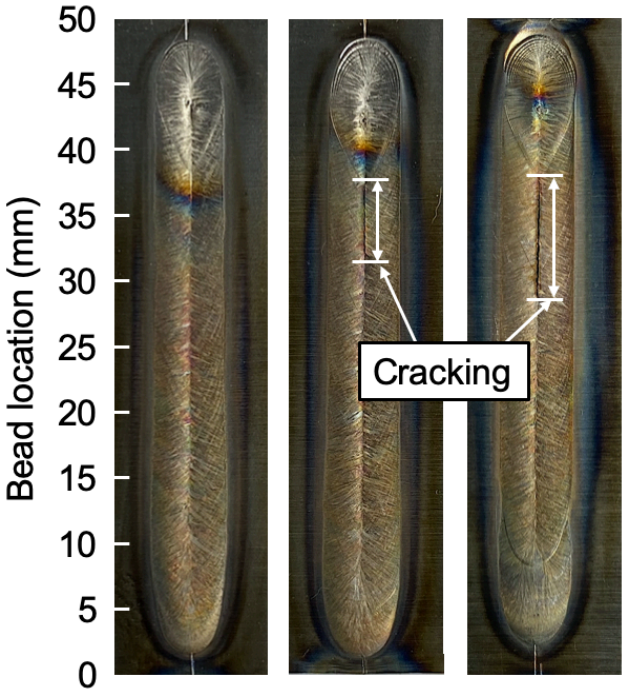
### 6.2.3 Solidification cracking observation

Optical microscope (OM) was used to observe the surface of the weld bead. Fracture surface of the material in the weld bead was observed by scanning electron microscope (SEM).

## 6.3 Solidification cracking behavior according to welding speed

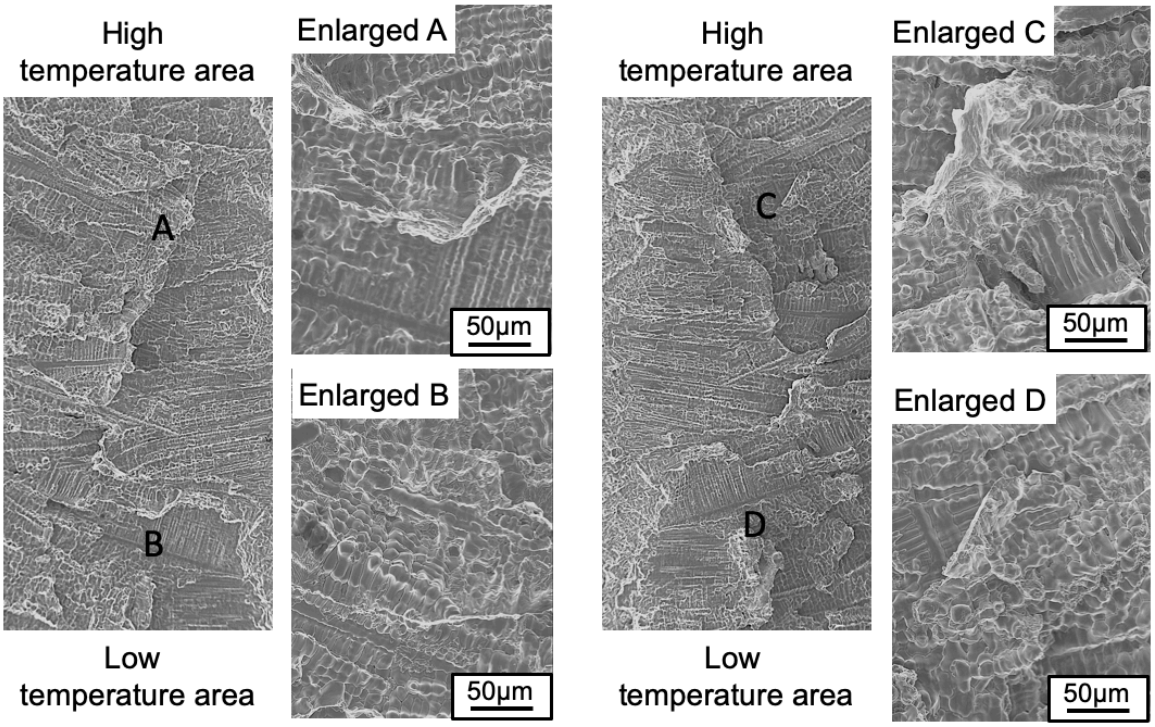
Fig. 6.2 shows the bead surface images after the GTAW of the U-type hot cracking test according to welding speed (stress condition: 12 kN). In the 7 mm/s condition (Fig. 57 (c)), cracks are observed to occur in the weld bead. However, the degree of cracking reduces upon the welding

speed decrease (6 mm/s) (Fig. 57 (b)), and no cracks are observed in 5 mm/s welding speed (Fig. 6.2(a)).




(a) 5 mm/s (b) 6mm/s (c) 7mm/s

Fig. 6.2 The bead surface after U-type hot cracking test.




(a) Fracture microstructure of 6 mm/s (b) Fracture microstructure of 7 mm/s

Fig. 6.3 SEM images of fracture surface according to welding speed.

The fracture surfaces of the 6mm/s and 7mm/s GTAW samples were observed via SEM. Fig. 6.3 shows the fracture microstructure according to welding speed. The fracture surface was divided into Regions a-d. These regions were observed from the magnified SEM images (enlarged Regions a-d). As can be seen from both images, dendrite structures were observed on the fracture surface, which confirms the occurrence of solidification cracking.

## 6.4 Thermal strain calculation using finite element method

### 6.4.1 Finite element model

The finite element method for the U-type hot cracking test was designed by Quick welder software. Exploiting the symmetrical welding, half of the workpiece was simulated to decrease the simulation time in the finite-element model to decrease the calculation time of the finite element method (Fig. 3.4). In the U-type hot cracking test, In the U-type hot cracking test, the bent restraint beam applied tensile stress to the specimen. The bent restraint beam was restored, due to the specimen expansion during the welding. Therefore the tensile stress loaded on the specimen decreased. The restraint beam was included in the model to reproduce this phenomenon. The material constants used in this model is same as the Fig. 3.5.

### 6.4.2 Comparison of weld bead shape and temperature history between experiment and simulation

The weld bead geometries according to welding conditions calculated by means of simulations were compared with the experiment results (Table 6.2). The calculated geometry of the fusion zone was determined based on the melting temperature (1680 K) of 310S stainless steel. The bead sizes from the simulation and experimental results were in good agreement, with an error of less than 10%.

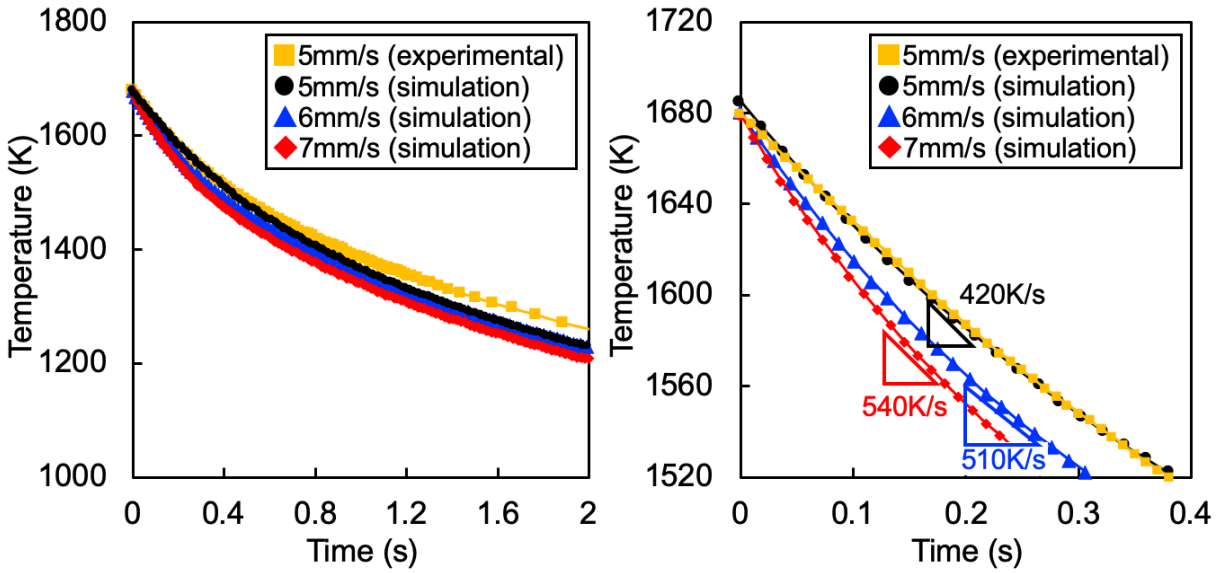
Fig. 6.4 shows the temperature history comparison between experimental results and calculation results. The cooling rate was measured by inserting a thermocouple into the molten pool during welding. The thermal strain measurement explained in the Chapter of 3.5. The experimental and simulation results were in good agreement. Thus, the finite-element model for GTAW were verified based on the comparison of the experimental and simulation results. The temperature history of 6, 7mm/s conditions were replaced by the simulation result (Fig. 6.4).

Table 6.2 Comparison of the experimental and simulation results.

| Welding process | Width of weld bead (mm) | | Depth of weld bead (mm) | |
|---|---|---|---|---|
| | Experiment | Simulation | Experiment | Simulation |
| 5 mm/s | 5.14 | 5.11 | 0.99 | 1.04 |
| 6 mm/s | 5.08 | 5.11 | 1.14 | 1.04 |
| 7 mm/s | 5.13 | 5.11 | 1.10 | 1.04 |

Fig. 6.4 compares the temperature history curves according to welding conditions. In the calculated solid-liquid coexistence temperature range (Chapter 6.5) , the cooling rate was increased

as the welding speed increased. Fig. 6.4 (b). However, when compared over a wide temperature and time axis, there was no significant temperature difference.




(a) Temperature range: 1800 – 1000 K (b) Temperature range: 1680 – 1520 K

Fig. 6.4 Time dependent temperature profiles according to welding speed condition.

## 6.5 Theoretical approach to solidification cracking susceptibility

The BTR was discussed by employing a metallurgical model. Generally, the BTR is characterized by solidification initiation and completion temperature. During the welding, segregation of solute elements occurs along with dendrite growth due to exhausting solute element from solid phase to residual liquid phase. Consequently, the solute content of the liquid continuously increases during the solidification. Therefore, the true solidification completion temperature deviates from the nominal solidus temperature. The solidification initiation and completion temperatures were calculated using the Kurz-Giovanola-Trivedi (KGT) model and solidification segregation model respectively. In this chapter, the BTR according to welding conditions was calculated by metallurgical analysis method explained in Chapter 3.6. Table 6.3 shows conditions for numerical calculations. The cooling rate for each condition was measured in Fig. 6.4 (b).

Table 6.3 Conditions for numerical calculations.

| | | | |
|---|---|---|---|
| Dendrite radius (μm) | | 10 | |
| Number of mesh division | | 100 | |
| Solidification rate (mm/s) | | 5 | |
| Welding speed (mm/s) | 5 | 6 | 7 |
| Cooling rate (K/s) | 420 | 510 | 540 |

The solidification initiation temperature was 1680 K in all welding conditions (5-7 mm/s). There was no effect of the supercooling degree on the solidification initiation temperature change according to the welding speed.

Fig. 6.5 shows the amount of segregation concentration in residual liquid during solidification using solidification segregation model. Fig. 6.5 shows a comparison of segregation amounts of low-melting-point elements P, C and S according to welding condition.

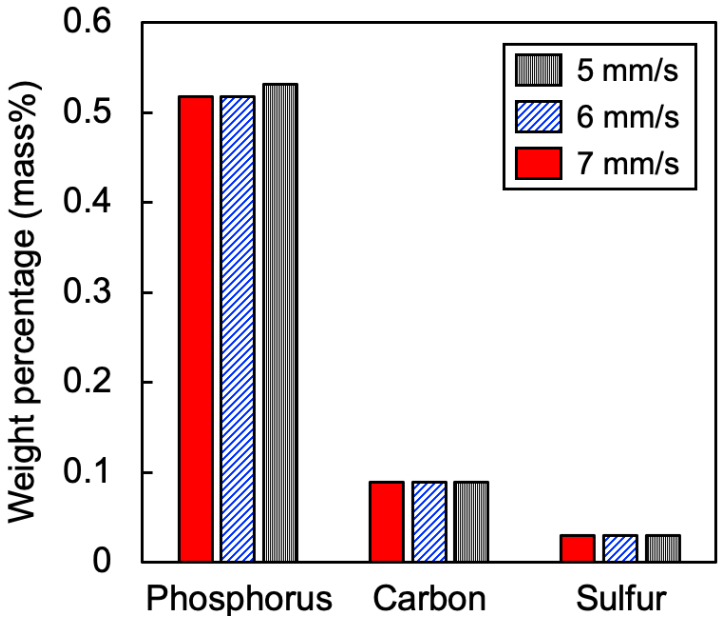



Fig. 6.5 Solidification segregation concentration according to welding conditions.

According to the welding speed, the segregation of P decreased and segregation of C and S also slightly decreased. Under GTAW conditions, the solidification completion temperature was 1520 K. In the condition of 6 mm/s and 7 mm/s solidification completion temperature was 1521 K. As the welding speed increased, the solidification completion temperature was slightly increased due to the inhabitation of segregation of low-melting point elements in residual liquid. Table 6.4 shows the BTR according to welding conditions. The BTR was slightly decreased as the welding speed increased. Therefore, the welding speed change did not significantly affect the solidification cracking susceptibility.

Table 6.4 BTR according to welding conditions.

| Welding speed (mm/s) | 5 | 6 | 7 |
|---|---|---|---|
| BTR (K) | 160 | 159 | 159 |

### 6.6 Evaluation of solidification cracking susceptibility

A solidification initiation temperature and completion temperature, in addition to the critical strain are required for the hot ductility curve. The solidification initiation temperature and

completion temperature viz; the BTR according to welding speed conditions were calculated by metallurgical analysis model (Table 6.4). As the welding speed increased, the segregation concentration of the residual liquid phase was slightly decreased, and also the BTR was slightly decreased. The critical strain was constant according to the cooling rate change of the weld bead (Fig. 4.10). Therefore, the critical strain was employed from the results of GTAW (Fig. 3.10). The $x$-axis in Fig. 3.10 was converted from time to temperature using the temperature history (Fig. 3.7) and all $\varepsilon_{CSR}$ were combined. Fig. 6.6 shows the hot ductility curves according to welding conditions (BTR: 159-160 K). There was no significant difference in solidification susceptibility according to the welding process. This implies that the change in the hot ductility curve does not significantly cause an increase in solidification cracking.

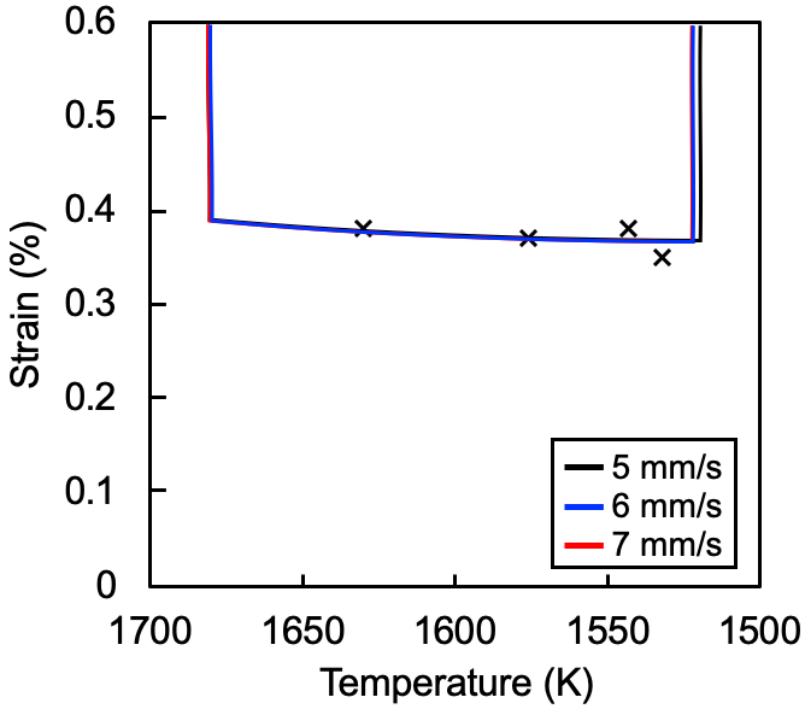
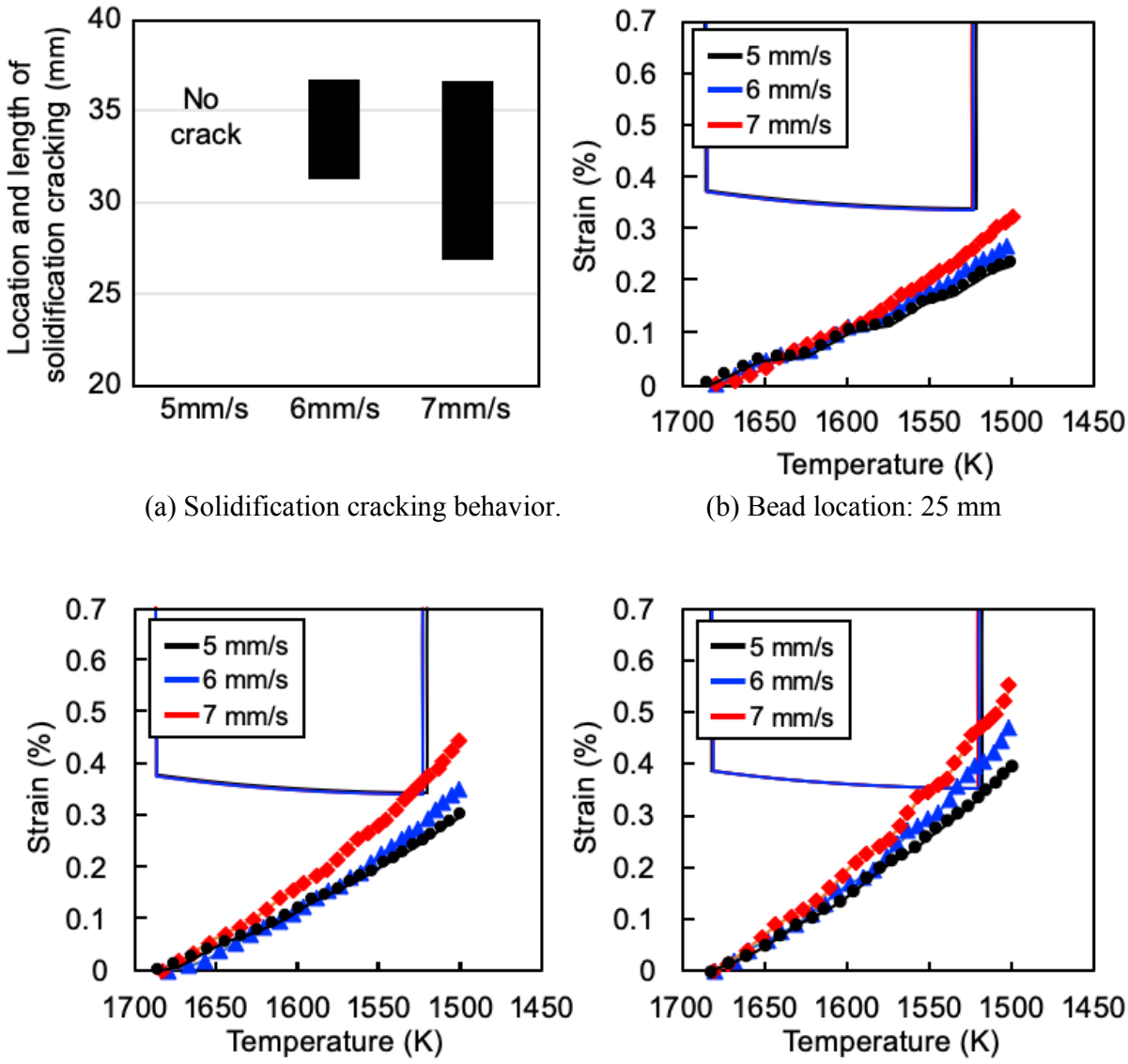



Fig. 6.6 Hot ductility curves according to welding conditions.

### 6.7 Influence of welding speed on solidification cracking behavior

The solidification cracking occurrence can be expressed through the intersection of the hot ductility curve and the thermal strain, which can be seen for comparison in Fig. 6.7. The thermal strains were derived from the finite element analysis results under a stress level of 12 kN in the U-type hot cracking test. Fig. 6.7(a) shows the experimental results of the solidification cracking behavior according to the welding conditions. The intersection between the thermal strain and the hot ductility curves according to the bead location was observed (Fig. 6.7(b)-(d)). At the bead location of 25 mm, the intersection of the two curves did not appear in all conditions (Fig. 6.7(b)), and solidification cracking was not observed on the bead surface (Fig. 6.2). At the location of 30 mm, the intersection was observed only in the 7 mm/s condition, and at 35 mm, the intersection occurred in both the 6 mm/s and 7 mm/s conditions. As the welding speed was increased, the

solidification cracking was elongated due to the increase in the thermal strain. Therefore, it is evident that the slope change of the thermal strain is a major factor in solidification cracking behavior.




(a) Solidification cracking behavior.

(b) Bead location: 25 mm

(c) Bead location: 30 mm

(d) Bead location: 35 mm

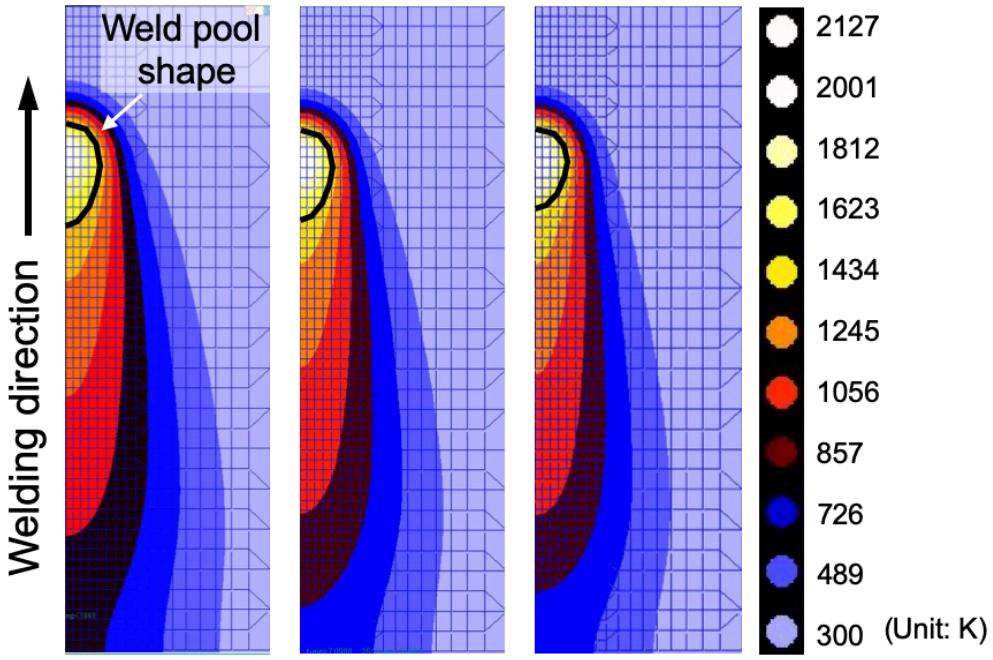
Fig. 6.7 Evaluation of solidification cracking behavior according to welding condition. Hot ductility and thermal strain comparison.

## 6.8 Changing mechanism of thermal strain behavior according to welding speed

### 6.8.1 Effect of welding speed on temperature distribution of weld bead

The temperature distribution investigated to compare the solidification cracking behavior according to the welding conditions. Fig. 6.8 shows the temperature distribution according to welding condition calculated using finite element simulation method. As the welding speed increased, the temperature distribution of the welding beads was decreased. The solid-liquid co-existence zone was measured using the temperature history employed by the finite element method

(Fig. 6.4). Table 6.5 shows solid-liquid co-existence zone according to welding conditions. An increase in welding speed reduced the solid-liquid co-existence zone due to an increase in cooling rate.




(a) 5mm/s (b) 6 mm/s (c) 7 mm/s

Fig. 6.8 Temperature field according to welding condition calculated by finite element method.

Table 6.5 Length of solid-liquid co-existence zone.

| | Welding condition | | |
|---|---|---|---|
| | 5 mm/s | 6 mm/s | 7 mm/s |
| Solid-liquid co-existence zone (mm) | 2.3 | 1.5 | 1.3 |

In order to investigate the cause of the effect of welding speed condition on the solid-liquid co-existence zone, the amount of heat input according to the welding conditions was calculated. The heat input (J/mm) can be expressed as Equation (21).

$$Heat\ input\ [\mathrm{J/mm}] = \frac{V \times A \times 60}{W} \tag{21}$$

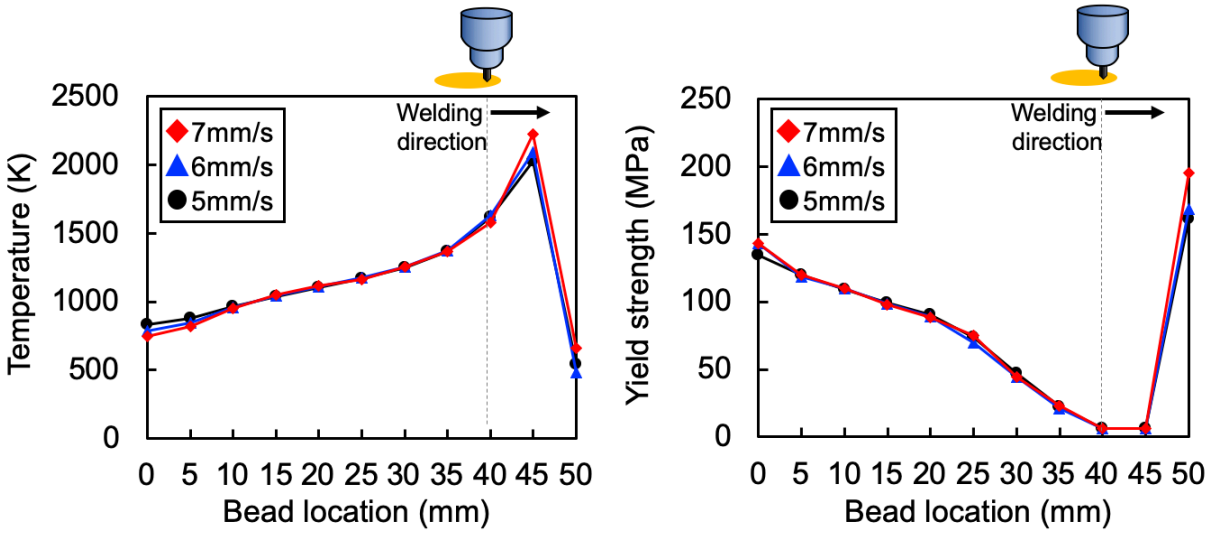
where V is the arc voltage (V), A denotes the welding current (A) and $W$ denotes the welding speed (mm/min). Table 6.6 shows the amount of heat input and cooling rate according to the welding conditions. In order to form the constant welding bead size, the current was also increased as the welding speed increased. An increase in welding speed decreased the amount of heat input, and thus the cooling rate was increased. Therefore, An increase in heat input according to a decrease

in welding speed increased the solid-liquid coexistence zone of the molten pool, resulting in the decreased cooling rate.

Table 6.6 Heat input and cooling rate according to welding speed change.

| Welding speed (mm/s) | Welding current (A) | Heat input (J/mm) | Cooling rate (K/s) |
|---|---|---|---|
| 7 | 140 | 200 | 540 |
| 6 | 125 | 208 | 510 |
| 5 | 110 | 220 | 420 |

Fig. 6.9(a), (b) shows the temperature and yield strength distribution calculated by the finite element simulation method according to the bead location when the heat source passes through an arbitrary location (45 mm).




(a) Temperature distribution (b) Yield strength distribution

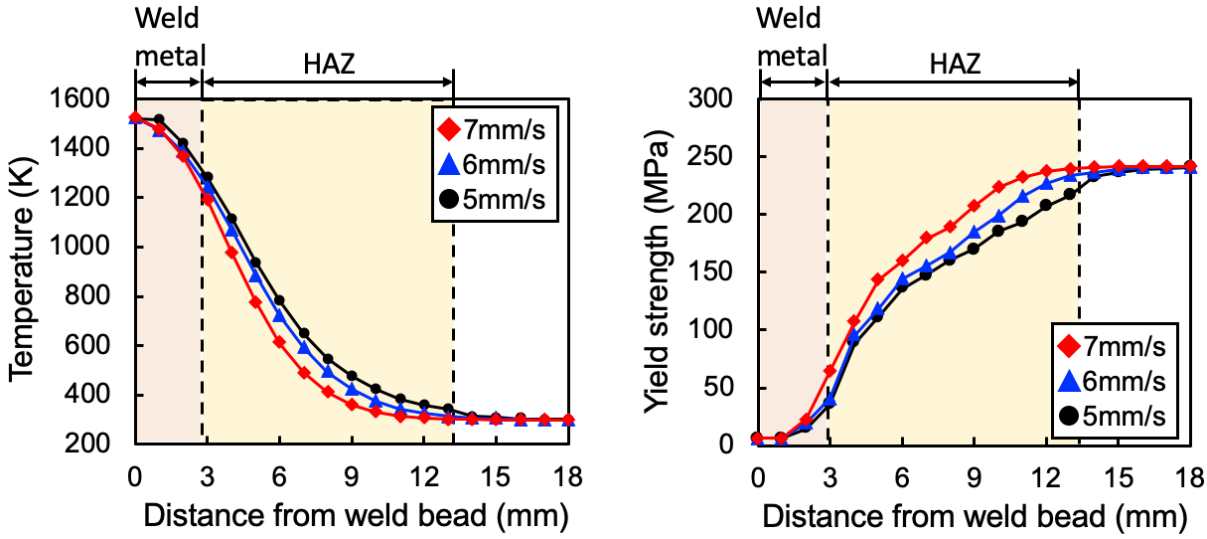
Fig. 6.9 Temperature and yield strength distribution calculated by finite element method.

The heat input is the largest in the 5 mm/s condition, but at the 45 mm bead location, the current was the largest in the 7 mm/s condition, therefore the temperature was the highest. However, although the solid-liquid co-existence zone changed according to welding speed, the temperature distribution of the welding beads did not significantly change (Fig. 6.9(a)). In the temperature history curve (Fig. 6.4(a)) in the range of solidification initiation/completion temperature, the cooling rate was increased as the welding speed increased. However, during the solidification process, the temperature difference was not increased and the parallel temperature history curve appeared (Fig. 6.4(b)). Therefore, the constant temperature distribution was formed in the temperature distribution of the weld (Fig. 6.9(a)). Since the temperature distribution was constant according to the welding conditions, the yield strength of the welding beads was also constant. Therefore, the differences in temperature and mechanical properties affected on thermal strain were not confirmed.

### 6.8.2 Thermal strain behavior controlled by thermal expansion of heat-affected zone

Okano et al. [124] compared not only the melting length along the welding direction but also the temperature distribution along the vertical direction of the welding direction to observe the effect of an amount of heat input on plastic deformation. In this study, no change in weld bead temperature and mechanical properties according to welding conditions was observed. Therefore, in order to explained the thermal strain, viz; solidification cracking behavior, the transverse temperature and yield strength distribution were considered. Fig. 6.10 shows the calculation results of temperature distribution (Fig. 6.10(a)) and yield strength distribution (Fig. 6.10(b)) along the vertical direction of welding using the finite element method. In the welding bead area, high temperature distribution was observed under the condition of 5 mm/s with the highest heat input. In the heat-affected zone (3-13 mm), an increase in temperature distribution was also observed with the increase in heat input. The difference in the temperature distribution of the welding beads according to the welding conditions was not observed, but the difference in the temperature distribution in the vertical direction of the welding was observed according to the amount of heat input. The difference in temperature distribution showed the difference in yield strength distribution. The lowest yield strength distribution was observed under the condition of 5 mm/s, which had the highest temperature in the heat-affected zone. The yield strength of the heat-affected zone was lowered due to a decrease in the temperature distribution with a decrease in heat input.

In order to investigate the effect of the temperature distribution and yield strength distribution of the heat-affected zone on the thermal strain, strain changes over time were compared. Fig. 6.11 shows the calculation results of strain over time in the center of the heat-affected zone (location: 9mm in *x*-axis direction) using the finite element method. The yield strength affected the amount of deformation in heat-affected zone. Under the condition of 5 mm/s with low yield strength distribution, strain was the highest due to the tensile stress loading during the U-type hot cracking test. The strain was decreased as the yield strength increased due to the reduction of heat input. During the U-type hot cracking test, the restraint beam constrained by external stress was relaxed during the welding process and tensile stress on the specimen was reduced. The increase in the amount of expansion of the heat-affected zone due to the increase in the amount of heat input relieved the stress on the weld during the U-type hot cracking test. Fig. 6.12 shows the stress loaded on the weld bead calculated by the finite element method during solidification according to the welding conditions. The increased expansion of the heat-affected zone relieved the stress on the weld during the U-type hot cracking test. As the welding speed decreased, the amount of expansion of the heat-affected zone was increased. Therefore, the amount of heat input increase due to the decrease in welding speed alleviated the stress applied to the weld bead. As a result, the thermal strain was decreased resulting in the suppression of solidification cracking.




(a) Temperature distribution. (b) Yield strength distribution

Fig. 3.10 Temperature and yield strength distribution calculated by finite-element model according to transverse location.

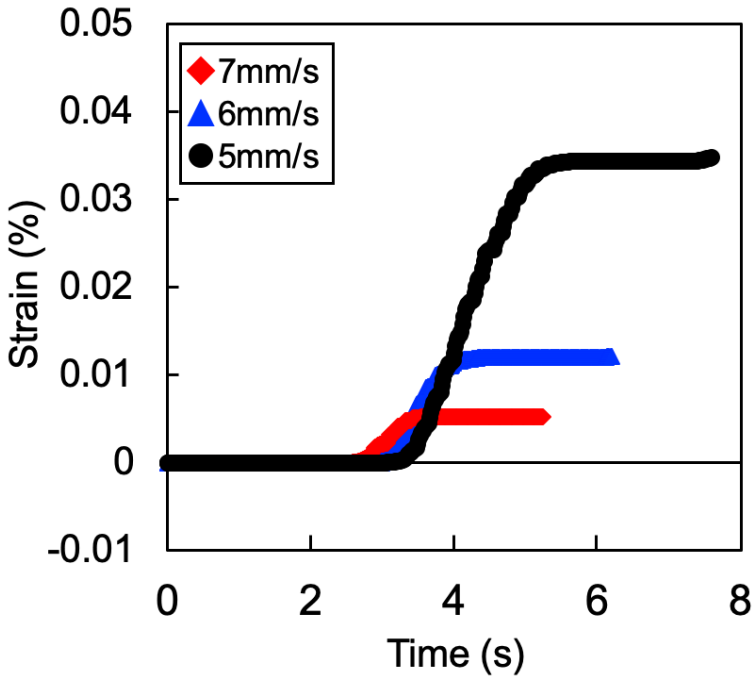



Fig. 6.11 Strain rate in the center of HAZ (location: 9mm in x-axis direction) according to welding time.

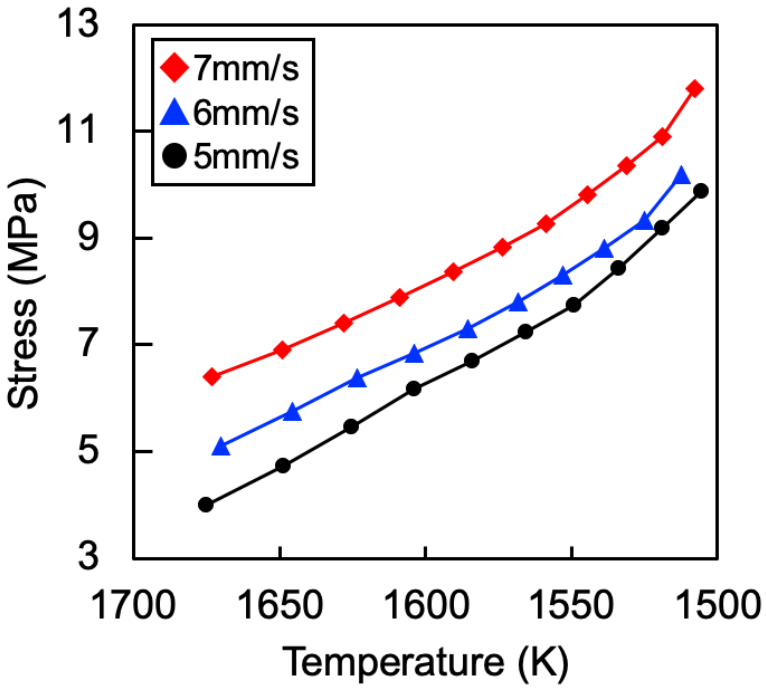



Fig. 6.12 Stress loaded on the weld bead during the solidification.

### 6.9 Summary

In the Chapter 5, The suppression of solidification cracking was possible by applying the water-cooling process. However, the welding process became complicated. Therefore, in this chapter, we will investigate the optimization welding conditions for solidification cracking suppression. The arc current value was also adjusted to constant the size of the welding bead according to the welding speed. The increase in welding speed was vulnerable to the solidification cracking. The hot ductility curve and the thermal strain was calculated and compared to investigate the solidification cracking behavior. The mechanical properties of the weld bead were compared and analyzed using the finite element method to investigate the behavior of thermal strain.

The summarized conclusions are as follows;

1) Solidification initiation and completion temperatures were calculated by KGT model and solidification segregation model, respectively. The solidification initiation temperature was constant. The segregation concentration of S, P and C in the residual liquid slightly decreased with increasing welding speed. The BTR didn't significantly change. Therefore, the solidification cracking susceptibility change didn't significantly affected the solidification cracking behavior.

2) The thermal strain was calculated using the finite element method. As the welding speed increased, the slope of the thermal strain increased. As a result, intersection with the hot ductility curve increased, resulting in vulnerable solidification cracking.

3) The difference in the temperature distribution of the welding beads according to the welding conditions was not observed. However, the heat input increase due to the decrease in welding speed increased the temperature distribution of heat-affected zone resulting in vulnerable to plastic deformation.

4) Decreasing the welding speed increased the amount of heat-affected zone expansion as the yield strength of the heat-affected zone decreased. In addition, with the expansion of the heat-affected zone, stress was reduced on the weld bead, which suppressed the hot cracking process.

# Chapter 7 Prevention of solidification cracking by thermal expansion control via parallel laser heating

## 7.1 Introduction

The metallurgical reason underlying solidification cracking has been attributed to stress concentration due to the segregation of low-melting-point elements (S, P) in the residual liquid [1, 12, 17, 83-84]. Therefore, researchers have proposed solidification cracking prevention methods based on the controlled segregation of low-melting-point elements. However, this has led to other problems; reducing the S and P content of stainless steel required a complicated and costly manufacturing process [36, 48-50, 82]. Meanwhile, increased carbon content was found to reduce the extent of microfissuring, and furthermore, increasing the Mn content to combine with excess S successfully prevented solidification cracking [55]. However, the use of these methods also deteriorated the corrosion resistance of stainless steel.

Therefore, researchers have proposed effective technologies to reduce crack formation without metallurgical side effects. Wang et al. [125] estimated the welding conditions to prevent solidification cracking during dual-beam welding. Gobel et al. [115] reported crack prevention via changing the temperature distribution around the weld bead using an induction coil. Here, we note that the thermomechanical reasons underlying solidification cracking have been elucidated by means of hot ductility curves and thermal strain. However, in these previous studies, the quantitative assessment of solidification cracking prevention is not adequate.

Therefore, in this study, we irradiated the base material with a laser beam to prevent solidification cracking during multi-beam GTAW. In addition, we consider the effect of the laser-beam irradiation on the thermal strain in detail.

## 7.2 Materials and experimental procedure

### 7.2.1 Material

A type 310S stainless steel with solidification mode A was used. The size of specimen is 100×50×2 mm. The chemical composition of the steel is shown in Table 3.1. For the removal of the surface metal oxides and other tarnishes, the specimen was cleaned by ethanol prior to welding.

### 7.2.2 U-type hot cracking test with multi-beam welding

The U-type hot cracking test was conducted for stress loading (loaded stress: 13 kN) on the weld bead during the GTAW with parallel laser beam irradiation (Fig. 7.1). The fiber laser beam was employed for basemetal heating (multi-beam welding). The laser power was set in the range where the steel did not melt. Tables 7.1, 7.2 list the multi-beam welding and U-type hot-cracking test conditions. The solidification cracking behavior according to the distance between the heat sources and the change in laser power was investigated.

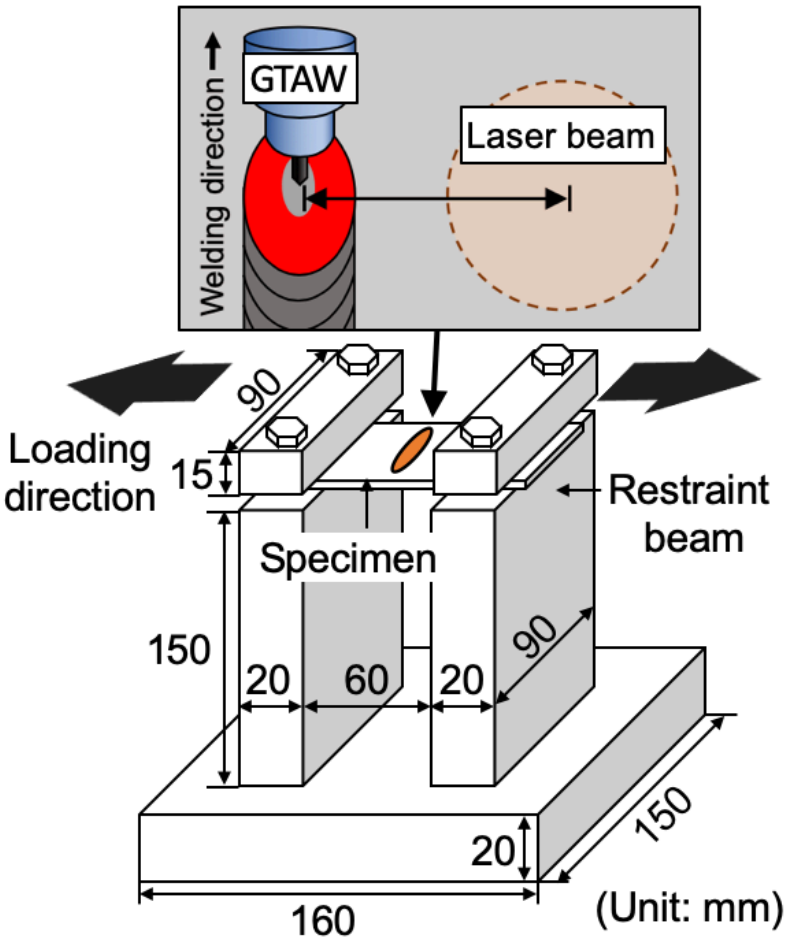



Fig. 7.1 Schematic diagram of the U-type hot cracking test during GTAW and multi-beam welding.

Table 7.1 GTAW conditions in multi-beam welding during the U-type hot cracking test.

| Heat source | Parameters | Values |
|---|---|---|
| GTAW | Welding speed (mm/s) | 5 |
| | Welding current (A) | 110 |
| | Arc length (mm) | 1 |
| | Electrode radius (mm) | 2.4 |
| | Electrode extension (mm) | 15 |
| | Electrode angle (°) | 50 |
| | Shielding gas | Ar |
| | Gas flow rate (l/min) | 20 |

Table 7.2 Laser conditions in multi-beam welding during the U-type hot cracking test.

| Heat source | Parameters | Values |
|---|---|---|
| Laser | Laser power (kW) | 0.5, 0.8 |
| | Laser angle (°) | 32 |
| | Defocus length (mm) | 200 |
| | Laser spot size (mm) | 10 |
| | Distance between heat sources (mm) | 5, 15 |

### 7.2.3 Solidification cracking observation

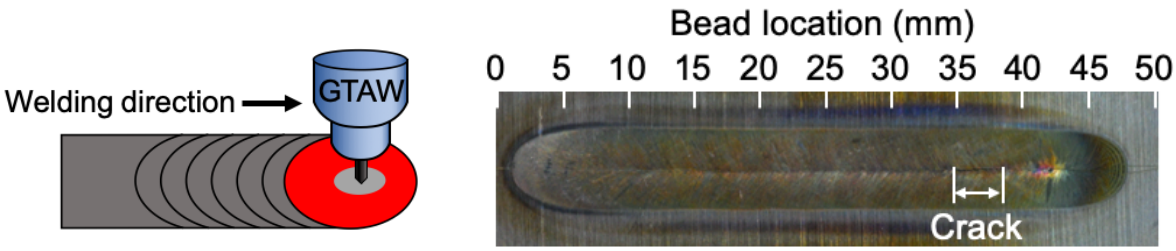
Optical microscope (OM) was used to observe the surface of the weld bead. Fracture surface of the material in the weld bead was observed by scanning electron microscope (SEM).

## 7.3 Solidification cracking behavior according to multi-beam welding

Fig. 7.2 shows the bead surface images after the multi-beam welding of the U-type hot cracking test according to welding speed (stress condition: 13kN). In the conventional GTAW, cracking was observed (bead location: 35mm). The weld bead size was constant under the condition of the distance between the heat sources of 5 mm and the laser power of 0.5 kW, but the width of the weld beads increased under the conditions of 0.8 kW. Also, as the laser power increased, the length of the cracking increased. However, in the condition of the distance between the heat sources of 15 mm, as the laser power increased, the size of the weld bead was constant and the cracking was suppressed. Under the condition of 0.8 kW the cracking was prevented.

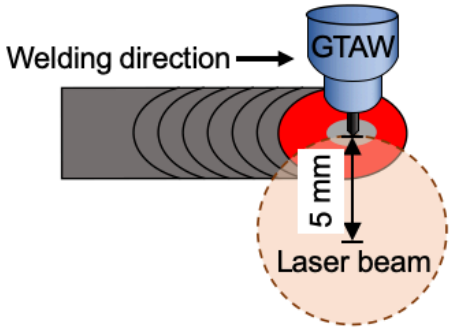
The fracture surfaces of the GTAW and multi-beam welding samples were observed via SEM (Fig. 7.3 (a-d)). Fig. 7.3 shows the fracture microstructure according to welding condition. The fracture surface was divided into Regions a-h. These regions were observed from the magnified SEM images (enlarged Regions a-h). As can be seen from all images, dendrite structures were observed on the fracture surface, which confirms the occurrence of solidification cracking.

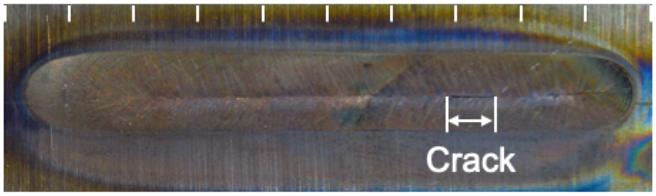
GTAW



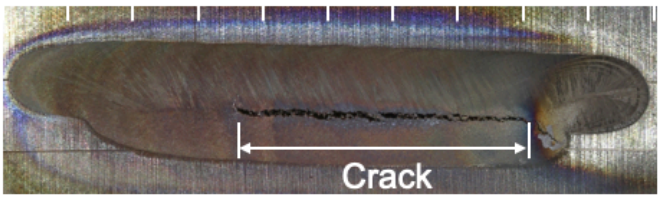

(a) GTAW

Multi-beam welding

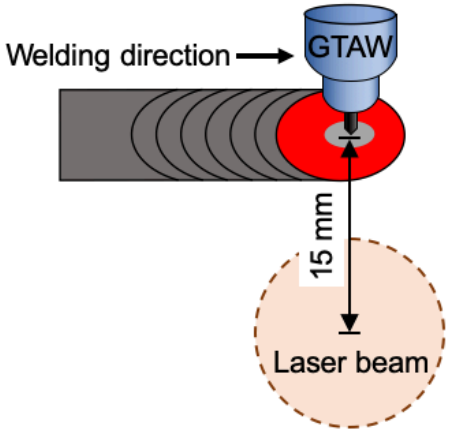


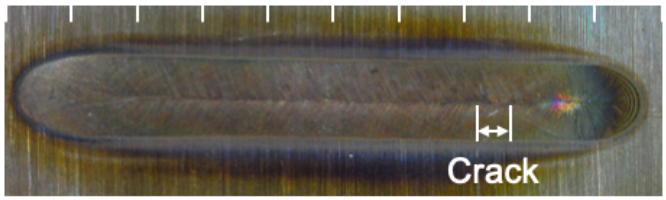




(b) Distance: 5 mm, laser power: 0.5 kW

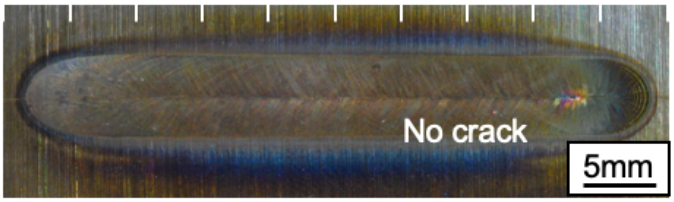



(c) Distance: 5 mm, laser power: 0.8 kW



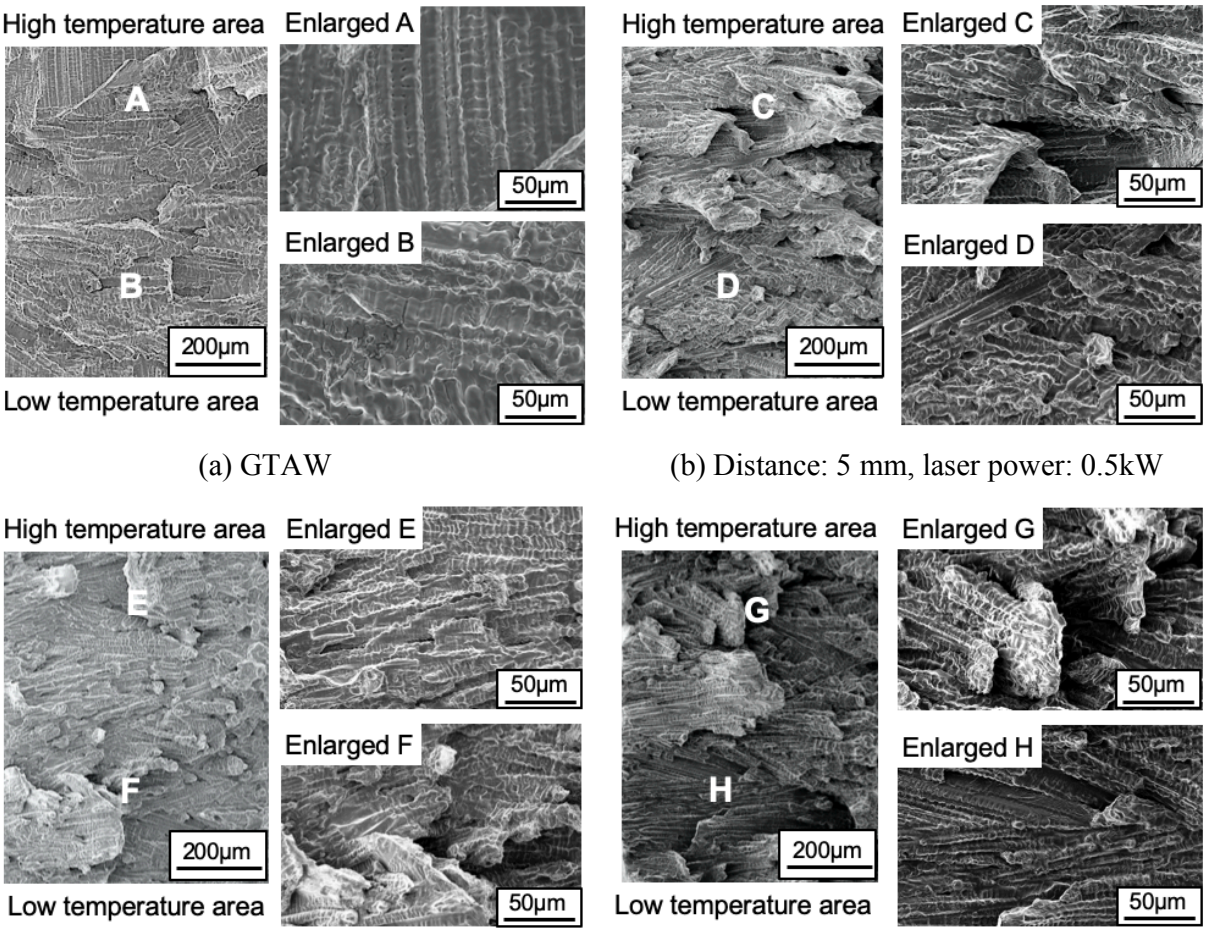




(d) Distance: 15 mm, laser power: 0.5 kW




(e) Distance: 15 mm, laser power: 0.8 kW

Fig. 7.2 The bead surface after U-type hot cracking test during multi-beam welding.




(a) GTAW (b) Distance: 5 mm, laser power: 0.5kW

(c) Distance: 5 mm, laser power: 0.8kW (d) Distance: 15 mm, laser power: 0.5kW

Fig. 7.3 SEM images of fracture surface after U-type hot cracking test.

## 7.4 Thermal strain calculation using finite element method

### 7.4.1 Finite element model

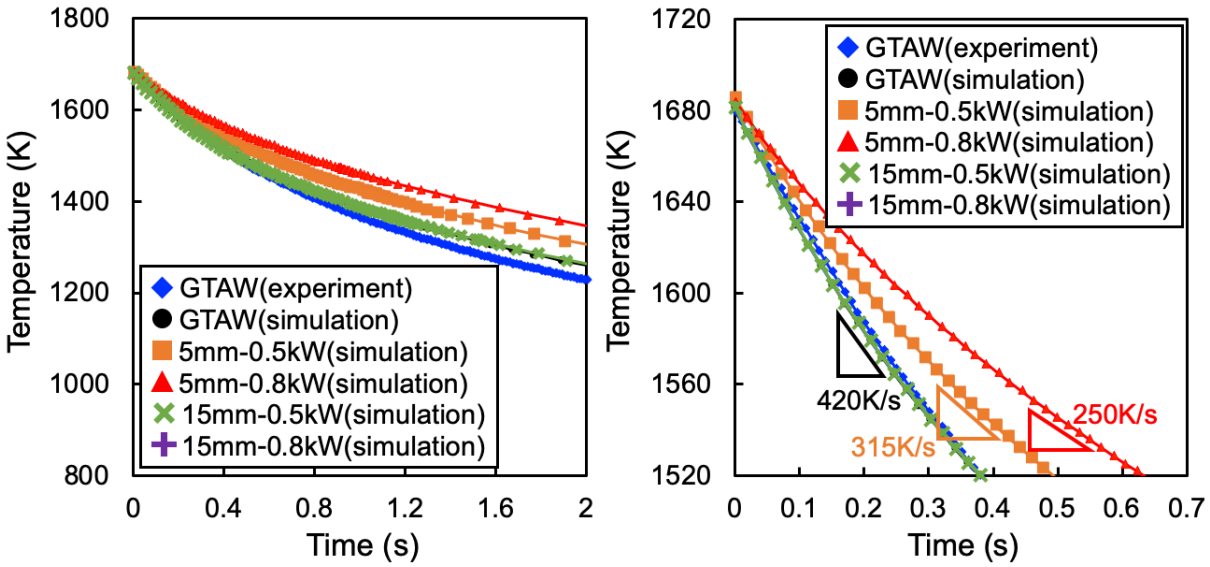
The finite element method for the multi-beam welding during the U-type hot cracking test was designed by Quick welder software. Exploiting the symmetrical welding, half of the workpiece was simulated to decrease the simulation time in the finite-element model to decrease the calculation time of the finite element method (Fig. 3.4). In the U-type hot cracking test, In the U-type hot cracking test, the bent restraint beam applied tensile stress to the specimen. The bent restraint beam was restored, due to the specimen expansion during the welding. Therefore the tensile stress loaded on the specimen decreased. The restraint beam was included in the model to reproduce this phenomenon. The material constants used in this model is same as the Fig. 3.5.

### 7.4.2 Comparison of weld bead shape and temperature history between experiment and simulation

The weld bead geometries according to welding conditions calculated by means of simulations were compared with the experiment results (Table 7.3). The calculated geometry of the fusion zone was determined based on the melting temperature (1680 K) of 310S stainless steel. The bead sizes

from the simulation and experimental results were in good agreement, with an error of less than 10%.

Fig. 7.4 shows the temperature history comparison between experimental results and calculated results. The cooling rate was measured by inserting a thermocouple into the molten pool during welding. The thermal strain measurement explains in the chapter of 3.5. The experimental and simulation results were in good agreement. Thus, the finite-element model for GTAW were verified based on the comparison of the experimental and simulation results. The temperature history of multi-beam welding conditions were replaced by the simulation result (Fig. 7.4).




(a) Temperature range: 1800 – 1000 K (b) Temperature range: 1680 – 1520 K

Fig. 7.4 Time dependent temperature profiles according to welding speed condition and temperature history in the solid-liquid co-existence range.

Table 7.3 Comparison of the experimental and simulation results.

| Distance between heat sources | Welding process | Width of weld bead (mm) | | Depth of weld bead (mm) | |
|---|---|---|---|---|---|
| | | Experiment | Simulation | Experiment | Simulation |
| - | GTAW | 5.14 | 5.11 | 0.99 | 1.04 |
| 5 mm | 0.5 kW | 5.19 | 5.11 | 1.10 | 1.04 |
| | 0.8 kW | 5.20 | 5.11 | 1.03 | 1.04 |
| 15 mm | 0.5 kW | 5.40 | 5.33 | 1.20 | 1.23 |
| | 0.8 kW | 7.32 | 7.34 | 1.30 | 1.35 |

## 7.5 Theoretical approach to solidification cracking susceptibility

The BTR is characterized by the solidification initiation/completion temperature. In the study, each temperature was calculated based on the theoretical analysis model instead of the experimental result. Fig. 7.4 shows the cooling rate of the weld bead according to the welding conditions. In the GTAW case, the simulated and experimental cooling rate results show a close correspondence. Therefore, the cooling rate of the multi-beam was replaced by the simulation results. The simulated cooling rates in the multi-beam welding distance condition of 15 mm also demonstrate the same temperature history as in the case of GTAW. Therefore, we concluded that the BTR was consistent according to the welding conditions. However, in distance condition of 5 mm, the cooling rate was decreased by increasing the laser beam power. The BTR was expected to change due to the difference in cooling rate. The solidification initiation/completion temperatures were modeled by means of the supercooling and solidification segregation models, respectively. In this chapter, the BTR according to welding conditions was calculated by metallurgical analysis method explained in Chapter 3.6. Table 7.4 shows conditions for numerical calculations. The cooling rate for each condition was measured in Fig. 7.4 (b).

Table 7.4 Conditions for numerical calculations.

| | | | | |
|---|---|---|---|---|
| Dendrite radius (μm) | 10 | | | |
| Number of mesh division | 100 | | | |
| Solidification rate (mm/s) | 5 | | | |
| Distance between heat sources (mm) | 5 | | 15 | |
| Laser power (kW) | 0.5 | 0.8 | 0.5 | 0.8 |
| Cooling rate (K/s) | 315 | 250 | 420 | 420 |

*Cooling rate in GTAW: 420K/s

The solidification initiation temperature was 1680K in all welding conditions. There is no effect of the supercooling degree on the solidification initiation temperature change according to the welding speed. Fig. 7.5 shows the amount of segregation concentration in residual liquid during solidification using solidification segregation model. Fig. 7.5 shows a comparison of segregation amounts of low-melting-point elements P, C and S according to welding condition.

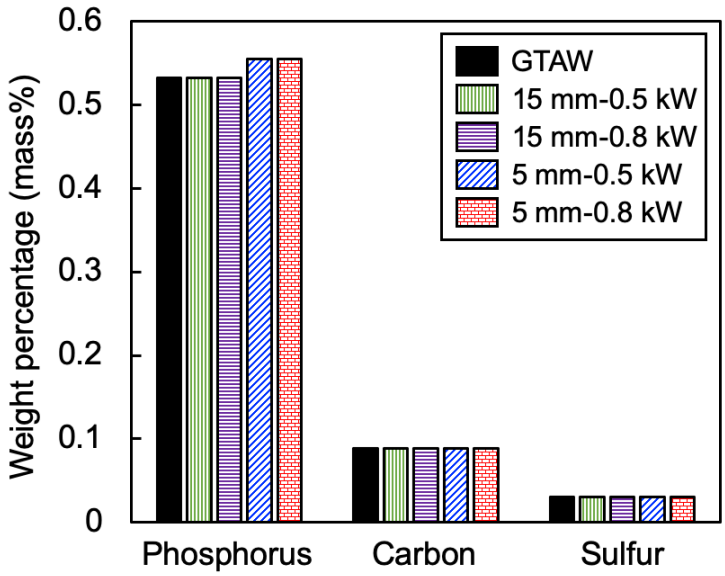



Fig. 7.5 Solidification segregation concentration according to welding conditions.

Under GTAW conditions, the solidification completion temperature was 1520K. In the distance condition of 15 mm solidification completion temperature was 1520 K regardless of laser power increase due to the constant cooling rate. According to the laser power in the distance condition of 5 mm, the segregation of P was promoted and segregation of C and S were also slightly promoted. Table 7.5 shows the BTR according to welding conditions. The BTR was slightly increased as the laser power increased in the distance condition of 5 mm. The laser power increase did not significantly affect the solidification cracking susceptibility.

Table 7.5 BTR according to welding conditions.

| Distance between heat sources (mm) | 5 | | 15 | |
|---|---|---|---|---|
| Laser power (kW) | 0.5 | 0.8 | 0.5 | 0.8 |
| BTR (K) | 164 | 164 | 160 | 160 |

*BTR in GTAW: 160 K

### 7.6 Evaluation of solidification cracking susceptibility in multi-beam welding

A solidification initiation temperature and completion temperature, in addition to the critical strain are required for the hot ductility curve. Fig. 7.6 shows the hot ductility curve according to welding conditions.

The solidification initiation temperature and completion temperature viz; the BTR according to welding speed conditions were calculated by metallurgical analysis model (Table 7.4). In the distance between heat source of 5 mm, the segregation concentration of the residual liquid was constant with the GTAW. However, in the distance between heat source of 5 mm, the segregation concentration of the residual liquid phase was slightly increased as the laser power increased, and the BTR was also slightly increased. The critical strain was constant according to the cooling rate

change of the weld bead (Fig. 4.10). Therefore, the critical strain was employed from the results of GTAW (Fig. 3.10). The *x*-axis in Fig. 3.10 was converted from time to temperature using the temperature history (Fig. 3.7) and all critical strain were combined. Fig. 7.6 shows the hot ductility curves according to welding conditions (BTR: 160-164 K). There was no significant difference in solidification susceptibility according to the welding process. This implies that the change in the hot ductility curve does not significantly cause an increase in solidification cracking.

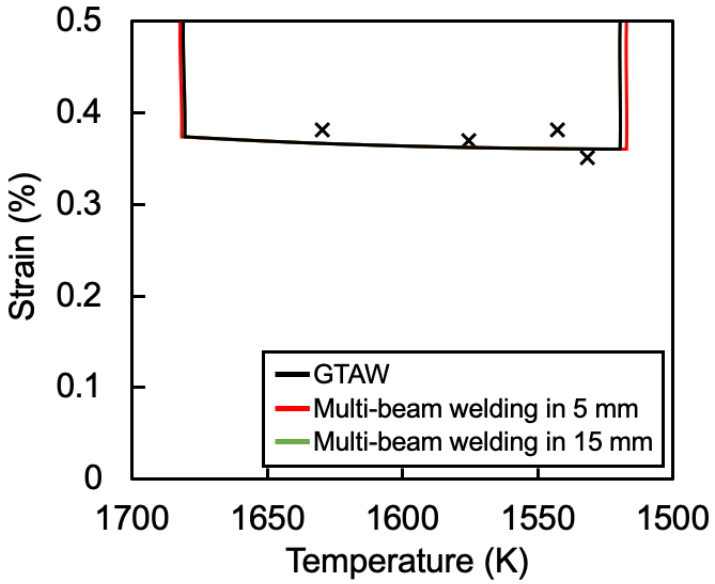
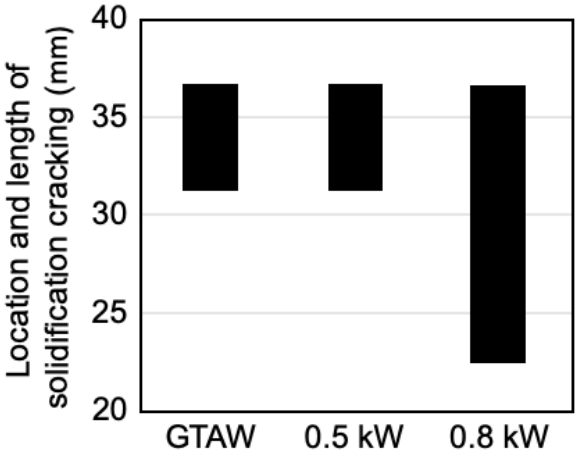


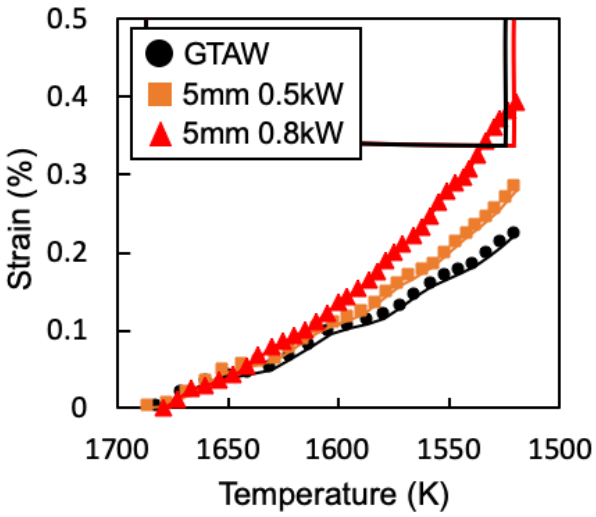

Fig. 7.6 Hot ductility curves according to welding conditions.

### 7.7 Influence of multi-beam welding on solidification cracking behavior

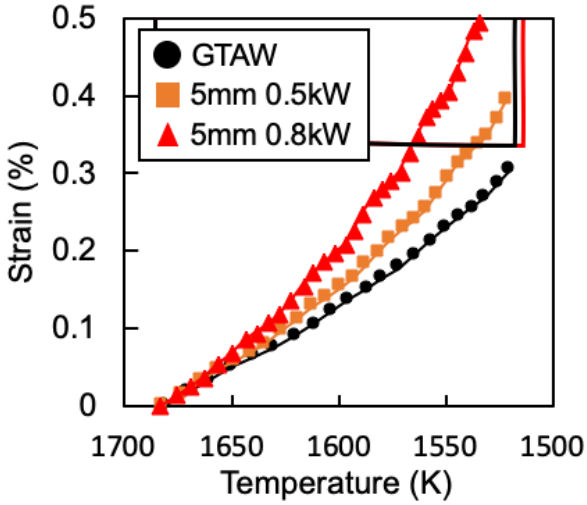
Solidification cracking occurrence (Fig. 7.2) can be explained by relationship between hot ductility and thermal strains. Fig. 7.7 shows thermal strain and hot ductility curve under the distance condition of 5 mm according to bead location (Fig. 7.7(b-d)), in addition to solidification cracking behavior (Fig. 7.7(a)).



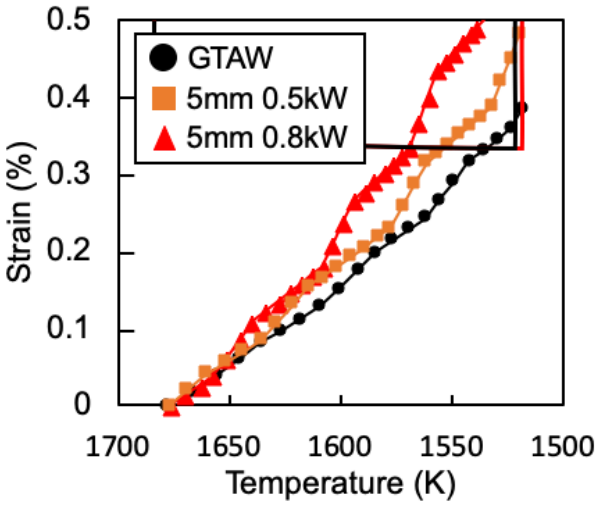

(a) Solidification cracking behavior




(b) Bead location: 25 mm




(c) Bead location: 30 mm



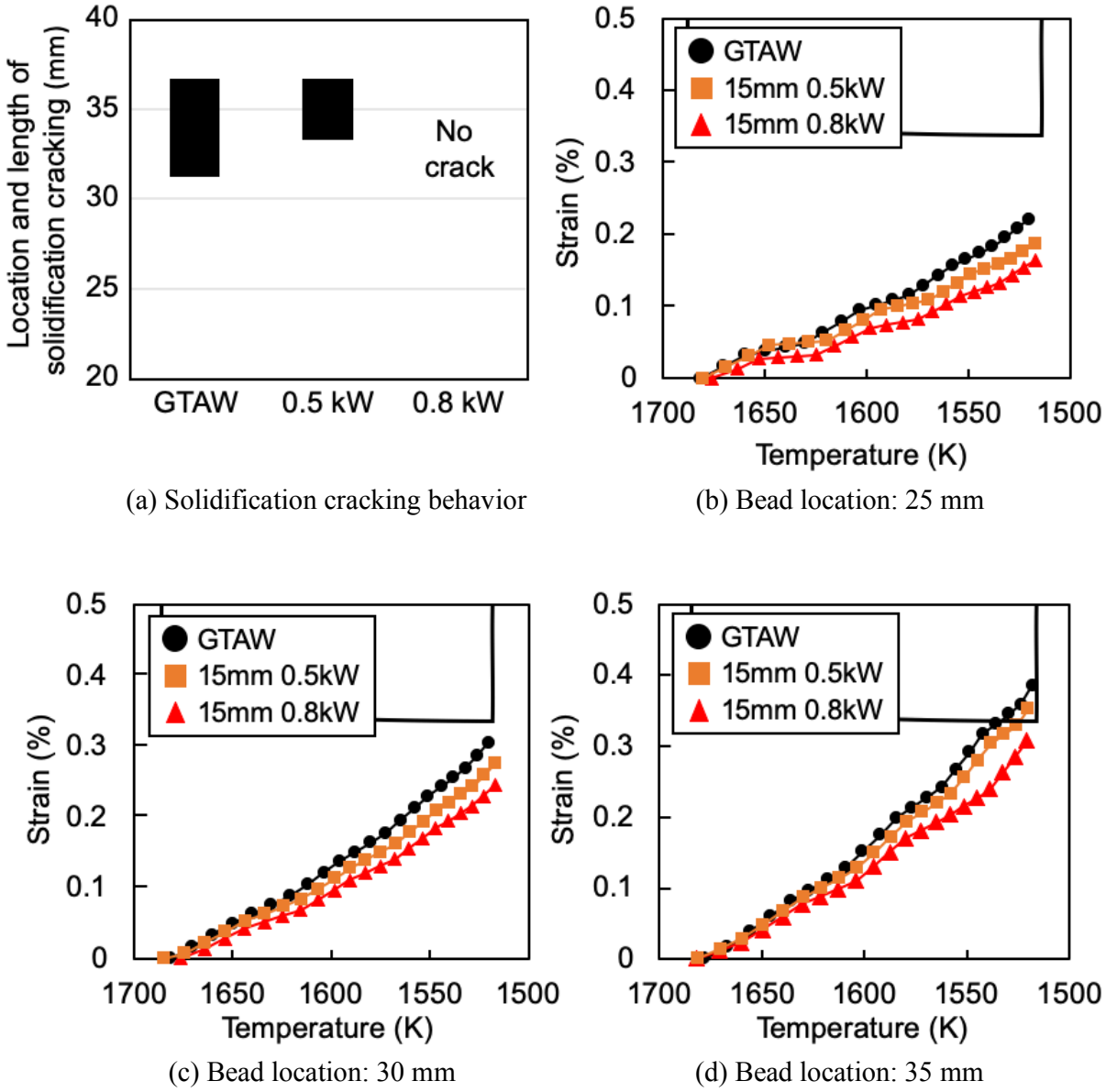

(d) Bead location: 35 mm

Fig. 7.7 Evaluation of solidification cracking behavior according to welding condition Hot ductility curve and thermal strain comparison (GTAW-laser distance: 5 mm).

The thermal strains were derived from the finite element analysis results under a stress level of 13 kN in the U-type hot cracking test. In the 0.8 kW welding condition, the thermal strain intersected with the hot ductility curve at the 25-35 mm bead location, so the longest solidification cracking was observed. Under the 0.5 kW welding conditions, the thermal strains intersected at the 30 and

35 mm bead location and in the GTAW, the intersection was observed at the 35 mm. The slope of the thermal strain was significantly increased with increasing laser power at 5 mm distance between the heat sources. Therefore, the behavior of the solidification cracking is greatly influenced by the behavior of the thermal strain, not the hot ductility curve.

Fig. 7.8 shows thermal strain and hot ductility curve under the distance condition of 15 mm according to bead location (Fig. 7.8(b-d)), in addition to solidification cracking behavior (Fig. 7.8(a)).




(a) Solidification cracking behavior

(b) Bead location: 25 mm

(c) Bead location: 30 mm

(d) Bead location: 35 mm

Fig. 7.8 Evaluation of solidification cracking behavior according to welding condition Hot ductility curve and thermal strain comparison (GTAW-laser distance: 15 mm).

Unlike the results in the 5mm distance between heat sources, the 15mm condition showed that the thermal strain was decreased with increasing laser power. At the laser power of 0.5 kW, the slope of the thermal strain was decreased when compared to GTAW, but at the 35 mm bead location, the intersection with the hot ductility curve was continued and the solidification cracking occurred.

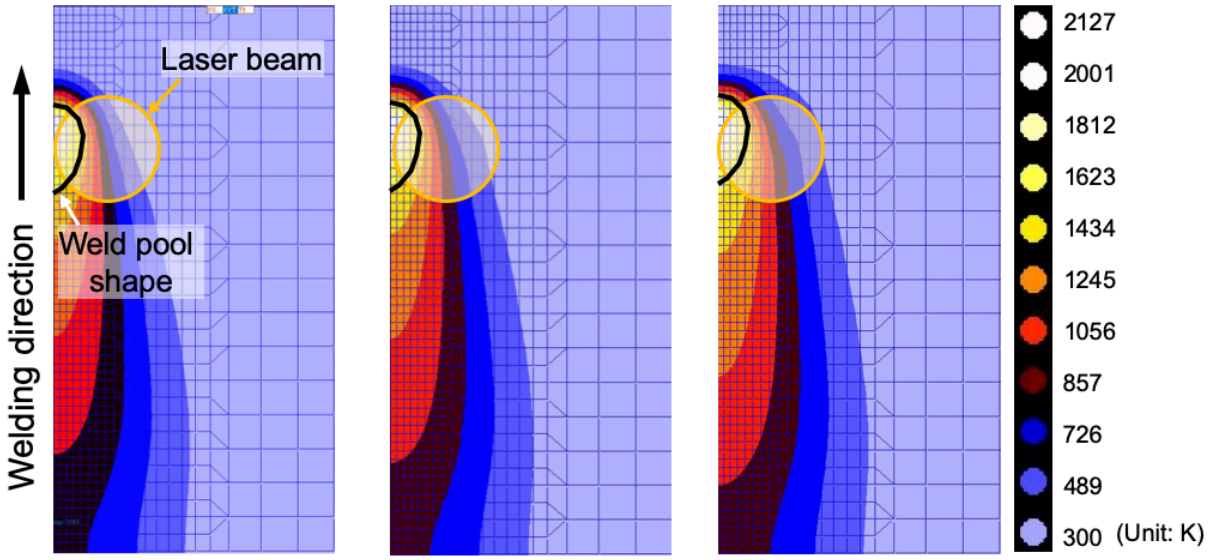
However, at the condition of 0.8 kW, the thermal strain slope was further decreased and intersection between these two curves was confirmed at any bead location.

It was found that the behavior of solidification cracking during multi-beam welding was affected by the distance between the heat sources and the laser power. The effect of the distance between heat source and laser power on the thermal strain behavior was investigated using the finite element method.

## 7.8 Controlling of thermal strain behavior in multi-beam welding

### 7.8.1 Controlled by overlapped heat sources in multi-beam welding

The temperature distribution was calculated using the finite element method in order to observe the high temperature cracking behavior at a distance of 5 mm between the heat sources. Fig. 7.9 shows the temperature distribution according to welding condition. Since the diameter of the laser beam is 10 mm, the laser beam overlaps the arc. Therefore, as the laser power increased, the width of the weld bead and the heat-affected zone was increased.




(a) GTAW (b) Distance: 5 mm Laser power: 0.5 kW (c) Distance: 5 mm Laser power: 0.8 kW

Fig. 7.9 Temperature field according to welding condition calculated by finite element method.

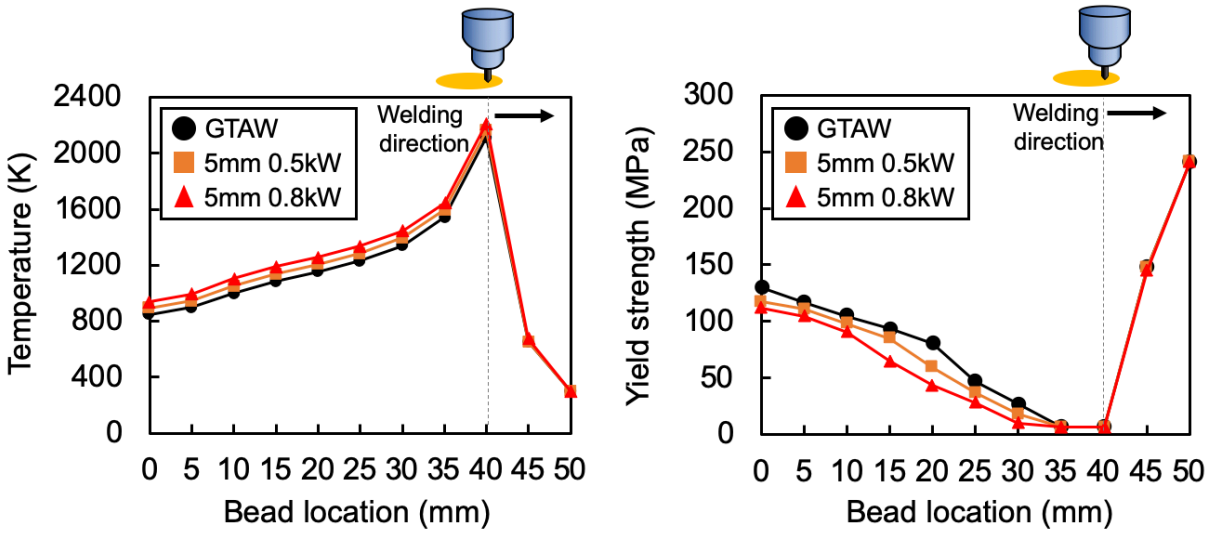
Table 7.6 Length of solid-liquid co-existence zone.

| Distance between heat sources (mm) | 5 | |
|---|---|---|
| Laser power (kW) | 0.5 | 0.8 |
| Solid-liquid co-existence zone (mm) | 2.4 | 3.1 |

*Solid-liquid co-existence zone in GTWA: 2.3 mm

The solid-liquid co-existence zone was measured using the temperature history employed by the finite element method (Fig. 7.4). Table 7.6 shows solid-liquid co-existence zone according to welding conditions. The increase in laser power increased the solid-liquid co-existence zone.

Fig. 7.10(a) and (b) shows the temperature and yield strength distribution calculated by the finite element simulation method according to the bead location when the heat source passes through an arbitrary location (40 mm). The increase in laser power under the conditions of overlapping two heat sources shows the effect of increasing the amount of heat input on the weld bead. Therefore, as the laser power which is overlapped with the arc increased, the amount of heat input of the weld bead was increased. As a result, the temperature distribution of the weld beads was higher, and the distribution of yield strength was decreased. Therefore, the increase of laser power in the condition where the two heat sources overlap, makes the welding bead vulnerable to plastic deformation.




(a) Temperature distribution (b) Yield strength distribution

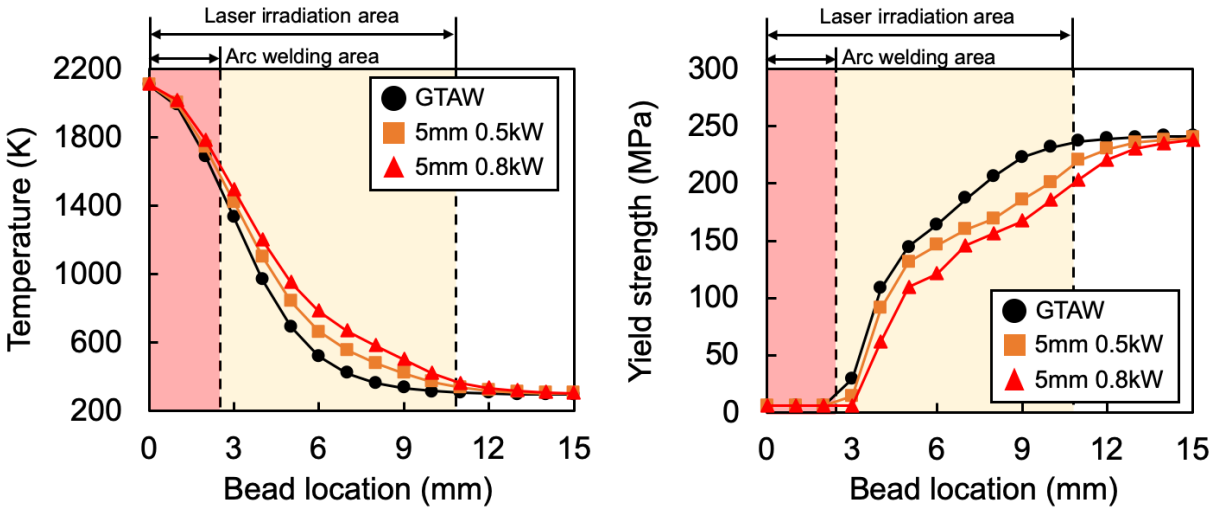
Fig. 7.10 Temperature and yield strength distribution calculated by finite element method.

The effect of the heat-affected zone by laser beam irradiation parallel to GTAW on the solidification cracking behavior was investigated. Fig. 7.11 shows the temperature distribution and yield strength distribution along the transverse welding direction. As the laser power increased, the temperature distribution of the base material was increased. Therefore, the yield strength was decreased with increasing temperature. The decrease in yield strength of the heat-affected zone affected the expansion due to tensile stress during the U-type hot cracking test.

In order to investigate the effect of the temperature distribution and yield strength distribution of the heat-affected zone on the thermal strain, strain changes over time were compared. Fig. 7.12 shows the calculation results of strain over time in the center of the heat-affected zone (location: 6 mm in *x*-axis direction) using the finite element method. The yield strength affected the amount of deformation in heat-affected zone.

The increase in the amount of expansion of the heat-affected zone due to the increase in the amount of heat input expects to relieve the stress on the weld during the U-type hot cracking test. Fig. 7.13 shows the stress loaded on the weld bead calculated by the finite element method during solidification according to the multi-beam welding conditions. As the laser power increased, the amount of expansion of the heat-affected zone was increased. Therefore, the stress on the weld was expected to decrease, but on the contrary, the stress was increased. This is because the effect of vulnerable to plastic deformation due to the increase in the heat input of the weld is more dominant

than the effect of releasing the stress of the weld bead due to the increase in the amount of expansion of the heat-affected zone.




(a) Temperature distribution (b) Yield strength distribution

Fig. 7.11 Temperature and yield strength distribution calculated by finite-element model according to transverse location.

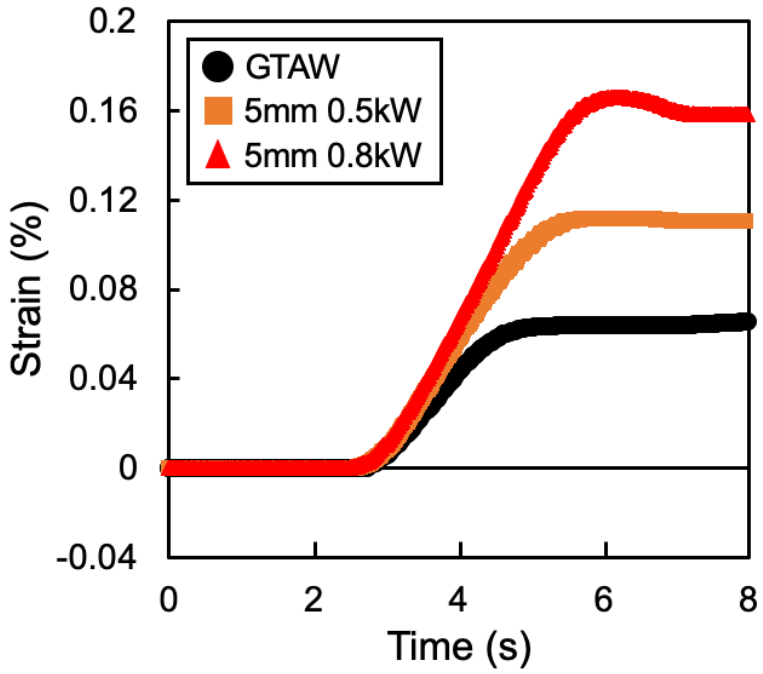



Fig. 7.12 Strain rate in the center of HAZ (location: 6 mm in *x*-axis direction) according to welding time (Distance between heat sources: 5 mm).

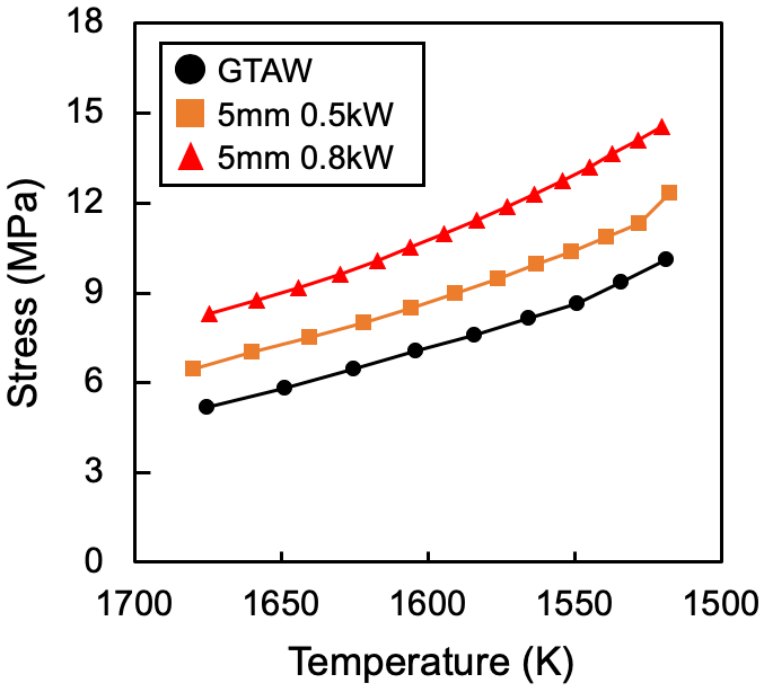
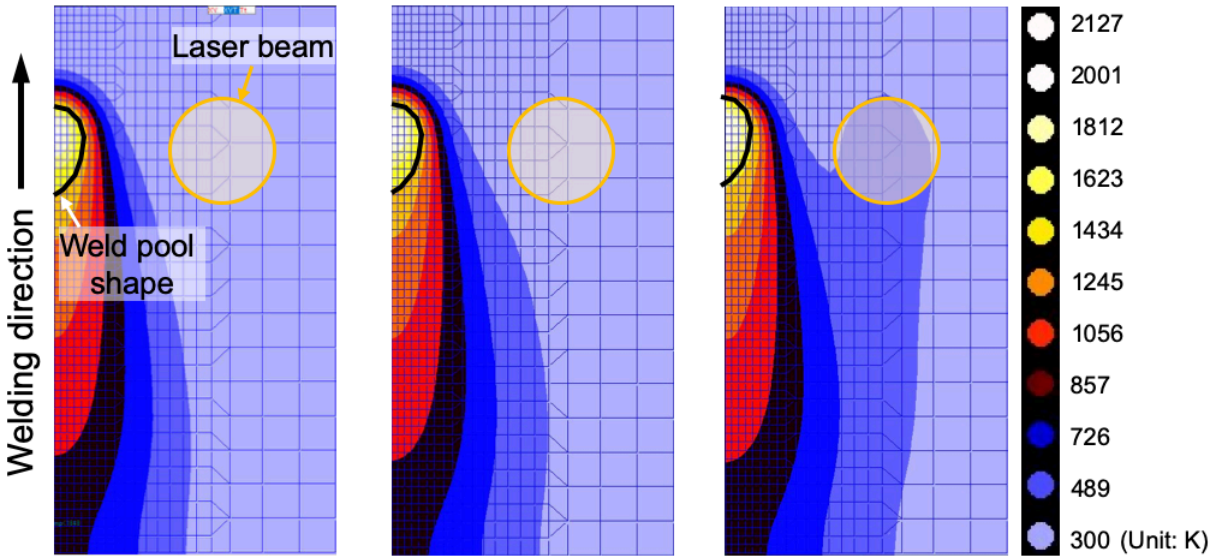



Fig. 7.13 Stress loaded on the weld bead during the solidification (Distance between heat sources: 5 mm).

### 7.8.2 Controlled by non-overlapped heat sources in multi-beam welding

The temperature distribution was calculated using the finite element method in order to observe the high temperature cracking behavior at a distance of 15 mm between the heat sources. Fig. 7.14 shows the temperature distribution according to welding condition. In the 15mm distance condition, the weld bead size was constant despite the increase of laser power.




(a) GTAW (b) Distance: 15 mm Laser power: 0.5 kW (c) Distance: 15 mm Laser power: 0.8 kW

Fig.7.14 Temperature field according to welding condition calculated by finite element method.

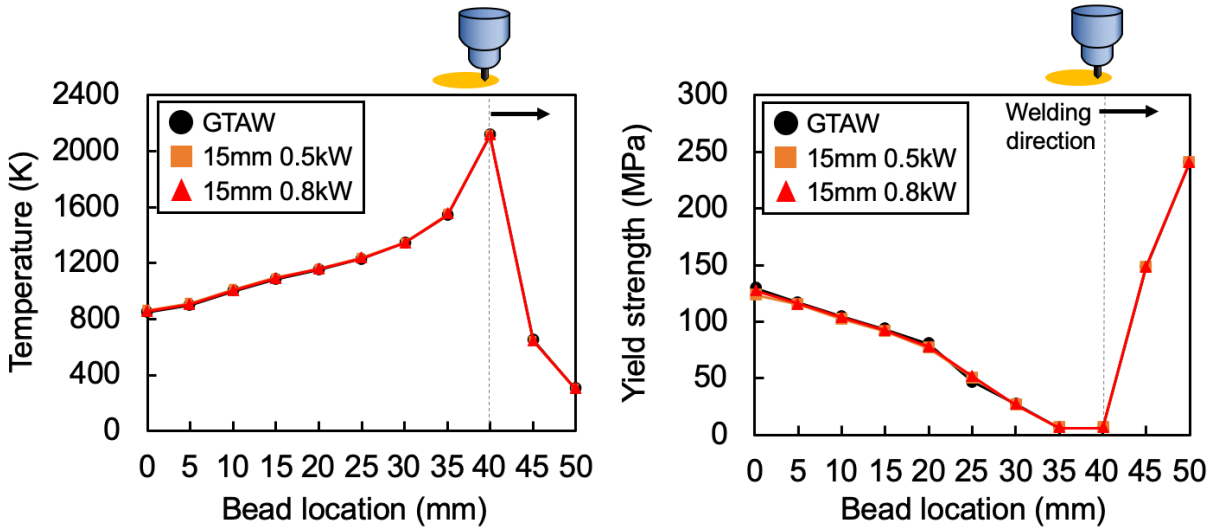
The solid-liquid co-existence zone was measured using the temperature history employed by the finite element method (Fig. 7.4). Table 7.7 shows solid-liquid co-existence zone according to welding conditions.

Table 7.7 Length of solid-liquid co-existence zone.

| Distance between heat sources (mm) | 15 | |
|---|---|---|
| Laser power (kW) | 0.5 | 0.8 |
| Solid-liquid co-existence zone (mm) | 2.3 | 2.3 |

*Solid-liquid co-existence zone in GTWA: 2.3 mm

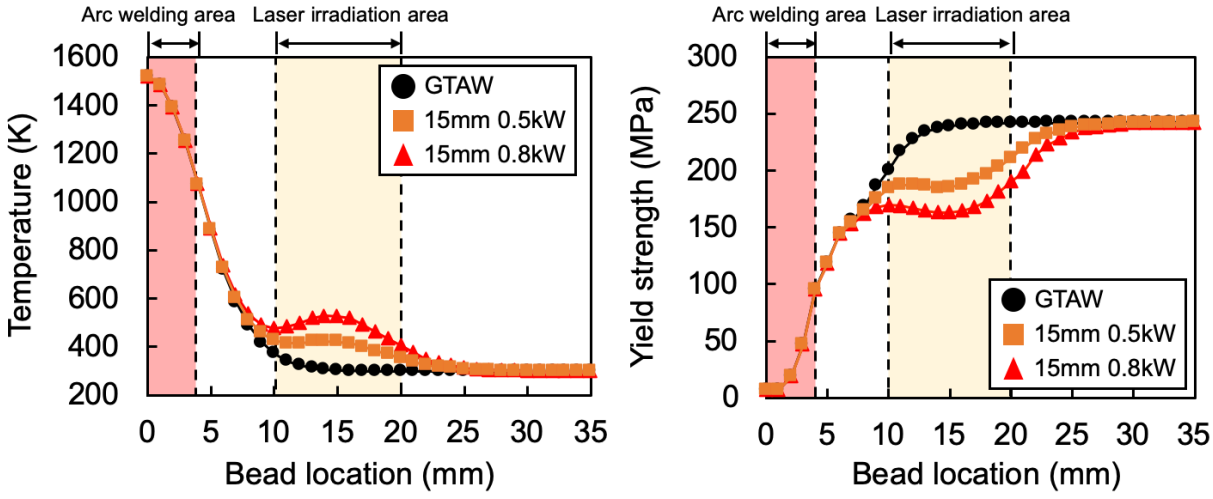
There was no difference in the temperature history curve and the solid-liquid coexistence zone. The increase in laser power under the distance of 15mm conditions did not affect on the weld bead. Fig. 7.15(a) and (b) shows the temperature and yield strength distribution calculated by the finite element simulation method according to the bead location when the heat source passes through an arbitrary location (40 mm). In the distance of 15mm condition where the heat sources did not overlap, even if the laser power was increased, the temperature distribution of the weld was not affected. Therefore, the yield strength distribution was also constant regardless of the increase in laser power.




(a) Temperature distribution (b) Yield strength distribution

Fig. 7.15 Temperature and yield strength distribution calculated by finite element method.

The effect of the heat-affected zone by laser beam irradiation parallel to GTAW on the solidification cracking behavior was investigated. Fig. 7.16 shows the temperature distribution and yield strength distribution along the transverse welding direction. As the laser power increased, the temperature distribution of the base material was increased (8-24 mm). Therefore, the yield strength was decreased with increasing temperature. A decrease in yield strength of the heat-affected zone affected the expansion due to tensile stress during the U-type hot cracking test.




(a) Temperature distribution (b) Yield strength distribution

Fig. 7.16 Temperature and yield strength distribution calculated by finite-element model according to transverse location.

Ploshiken et al. [126] reported solidification cracking prevention via additional laser beam. However, there was no explanation for the effect of laser-beam-irradiated area on the solidification cracking prevention. Therefore, in this study, the role of the laser beam for the cracking suppression was discussed. In order to investigate the effect of the temperature distribution and yield strength distribution of the heat-affected zone on the thermal strain, strain changes over time were compared. Fig. 7.17 shows the calculation results of strain over time in the center of the heat-affected zone (location: 6 mm in x-axis direction) using the finite element method.

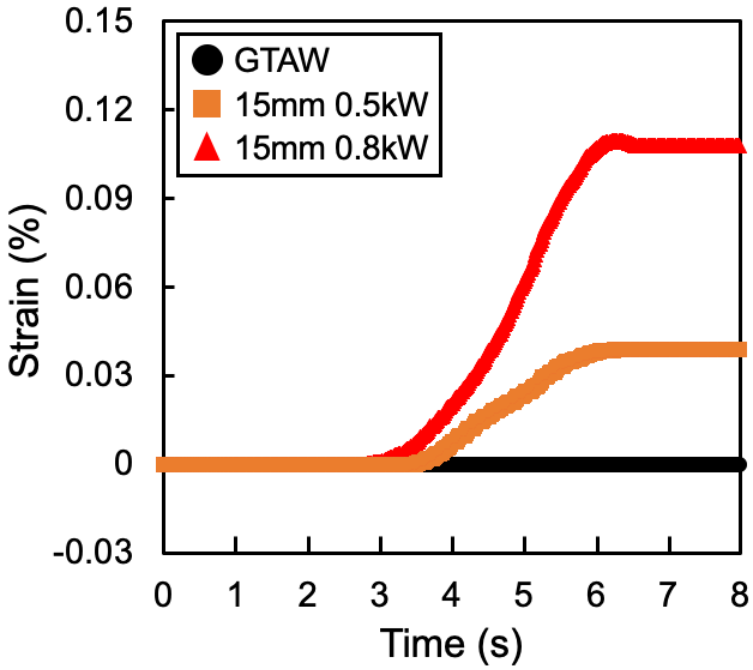



Fig. 7.17 Strain rate in the center of HAZ (location: 6 mm in x-axis direction) according to welding time (Distance between heat sources: 15 mm).

We note that there is no strain change in the GTAW specimen. However, as the laser power increases, the amount of expansion of the specimen increases because of the yield-strength reduction. Next, we used the Quick Welder software to calculate the load stress on the weld bead during solidification. Fig. 7.18 shows the load stress at the same weld bead location where the cracks occurred in Fig. 7.2 (c, d). In the case of GTAW, the largest stress is applied to the weld bead, and it decreased with increasing laser power. The tensile stress applied to the weld bead is decreased with the expansion of the specimen, and the magnitude of the thermal strain is also decreased, thereby resulting in the prevention of solidification cracking.

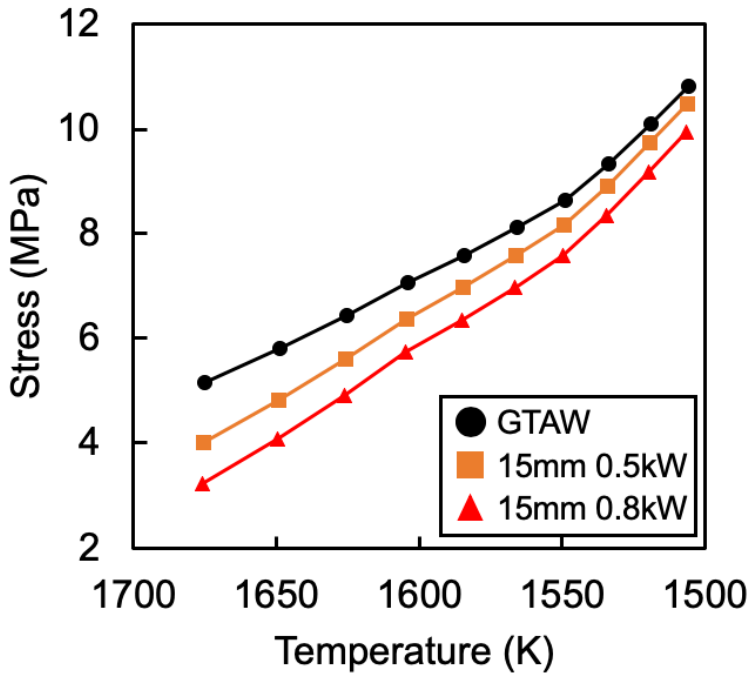
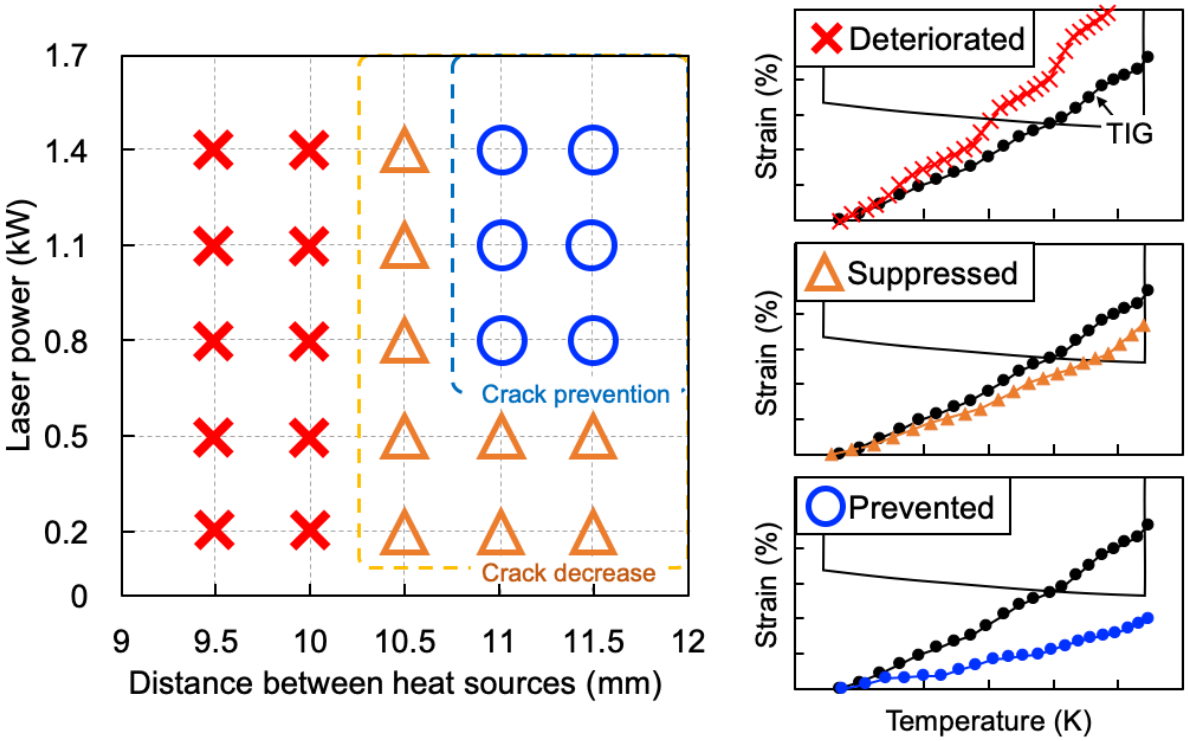



Fig. 7.18 Stress loaded on the weld bead during the solidification (Distance between heat sources: 15 mm).

### 7.9 Optimization of multi-beam welding condition for solidification cracking prevention

Fig. 7.19 shows the solidification cracking behavior according to the distance between the heat sources and the laser power. The thermal strain and hot ductility curve of each condition were compared. When the distance between the two heat sources was below 10 mm, the yield strength of the weld bead was reduced due to the increase of heat input of the weld bead. As a result, it made vulnerable to the solidification cracking. However, at the distance of 10.5 mm or more, the amount of expansion of the base material was increased without affecting the temperature and yield strength distribution of the welding bead even when the laser power was increased. During the U-type hot cracking test, an increase in the amount of expansion due to irradiation of the laser beam relieved the stress loaded on the weld bead, therefore, it is possible to suppress and prevent the solidification cracking.




(a) Solidification cracking suppression area according to welding condition

(b) Solidification cracking behavior according to thermal strain

Fig. 7.19 Solidification cracking behavior according to multi-beam welding condition.

### 7.10 Summary

In the Chapter 6, the solidification cracking was suppressed due to the stress relief of weld bead due to the increase in the amount of expansion of the heat-affected zone. In order to apply this principle, the laser beam was irradiated to the base material in this chapter. The solidification cracking behavior was observed according to the distance between the heat sources and the laser power prior to suggest optimal multi-beam welding conditions. The hot ductility curve and the thermal strain according to each welding condition were calculated. The optimal multi-beam welding conditions were proposed using the finite element method.

The summarized conclusions are as follows;

1) In order to estimate the conditions for solidification cracking prevention, we calculated the hot ductility curve and thermal strain for three different welding conditions. The hot ductility curve was plotted as the variation in the critical strain as a function of the solidification initiation/completion temperatures. Thermal strain was calculated by means of the finite-element simulation model.

2) When the heat source overlapped, the solidification cracking increased due to the increase of the thermal strain. Stress relief was expected due to an increase in the amount of expansion

of the heat-affected zone, but the influence of the reduction in yield strength of the weld bead prevailed, making it vulnerable to solidification cracking.

3) In the condition of laser beam did not affect the temperature distribution of the weld bead, the thermal strain was reduced. The increase in the amount of expansion of the heat-affected zone due to the increase in the laser power, the stress applied to the weld was alleviated resulting in preventing solidification cracking.

4) In order for the solidification cracking to be suppressed the following conditions are required. A sufficient distance between the heat sources is required for the constant weld bead temperature distribution. A sufficient laser power for expansion of base metal which required for stress relief in weld bead.

# Chapter 8 Conclusions

The purpose of this study is to control the thermal strain to prevent solidification cracking that occurs during GTAW of austenitic stainless steel. In order to evaluate the solidification cracking from the thermomechanical point of view, the hot ductility curve and the thermal strain was calculated. Based on these two curves, the solidification cracking behavior according to various welding processes was described. We propose a optimize welding process that prevents solidification cracking via the reduction of the thermal strain of the weld bead.

The first chapter is an introductory part, describing the purpose and flow of the study.

In the Chapter 2, the characteristics and applications of austenitic stainless steels was described. In addition, the solidification cracking problems arising during the welding of stainless steel and the limitations of solutions were described, and at the same time, the evaluation of solidification cracking susceptibility was summarized.

In the Chapter 3, the solidification cracking prediction model was designed to predict the solidification cracking that occurs during U-type hot cracking tests in GTAW of 310S stainless steel. A solidification cracking occurrence during the U-Type hot cracking test in the GTAW was observed through the relationship between the hot ductility curve and thermal strain.

1. The hot ductility curve was obtained based on a combination of the solidification initiation and completion temperatures, in addition to the critical strain rate. Solidification initiation and completion temperatures were calculated by metallurgical analysis model; viz. KGT model (supercooling) and solidification segregation model, respectively.
2. The thermal strains were calculated using the finite element model. The finite element method verified the identical results with the experimental results with respect to the weld bead morphology, temperature history and strain-time curve.
3. The intersection between the hot ductility curve and the thermal strains increased with an increase in the loaded stress. In the actual test, solidification cracking did not occur under the conditions of 12 kN, but the cracks elongated according to the loaded stress. The solidification cracking occurrence in the actual test corresponded with the prediction results.

In the Chapter 4, the laser beam was irradiated behind the molten pool to observe the solidification cracking behavior during the U-type hot cracking test of GTAW. Irradiation of the laser beam of the molten pool increased the solidification cracking than the GTAW. The effect of the change in the solid-liquid coexistence zone of the molten pool on the solidification cracking by changing the laser power, the distance between the heat sources, and the laser spot size was analyzed using the solidification cracking prediction model. The hot ductility curve according to each welding condition was calculated and compared with the thermal strain calculated by the finite element method to compare the solidification cracking behavior.

1. The critical strain according to the laser power change was compared using the in-situ observation method. The cooling rate was changed according to the laser power, but the critical

strain was constant. Therefore, the critical strain of the hot ductility curve was used as the result of GTAW.

2. Solidification initiation and completion temperatures according to welding conditions were calculated through metallurgical analysis. Cooling rate decreased with increasing laser beam power. A decrease in cooling rate increased the solidification initiation temperature. The solidification completion temperature decreased due to an increase in the amount of segregation concentration of the residual liquid. Therefore, the BTR increased with increasing laser power. As the distance change between heat sources increased, the cooling rate decreased and BTR increased. The BTR was constant because there was no change in the cooling rate under the laser spot size change condition. The BTR slightly increased by the laser in-situ post heating process. However, solidification cracking susceptibility did not significantly changed enough to affect the solidification cracking behavior.
3. The slope of thermal strain increased with the increase of the laser power and the solidification cracking increased with an increase in the intersections with the hot ductility curve. As the distance between the heat sources increased, the thermal strain increased, and the solidification cracking increased. The change in the size of the laser beam has no significant effect on the slope of the thermal strain.
4. Increasing the laser power and the distance between heat sources increased the solid-liquid coexistence area and increased the temperature distribution of the weld beads. Therefore, the distribution of yield strength of the welded bead decreased, making it vulnerable to plastic deformation, and the length of solidification cracking increased. Since there was no change in the solid-liquid coexistence area under the laser spot size change, the temperature distribution and yield strength distribution were constant, showing similar solidification cracking behavior.

In the Chapter 5, in order to suppress the solidification cracking, water was flowed on the opposite side of the specimen during GTAW during the U-type hot cracking test. In addition, the finite element method was used to predict the behavior of solidification cracking according to the conductivity change of coolant. The hot ductility curve and the thermal strain was calculated and compared to investigate the solidification cracking behavior. The mechanical properties of the weld bead were compared and analyzed using the finite element method to investigate the behavior of thermal strain.

1. In Chapter 4, From the fact that the critical strain was not affected by the cooling rate, the critical strain according to the cooling process was used as the value measured during GTAW.
2. Solidification initiation and completion temperatures were calculated by KGT model and solidification segregation model, respectively. The solidification initiation temperature was not changed. However, the segregation concentration of S, P and C in the residual liquid decreased with increasing cooling rate. Therefore, the solidification completion temperature increased. However, the BTR didn’t change enough to affect the solidification cracking behavior change.

3. The thermal strain was calculated using the finite element method. As the conductivity of the coolant increased, the thermal strain slope decreased and intersection between hot ductility curve didn't observed. As a result, the solidification cracking was prevented.
4. Increasing of the coolant conductivity increased the heat dissipation of the weld bead, resulting in increasing the cooling rate and decreasing the solid-liquid coexistence zone. Therefore, the temperature distribution of the weld beads decreased and the yield strength increased. Increasing yield strength suppressed plastic deformation and suppressed the solidification cracking.

In the Chapter 6, we investigated the optimization welding conditions for solidification cracking suppression. The arc current value was also adjusted to constant the size of the welding bead according to the welding speed. The increase in welding speed was vulnerable to the solidification cracking. The hot ductility curve and the thermal strain was calculated and compared to investigate the solidification cracking behavior. The mechanical properties of the weld bead were compared and analyzed using the finite element method to investigate the behavior of thermal strain.

1. Solidification initiation and completion temperatures were calculated by KGT model and solidification segregation model, respectively. The solidification initiation temperature was constant. The segregation concentration of S, P and C in the residual liquid slightly decreased with increasing welding speed. The BTR didn't significantly change. Therefore, the solidification cracking susceptibility change didn't significantly affected the solidification cracking behavior.
2. The thermal strain was calculated using the finite element method. As the welding speed increased, the slope of the thermal strain increased. As a result, intersection with the hot ductility curve increased, resulting in vulnerable solidification cracking.
3. The difference in the temperature distribution of the welding beads according to the welding conditions was not observed. However, the heat input increase due to the decrease in welding speed increased the temperature distribution of heat-affected zone resulting in vulnerable to plastic deformation.
4. Decreasing the welding speed increased the amount of heat-affected zone expansion as the yield strength of the heat-affected zone decreased. In addition, with the expansion of the heat-affected zone, stress was reduced on the weld bead, which suppressed the hot cracking process.

In the Chapter 7, the laser beam was irradiated to the base material in this chapter to apply the principle of Chapter 6. The solidification cracking behavior was observed according to the distance between the heat sources and the laser power prior to suggest optimal multi-beam welding conditions. The hot ductility curve and the thermal strain according to each welding condition were calculated. The optimal multi-beam welding conditions were proposed using the finite element method.

1. In order to estimate the conditions for solidification cracking prevention, we calculated the hot ductility curve and thermal strain for three different welding conditions. The hot ductility curve was plotted as the variation in the critical strain as a function of the solidification

initiation/completion temperatures. Thermal strain was calculated by means of the finite-element simulation model.

2. When the heat source overlapped, the solidification cracking increased due to an increase in the thermal strain. Stress relief was expected due to an increase in the amount of expansion of the heat-affected zone, but the influence of the reduction in yield strength of the weld bead prevailed, making it vulnerable to solidification cracking.
3. In the condition of laser beam did not affect the temperature distribution of the weld bead, the thermal strain was reduced. The increase in the amount of expansion of the heat-affected zone due to an increase in the laser power, the stress applied to the weld was alleviated resulting in preventing solidification cracking.
4. In order for the solidification cracking to be suppressed the following conditions were required. A sufficient distance between the heat sources was required for the constant weld bead temperature distribution. A sufficient laser power for expansion of base metal which required for stress relief in weld bead.

## ACKNOWLEDGMENTS

I would like to express my sincere gratitude to Professor Kazuyoshi Saida for his great guidance and insight throughout this study. I consider myself privileged to have worked with world-class welding process professional. He gave me support not only on my research, but also on my career, which has played an important role in both of my professional and personal development. I would also like to thank assistant professor Shotaro Yamashita for providing me essential comments and advices as the research and experiments proceeded.

I would like to thank examiners of my thesis Professor Hiroshige Inoue, Professor Masahito Mochizuki Associate Professor Tomo Ogura for providing me this opportunity to conduct important scientific research. I would like to thank associate professor Yu Lina for providing me this opportunity to conduct important scientific research. I would also like to appreciate my sincere gratitude for the guidance and encouragement of Professor Chung-Yun Kang of Materials Science and Engineering, Busan University, Republic of Korea.

I would like to thank the past members of my research group Mr. Yu Itasaka. He gave me so much help on the research and life of studying abroad. Moreover, I would like to thank all the past and present members of Saida Laboratory, in Division of Materials and Manufacturing Science, Osaka University, for their enthusiastic help to both of my study.

I want to ensure my gratitude to my family and friends, who were great support and encouragement during my studied at Osaka University.

## References


1. K.H. Lo, C.H. Shek, J.K.L. Lai, Recent developments in stainless steels, Mater. Sci. Eng. R Rep, (2009) 65, 39-104.
2. C.L. Lai, L.W. Tsay, C. Chen, Effect of microstructure on hydrogen embrittlement of various stainless steels, MAT SCI ENG A-STRUCT, (2013) 584, 14-20.
3. A. Mortezaie, M. Shamanian, An assessment of microstructure, mechanical properties and corrosion resistance of dissimial welds between Inconel 718 and 310S austenitic stainless steel, INT J PRES VES PIP, (2014) 37-46.
4. Y. Zhong, C. Zhou, S. Chen, R. Wang, Effect of temperature and pressure on stress corrosion cracking behavior of 310S stainless steel in chloride solution. CHIN J MECH ENG-EN., (2017) 30, 200-206.
5. A. Mortezaie, M. Shamanian, As assessment of microstructure, mechanical properties and corrosion resistance of dissimilar welds between Inconel 718 and 310S austenitic stainless steel. INT J PRES VES PIP., (2014) 116, 37-46.
6. Y. Behnamian, A. Mostafaei, A. Kohandehghan, B.S. Amirkhiz, J. Li, R. Zahiri, E. Aghaie, W. Zheng, D. Guzonas, M. Chmielus, W. Chen, J.L. Luo, Internal oxidation and crack susceptibility of alloy 310S stainless steel after long term exposure to supercritical water at 500℃. J. Supercrit. Fluids 120 (Part 1), (2017) 161-172.
7. W.S. Park, S.W. Yoo, M.H. Kim, J.M. Lee, Strain-rate effects on the mechanical behavior of the AISI 300 series of austenitic stainless steel under cryogenic environments, Mater. Des., 31 (2010) 3630–3640.
8. W.S. Lee, C.F. Lin, Comparative study of the impact response and microstructure of 304L stainless steel with and without prestrain, J. Mater. Eng. Perform., (2002) 33, 2801–2810.
9. Post-Solidification Phase Transformations, Welding Metallurgy Second edition, Sindo Kou, John Wiley & Sons, (2002) 216-241.
10. Metals handbook, 8 end, Vol. 8, 424;1973, Metals Park, OH, American Society for Metals.
11. J.C. Lippold, W.F. Savage, Solidification of austenitic stainless Steel Weldments: Part Ⅲ- The Effect of Solidification Behavior on Hot Cracking Susceptibility Welding research supplement, (1982) 388-396.
12. V. Shankar, T.P.S. Gill, S.L. Mannan, S. Sundaresan, Solidification cracking in austenitic stainless steel welds, WELDING J., (2003) 28, 359-382.
13. E. Folkhard, Welding metallurgy of stainless steels (New York: Springer Verlag) (1988).
14. J.W Pugh, J.D. Nisbet, A study of the iron-chromium-nickel ternary system, JOM, (1950) 188, 268-276.
15. T. Koseki, M.C. Flemings, Solidification of undercooled Fe–Cr–Ni alloys part II – microstructural evolution. Metall. Mater. Trans., (1996) 3226–3240.
16. V. Laitinen, Weldability of powder bed fusion fabricated stainless steel 316L sheets to cold rolled sheet metal, Thesis for: M. Sc., (2015).

17. J.A. Brooks, A.W. Thompson, Microstructural development and solidification cracking susceptibility of austenitic stainless steel welds, INT MATER REV, (1991) 36, 16-44.
18. P.K. Nanavati, B.J. Chauhan, S.N. Soman, Prediction of solidification mode in super austenitic stainless steel welds, IJAERD, (2018) 5, 201-209.
19. R. Saluja, K.M. Moeed, The emphasis of phase transformations and alloying constituents on hot cracking susceptibility of type 304L and 316L stainless steel welds, IJEST, (2012) 4, 2206-2216.
20. Y. Arata, F. Matsuda, S. Saruwatari, Varestraint test for solidification crack susceptibility in weld metals of austenitic stainless steels. Trans. Jpn., (1974) 3, 79–88.
21. Y. Arata, F. Matsuda, H. Nakagawa, S. Katayama, Solidification crack susceptibility in weld metals of fully austenitic stainless steels (Report 112), Transactions of JWRI, (1978) 7, 169-172.
22. Y. Arata, F. Matsuda, S. Katayama, Varestraint test for solidification crack susceptibility in weld metal of austenitic stainless steels, Transactions of JWRI, (1973) 3, 79-88.
23. Y. Arata, F. Matsuda, S. Katayama, Solidification crack susceptibility in weld metals of fully austenitic stainless steels (Report 112), Transactions of JWRI, (1977) 6, 105-116.
24. D. Wang, S. Sakoda, K. Kadoi, K. Shinozaki, M. Yamamoto, Investigation of evaluation method for hot cracking susceptibility of 310S stainless steel during laser welding using trans-varestrain test, Transaction of JWRI, (2015) 33, 39-43.
25. T. Ogawa, E. Tsunetomi, Hot cracking susceptibility of austenitic stainless steels, W J supplement, (1982) 82-93.
26. F. Matsda, H. Nakagawa, T.Uehara, S. Katayama, Y. Arata, A new explanation for role of delta-ferrite improving weld solidification crack susceptibility in austenitic stainless steel, Transaction of JWRI, (1979) 8, 105-112.
27. U. Feurer, Giessereiforschung, (1976) 28, 75–80.
28. Y.F. Guven, J.D. Hunt, Hot-tearing in Aluminium Copper Alloys, Cast Met., (1988) 2, 104–11.
29. J. Campbell: Castings, Butterworth-Heinemann, Oxford, United Kingdom, 2003.
30. S. Kou, A criterion for cracking during solidification, Acta Mater., (2015) 88, 366–74.
31. N. N. Prokhorov, Resistance to hot tearing of cast metals during solidification, Russ. Cast. Prod., (1962) 4, 172-175.
32. M. Rappaz, J.M. Drezet, M. Gremaud, A new hot-tearing criterion, Metal. Mater. Trans. A, (1999) 30, 449–55.
33. D.G. Eskin, Suyitno, L. Kangerman, Mechanical properties in the semi-solid state and hot tearing of aluminium alloys, PROF MATER SCI, (2004) 49, 629-711.
34. L. Aucott, D. Huang, H.B. Dong, S.W. Wen, J.A. Marsden, A. rack & A.C.F. Cocks, Initiation and growth kinetics of solidification cracking during welding of steel, SCI REP-UK, (2017).
35. L. Aucott, D. Huang, H.B. Dong, S.W. Wen, J.A. Marsden, A. rack & A.C.F. Cocks, A Three-Stage Mechanisitic Model for Solidification Cracking During Welding of Steel, METALL MATER TRANS A, (2018) 49, 1674-1682.

36. J.C Borland, R.N. Younger, Some aspects of cracking in welded Cr-Ni austenitic steels, Br. Weld J., (1960) 22-59.
37. W.S. Pellini, Strain theory of hot tearing. Foundry, (1952) 80, 124-34 and 196-99.
38. F. Matsuda, H. Nakagawa, T. Uehara, S. Katayama, Y. Arata, A new explanation for role of δ-ferrite improving weld solidification crack susceptibility in austenitic stainless steel. Trans. Jpn. Weld., (1979) 8, 105–112.
39. V. Kujanpaa, N. Suutala, T. Takalo, T. Moisio, Correlation between solidification cracking and microstructure in austenitic–ferritic stainless steel welds. Weld. Res., (1979) 9, 55–76.
40. F.C. Hull, Effects of alloying additions on hot cracking of austenitic stainless steels. Proc. ASTM, (1960) 60, 667–690.
41. Principles and Technology of the Fusion Welding of Metals, Vol.1, Mechanical Engineering Publishing Co., Peking, China, (1970).
42. F. Matsuda,S. Katayama, Y. Arata, Solidification crack susceptibility in weld metals of fully austenitic stainless steels – solidification crack susceptibility and amount of phosphide and sulphide in SUS 310 weld metal. Trans. Jpn. Weld., (1981) 10, 201–212.
43. J.A. Brooks, Effect of alloy modifications on HAZ cracking of A-286 stainless steel, Weld. J., (1974) 53, 517–523.
44. B. Dixon, Weld metal solidification cracking in austenitic stainless steels. Aust. Weld. J., (1988) 16, 2–10.
45. F. Matsuda, H. Nakagawa, S. Katayama, Y. Arata, Solidification crack susceptibility in weld metals of fully austenitic stainless steels (report VI) – effect of La or REM addition on solidification crack resistance. Trans. Jpn. Weld. Res., (1982) 11, 79–94.
46. W.S. Pellini, Strain theory of hot tearing, The foundry, (1952) 80, 125-133.
47. J.C. Boland, Generalized theory of super-solidus cracking in welds and castings, British Weld. Jour., (1960) 7, 508-512.
48. H. Fredriks, L. J. van der Toorn, Hot cracking in austenitic stainless steel weld deposits, British Weld. Jour., (1968) 178-182.
49. W. Dahl, C. Duren, H. Musch, Effect of various alloying elements on the hot cracking susceptibility of austnitic steel during welding, Stahl und Eisen, (1973) 93, 813-822.
50. S.M. Makin, C.B. Alock, D.M. Arell, P.C.L. Pfeil, Distribution of phosphorus and sulfur in fully austenitic stainless steel welds. British Weld. Jour., (1960) 595-599.
51. J.N. Cordea, P. A. Kammer, D. C. Martin, Causes of fissuring in nickel-base and stainless steel alloy weld metals, Welding J., (1960) 43, 481-491.
52. R. Scherer, G. Riedrich and H. Hougardy, 1941 (May 6) Welding rod. U.S. patent 2, 240, 672.
53. F.C. Hull, Effect of delta ferrite on the hot cracking of strainless steel, Welding J., (1967) 46, 399-409.
54. T.G. Cooch, J. Honeycombe, Microcracking in fully austenitic stainless steel weld deposits, Metal Construction and British Weld. Jour., (1970) 375-380.

55. T.G. Gooch, J. Honeycombe, Effect of manganese on cracking and corrosion behavior of fully austenitic stainless steel weld metals, Metal Construction and British Weld. Jour., (1972) 456-460.
56. N.N. Prokhorov, The problem of the strength of metals while solidifying during welding, Svar Proiz, (1956) 6, 5-11.
57. T. Senda, F. Matsuda, G. Takano, Studies on solidification crack susceptibility for weld metals with trans-varestraint test, J. Japan Weld Soc, (1973) 42, 48-56.
58. M. Shibahara et al., Effect of various factors on solidification crack under FCB welding, 溶接構造シンポジウム 2014.
59. R.A. Chihoski, The character of stress fields around a weld arc moving on an aluminium sheet, Weld J, (1972) 51, 9-18.
60. T. Zacharia, Dynamic stress in weld metal hot cracking, Weld J (1994) 73, 164-172.
61. Z. Feng, T. Zacharia, SA David, On the thermomechanical conditions for weld metal solidification cracking. In: Mathematical modelling of weld phenomena 3, (1997) Inst Materials, London, 199-222.
62. J.J. Dike, JA. Brooks, M. Li, Comparison of failure criteria in weld solidification cracking simulations. (1998) In: Mathematical modelling of weld phenomena 4. Inst Materials, London, 199-222.
63. J.H. Lee, S. Yamashita, T. Ogura, K. Saida, Suppression of solidification cracking via thermal strain control in multi-beam welding, MATER TODAY COMMUN, (2020) 24, 101094.
64. J.H. Lee, S. Yamashita, T. Ogura, K. Saida, Solidification cracking prevention by thermal strain control via water-cooled gas tungsten arc welding, MATER TODAY COMMUN, (2020) 24, 101109.
65. R. Batra, GA. Wilber, HF Breit, WJ Childs, Programmed in situ metling, freezing and tensile testing for laboratory study of high temperature properties of Ascast metals, Journal of Testing and Evaluation, (1975) 3, 68-74.
66. N.N. Prokhorov, The technological strength of metals while crystallizing during welding, Welding Production, (1962) 9, 1-8.
67. F. Matsuda, H. Nakagawa, S. Tomita, Quantitative evaluation of solidification brittleness of weld metal during solidification by in-situ observation and measurement (Rpt .3).Transactions JWRI, (1986) 15.
68. W.F. Savage, C.D. Lundin, Application of the varestraint technique to the study of weldability. Weld. J. (1965) 45, 497–503.
69. J.C. Lippold, W. Lin, Weldability of commercial Al-Cu-Li alloys. In: Proc. Of ICAA5, Aluminum Alloys - Their Physical and Mechanical Properties, eds.. Driver JH et al., Transtec Publications, (1996) 1685-1690.
70. T. Senda et al., Studies on solidification crack susceptibility for weld metals with trans-varestraint test (1), Japan Welding Society, (1972) 41, 113-127.

71. J. Andersson, J. Jacobsson, C. Lundin, A historical perspective on Varestraint testing and the importance of testing parameters. 4th International Hot Cracking Workshop, Berlin, Germany, (2014).
72. D. Wang, S. Sakoda, K. Kadoi, K. Shinozaki, M. Yamamoto, Investigation of evaluation method for hot cracking susceptibility of 310S stainless steel during laser welding using trans-varestraint test, Quaterly Journal of the JWS, (2015) 33, 39-43.
73. D. Wang, K. Kadoi, K. Shinozaki, M. Yamamoto, Evaluation of solidification cracking susceptibility for austenitic stainless steel during laser trans-varestraint test using two dimensional temperature measurement, ISIJ International, (2016) 56, 20220-2028.
74. K. Kadoi, A. Fujinaga, M. Yamamoto, K. Shinozaki, The effect of welding conditions on solidification cracking susceptibility of type 310S stainless steel during laser welding using an in-situ observation technique, Weld World, (2013) 57, 383-390.
75. P. Wen, K. Shinozaki, M. Yamamoto, Y. Senda, T. Tamura, N. Nemoto, In-situ observation of solidification cracking of laser dissimilar welded joints, Quaterly Journal of the JWS, (2009) 27, 134-138.
76. F. Matsuda, H. Nakagawa, S. Tomita, Investigation of weld solidification cracking by MISO technique (Report 1), Quaterly Journal of the JWS, (1988) 6-3, 394-400.
77. K. Shinozaki , X. Lou , H. Ariyoshi, H. Kuroki , M. Shirai, Quarterly Journal of the Japan Welding Society, (1999) Vol. 17 No.2, p. 279.
78. F. Matsuda, H. Nakagawa, K. Nakata, H. Kohmoto, Y. Honda, Quantitative evaluation of solidification brittleness of weld metal during solidification by means of in-situ observation measurement (Report I), Transaction of JWRI, (1983) 12, 65-72.
79. F. Matsuda, H. Nakagawa, K. Nakata, H. Kohmoto, Y. Honda, Quantitative evaluation of solidification brittleness of weld metal during solidification by means of in-situ observation measurement (Report Ⅱ), Transaction of JWRI, (1983) 12, 73-80.
80. T. Senda, F. Matsuda, G. Takano, K. Watanabe, T. Kobayashi, T. Matsuzaka, Fundamental investigation on solidification crack susceptibility for weld metals with transvarestraint test, Trans. JWS, (1971) 2, 1-22.
81. Y. Arata, F. Matsuda, K. Nakata, I. Sasaki, Solidification crack susceptibility of aluminum alloy weld metal (report I). Trans. JWRI (1976) 5, 53–67.
82. Y. Arata, E. Matsuda, S. Katayama, Solidification crack susceptibility in weld metals of fully austenitic stainless steels (Report II) -- Effect of ferrite, P, S, C, Si, and Mn on ductility properties of solidification brittleness. Transactions of JWRl, (1977) 6, 105-117.
83. V. M. Radhakrishnan, Hot cracking in austenitic stainless steel weld metals, Sci. Technol. Weld. Join., (2000) 5, 40–44.
84. T. J. Lienert, J. C. Lippold: Improved weldability diagram for pulsed laser welded austenitic stainless steels, Sci. Technol. Weld. Join., (2003) 8, 1–9.
85. C. D. Lundin, C.-P. D. Chou, C. J. Sullivan: Hot cracking resistance of austenitic stainless steel weld metals, Weld. J., (1980) 59, 226–232.
86. J. A. Brooks, F. J. Lambert Jr., The effect of phosphorus, sulfur and ferrite content on weld cracking of type 309 stainless steel, Weld. J., (1978) 57, 139–143.

87. F. Matsuda, H. Nakagawa, S. Katayama, Y. Arata, Weld metal cracking and improvement of 25%Cr–20%Ni (AISI 310S) fully austenitic stainless steel, Trans. JWS, (1982) 13, 115– 132.
88. V. P. Kujanpaa, S. A. David, C. L. White, Formation of hot cracks in austenitic stainless steel welds-solidification cracking, Weld. J., (1986) 65, 203–212.
89. V. P. Kujanpaa, Effect of steel type and impurities in solidification cracking of austenitic stainless steel welds, Met. Construct., (1985) 17 40–46.
90. T. G. Gooch, J. Honeycombe, Welding variables and microfissuring in austenitic stainless steel weld metal, Weld. J., (1980) 59, 233–241.
91. G. Rabensteiner, J. Tosch, H. Schabereiter, Hot cracking problems in different fully austenitic weld metals, Weld. J., (1983) 62, 21–27.
92. K. Nishimoto, H. Mori, Hot cracking susceptibility in laser weld metal of high nitrogen stainless steels. Sci Technol Adv Mater., (2004) 5, 231–240.
93. SAAA. Mousavi, A. Gharedaghi, M. Mastoori, Metallurgical investigations of laser welding of AISI 304 stainless steel, Mater Sci Forum., (2008) 580, 41–44.
94. JC. Lippold, Solidification behavior and cracking susceptibility of pulsed-laser welds in austenitic stainless steels, Weld J., (1994) 73, 129–139.
95. K. Shinozaki, P. Wen, M. Yamamoto, K. Kadoi, Y. Kohno, T. Komori: Effect of grain size on solidification cracking susceptibility of type 347 stainless steel during laser welding, Trans JWRI., (2010) 39, 136 –138.
96. S. Katayama, Improvement in solidification cracking of fully austenitic stainless steels SUS310S [doctoral thesis]. Osaka University (in Japanese); (1981).
97. L. Li, RW Jr. Messler, The effect of phosphorus and sulfur on susceptibility to weld hot cracking in austenitic stainless steels, Weld J., (1999) 78, 387–396.
98. L. Kosec, S. Savli, S. Kozuh, T.H. Grguric, A. Nagode, G. Kosec, G. Drazic, M. Gojic, Transformation of austenite during isothermal annealing at 600-900 ℃ for heat-resistant stainless steel, J ALLOY COMPD, (2013) 562, 59-64.
99. J.H. Moon, M.G. Yoon, T.K. Ha, Microstructure and high temperature deformation behavior of cast 310S alloy, WASET, (2014) 8, 533-536.
100. ArcelorMittal, SIRIUS 310S: A 25% Cr-0.6% Si heat resistant stainless steel; https://industeel.arcelormittal.com/wp-content/uploads/2016/01/DS-INOX-SIRIUS310Sv2.pdf
101. Acerinox 310s stainless steel; https://www.acerinox.com/opencms901/export/sites/acerinox/.content/galerias/galeria-descargas/galeria-documentos-producto/ACX350-low.pdf
102. Atals steels stainless steel grade datasheets; http://www.atlassteels.com.au/site/pages/stainless-steel-datasheets.php
103. Austenitic stainless steel - Kloeckner Metals UK; https://www.kloecknermetalsuk.com/wp-content/uploads/2015/12/Austnitic-Stainless-Steel-310_310s.pdf

104. E.J. Chun, H. Baba, K. Nishimoto, K. Saida, Evaluation of solidification cracking susceptibility in austenitic stainless steel welds using laser beam welding transverse-varestraint test, in: Cracking Phenomena in Welds IV, Thomas Boellinghaus, John C. Lippold and Carl E. Cross, Switzerland Springer (2016) 161–203.
105. S. Fukumoto, W. Kruz, The δ to γ transition in Fe−Cr−Ni alloys during laser treatment, ISIJ International., (1997) 37, 677−684.
106. J. Lipton, W. Kurz, R. Trivedi, Rapid dendrite growth in undercooled alloys, ACTA METALL MATER., (1987) 35, 957−964.
107. T. Osuki, H. Hirata, K. Ogawa, Numerical analysis of solidification process of austenitic stainless steel weld metal with dependence of welding velocity−Study of solidification structure on austenitic stainless steel weld metal, Q J Jpn Weld Soc., (2007) 25, 140−148.
108. H. Mori, K. Nishimoto, Theoretical analysis on hot cracking behavior in laser surface melted region of austenitic stainless steel. Proceedings of the Finnishi−German−Japanese Joint International Seminar on Mechanical and Metallurgical Approaches to New Joining Process, (2004) 221−231.
109. W.J. Boettinger, D. Shechtman, R.J. Schaefer, F.S. Biancaniello, The effect of rapid solidification velocity on the microstructure of Ag-Cu alloys, Metallurgical transactions A, (1984) 15, 55-66.
110. MJ Aziz, Model for solute redistribution on during rapid solidification, J APPLY PHYS., (1982) 53, 1158-1168.
111. K. Saida, Y. Nishijima, H Ogiwara, K. Nishimoto, Prediction of solidification cracking in laser welds of type 310 stainless steel, Q J Jpn Weld Soc, (2013) 31, 157-166.
112. M.H. Burden, J.D. Hunt, Cellular and dendritic growth-Ⅱ. J. Appl., (1974) 22, 109-116.
113. M. Morishita, H. Ishida, M. Yoshida, Modeling of microsegregation and precipitation of iron metallic compounds in Al–Fe–Si ternary alloy. JJILM., (2010) 60, 157−163.
114. V. Plochikhine, H.W. Zoch, V.A. Karhin, M. Makhutin, H.J. Pesch, Numerical optimization of the temperature field for the prevention of solidification cracking during laser beam welding using the multi-beam technique. Proceedings of international conference on materials week., (2002) 1-7.
115. G. Gobel, B. Brenner, Avoiding hot cracking by induction based change of thermal strains during laser welding. Laser Materials Processing Conference., (2006) 34-43.
116. E.J. Chun, H. Baba, K. Nishimoto, K. Saida, Development of Laser Beam Welding Transverse-Varestraint Test for Assessment of Solidification Cracking Susceptibility in Laser Welds. Met. Mater. Int., (2015) 3, 543-553.
117. K. Saida, Y. Okabe1, K. Hata1, K. Nishimoto, K. Kiuchi, J. Nakayama, Hot cracking behavior and susceptibility of extra high purity type 310 stainless steels. SCI TECHNOL WELD JOI. (2019) 15, 87-96.
118. H. Kihara, F. Matsuda, Varestraint test for Hot Crack Susceptibility of HY-type High Strength Steels. JWRI., (1973) 2, 83-95.

119. Y. Chen, F. Lu, K. Zhang, S.R.E. Hosseini, K. Feng, Z. Li, Dendrite microstructure and hot cracking of laser additive manufacture Inconel 718 under improved base cooling, J ALLOY COMPD, (2016) 670, 312-321.
120. M. Sistaninia, S. Terzi, A.B. Phillion, J.M. Drezet, M. Rappaz, ACTA METALL MATER, (2013) 61, 3831.
121. M. Sistaninia, A.B. Phillion, J.M. Drezet, M. Rappaz, ACTA METALL MATER, (2012) 60, 6793.
122. C.M. Gourlay, A.K. Dahle, T. Nagira, N.Nakatsuka, K. Nogita, K. Uesugi, H. Yasuda: Granular deformation mechanism in semisolid alloys, ACTA METALL MATER, (2011) 59, 4933.
123. A.R. Safari, M.R. Forouzan, M. Shamanian, Hot cracking in stainless steel 310s, numerical study and experimental verification, Comput. Mater. Sci, (2012) 63, 182-190.
124. S. Okano, K. Matsushita, M. Mochizuki, M. Toyoda, A discussion of the relationship between heat input parameter and angular distortion by considering moving heat source effect, Weld. Int., (2014) 28, 683-692.
125. X. Wang, H.P. Wang, F. Lu, B.E. Carlson, Y. Wu, Analysis of solidification susceptibility in side-by-side dual-beam laser welding of aluminum alloys, Int. J. Adv. Manuf. Technol., (2014) 73, 73–85.
126. V. Ploshikin, A. Prihodovsky, A. llin, C. Heimerdiger, F. Palm, Computer Aided Development of the Crack-free Laser Welding Process, Key Eng. Mater., (2007) 353-358, 1184-1194.

## Published or Accepted Papers in Regards to This Thesis

1. Jae-Hyeong Lee, Yu Itasaka, Shotaro Yamshita, Tomo Ogura and Kazuyoshi Saida, Prediction of solidification cracking during arc welding of 310S stainless steel in U-type hot cracking test, Quarterly Journal of the Japan Welding Society, 38 (2020) 68-75. (Chapter3)
2. Jae-Hyeong Lee, Shotaro Yamshita, Tomo Ogura and Kazuyoshi Saida, Suppression of solidification cracking via thermal strain control in multi-beam welding, Materials Today Communications, 24 (2020) 101094. (Chapter 7)
3. Jae-Hyeong Lee, Shotaro Yamshita, Tomo Ogura and Kazuyoshi Saida, Solidification cracking prevention by thermal strain control via water-cooled gas tungsten arc welding, Materials Today Communications, 23 (2020) 101109. (Chapter 5)
4. Jae-Hyeong Lee, Shotaro Yamshita, Tomo Ogura and Kazuyoshi Saida, Effect of welding condition on solidification cracking behavior in austenitic stainless steel, Science and Technology of Welding Joining, https://doi.org/10.1080/13621718.2020.1837490. (Chapter 6)

# Presentations

1. Jae-Hyeong Lee, Yu Itasaka, Shotaro Yamshita, Tomo Ogura and Kazuyoshi Saida, Prediction of solidification cracking by controlling thermal strain using in-situ post heating, Japan Welding Society, Spring, 2019, Tokyo, Japan.
2. Jae-Hyeong Lee, Shotaro Yamshita, Tomo Ogura and Kazuyoshi Saida, Welding process optimization for solidification cracking prevention by using solidification cracking prediction model, Japan Welding Society, 2019, Osaka, Japan.
3. Jae-Hyeong Lee, Shotaro Yamshita, Tomo Ogura and Kazuyoshi Saida, Effect of solid-liquid coexistence region on solidification cracking occurrence by U-type hot cracking test, Japan Welding Society, Autumn, 2019, Osaka, Japan.
4. Jae-Hyeong Lee, Shotaro Yamshita, Tomo Ogura and Kazuyoshi Saida, Application of cooling process for preventing solidification cracking by thermal strain control, Japan Welding Society, Spring, 2020, Osaka, Japan.